UNIVERSITY OF CALIFORNIA, SAN DIEGO

Calcium imaging and the neurovascular unit: Challenging the role of astrocytes as mediators of neurovascular coupling

A dissertation submitted in partial satisfaction of the requirements for the degree Doctor of Philosophy

in

Neurosciences

by

Krystal Wen-Tung Nizar

Committee in charge:

Professor Gabriel A. Silva, Chair
Professor Anna Devor, Co-Chair
Professor Richard Buxton
Professor Eliezer Masliah
Professor Nicholas Spitzer

2010

The Dissertation of Krystal Wen-Tung Nizar is approved, and it is acceptable in quality and form for publication on microfilm and electronically:

_____

_____

_____

_____
Co-Chair

_____
Chair

University of California, San Diego

2010

TABLE OF CONTENTS

LIST OF ABBREVIATIONS

2-DG	2-deoxyglucose
20-HETE	20-hydroxyeicosatetraenoic acid
ACh	acetylcholine
ACSF	artificial cerebrospinal fluid
AD	Alzheimer's disease
ATP	adenosine triphosphate
BBB	blood-brain barrier
BOLD	blood oxygenation level dependent
CBF	cerebral blood flow
$CMRO_2$	cerebral metabolic rate of oxygen
CO_2	carbon dioxide
DMSO	dimethyl sulfoxide
EETs	epoxyeicosatrienoic acids
FCIP	fluorescent calcium indicator protein
FITC	fluorescein dextran
fMRI	functional magnetic resonance imaging
GABA	gamma-aminobutyric acid
$GABA_AR$	type-A GABA receptor
mGluR	metabotropic glutamate receptor
MCT	monocarboxylate transporter
NADH	ß-nicotinamide adenine dinucleotide
NMDAR	N-methyl-D-aspartic acid receptor
NO	nitric oxide
NOS	nitric oxide synthase
NVU	neurovascular unit
OGB	Oregon Green BAPTA-488/ AM
ROI	region of interest
SI	primary somatosensory cortex
SOM	somatostatin
SR101	sulforhodamine 101
TPLSM	2-photon laser scanning microscopy

LIST OF FIGURES

ACKNOWLEDGEMENTS

I would like to thank Professor Anna Devor and Professor Gabriel Silva for their support as the chairs of my committee. Thank you for giving me the opportunity to work in your laboratories. Without your guidance and undying fortitude along the way, none of this would have been possible.

I would also like to acknowledge the wonderful help and technical expertise of Ms. Qun Cheng, whose surgical technique and skill helped to make all of our *in vivo* work possible.

Thanks also to Marius Buibas, Chris MacDonald, Tyler Steed, Payam Saisan, and Vishnu Sridhar for bearing witness to my love/hate relationship with Matlab, and being willing to lend a capable hand when hate >= love.

Chapter 4 is a reprint of the material as it appears in Mapping the Spatiotemporal Dynamics of Calcium Signaling in Cellular Neural Networks Using Optical Flow, Buibas, Marius; Yu, Diana; Nizar, Krystal; Silva, Gabriel, Annals of Biomedical Engineering, 2010.

VITA

2004 Bachelor of Arts, Neurosciences, University of Chicago
Bachelor of Arts, Psychology, University of Chicago
Summa Cum Laude

2010 Doctor of Philosophy, University of California, San Diego

2004-2012 Medical Scientist Training Program (M.D./Ph.D.)
University of California, San Diego

RESEARCH EXPERIENCE

Graduate Student Research, Sept. 2006 - present
University of California, San Diego, Neurosciences

Anna Devor: In vivo imaging of neuroglial calcium and microvascular dynamics
Gabriel A. Silva: In vitro calcium imaging of spontaneously forming neuroglial networks and retinal explants

Graduate Independent Study, Jul. 2004 - Sept. 2004
University of California, San Diego, Neurosciences

Anirvan Ghosh: Activity dependence of dendritic branching complexity in GFP-transfected cultured rat hippocampal neurons
Binhai Zheng: Spinal cord injury model induced expression of Semaphorins and Netrins in reactive gliosis
Yimin Zou: Wnt signaling in anterior-posterior axon guidance and growth cone dynamics

Neurobiology Honors Research, Jan. 2002 - June 2004
University of Chicago, Dept. of Neurobiology & Pharmacology

Dorothy Hanck: Developmental CNS expression, physiology, and pharmacology of voltage-gated T-type calcium channels

Undergraduate Research Assistant, Sept. 2000 - Dec. 2001
University of Chicago, Dept. of Psychology

John T. Cacioppo: Influence of facial feedback on racial bias as measured by performance on the implicit association task

PUBLICATIONS

Peer-reviewed publications:

Nizar K, Tian P, Reznichenko L, Cheng Q, Sridhar V, Steed T, Saisan P, Sakadžić S, Boas DA, Masliah E, Dale AM, Silva GA & Devor A. (2010) Neuronal but not astrocytic calcium increase correlates with the laminar profile of microvascular dilation in response to sensory stimulation. (in preparation)

Sakadžić S, Nizar K, Cheng Q, Boas DA, Kasischke KA & Devor A. (2010) In vivo functional NADH imaging with single-cell resolution confirms neural activity triggers neuronal followed by astrocytic oxidative metabolism. (in preparation)

Reznichenko L, Nizar K, Cheng Q, Devor A & Masliah E. (2010) In vivo study of abnormal neuronal Ca2+ activity in a-synuclein transgenic mice model of Parkinson's disease using 2-photon microscopy. (in preparation)

Buibas M, Yu D, Nizar K & Silva GA. (2010) Mapping the spatiotemporal dynamics of calcium signaling in cellular neural networks using optical flow. Ann Biomed Eng. Mar19.

Ito TA, Chiao KW, Devine PG, Lorig TS & Cacioppo JT. (2006) The influence of facial feedback on race bias. Psych Science. 17(3):256-61.

Abstracts and Conference Proceedings:

Nizar K, Reznichenko L, Cheng Q, Sakadzic S, Boas DA, Masliah E, Dale AM, Silva GA, Devor A. Delayed and infrequent astrocytic calcium response does not support the hypothesis of calcium-dependent astrocytic regulation of blood flow. 2010 Society for Neuroscience Annual Meeting.

Nizar K, Tian P, Reznichenko L, Cheng Q, Sakadzic S, Boas DA, Masliah E, Dale AM, Silva GA, Devor A. Delayed and infrequent astrocytic calcium response does not support the hypothesis of calcium-dependent astrocytic triggering of blood flow. 2010 Gordon Research Conference: Brain Energy Metabolism & Blood Flow. 2010 Outstanding Poster Award

Devor A, Sakadzic S, Pokrovsky A, Nizar K, Yucel MA, Teng IC, Kasischke KA, Boas DA. In vivo functional NADH imaging with single-cell resolution. 2009 Society for Neuroscience Annual Meeting.

MacDonald CL, Chiao KW, Creveling D, Abarbanel HD, Silva GA. Nonlinear estimation of spike rates from neuronal intracellular calcium signals. 2008 Society for Neuroscience Annual Meeting.

Chiao KW, Silva GA. Geometric and physiological properties of functional connectivity patterns arising in spontaneously forming neuron networks. 2007 Biomedical Engineering Society Annual Meeting.

Chiao KW, Silva GA. The role of glial network calcium dynamics in neurological disorders. 2007 Society for Neuroscience Annual Meeting.

ABSTRACT OF THE DISSERTATION

Calcium imaging and the neurovascular unit: Challenging the role of astrocytes as mediators of neurovascular coupling

by

Krystal Wen-Tung Nizar

Doctor of Philosophy in Neurosciences

University of California, San Diego, 2010

Professor Gabriel A. Silva, Chair
Professor Anna Devor, Co-Chair

Historically, experimental methods to investigate astrocyte function in the intact brain have been limited by the fact that glia are electrically silent. This has led to a heavy reliance on calcium imaging techniques in the study of astrocyte function. In the past decade, the widespread use of this technique, particularly *in vivo*, has pushed the boundaries of what can be accomplished with fluorescent imaging. This series of studies is dedicated to taking that boundary a step further, utilizing the technology currently available to ask fundamental questions regarding the neurovascular unit (NVU), and concluding with some perspectives on the advances still needed to fully elucidate the functional role of astrocytes within the NVU. This

dissertation is focused on astrocytic function in relation to the vascular compartment, astrocytic function in relation to the neuronal compartment, and finally, astrocytic function in relation to each other (Fig. A.1). In considering the vascular aspect of the NVU, we compare the *in vivo* temporal characteristics of the cerebral blood vessel dilation and the astrocytic calcium response to increased neuronal activity. We provide evidence of a significant temporal mismatch that challenges the popular idea of a calcium-dependent astrocytic role in triggering neurovascular coupling. In considering the metabolic aspect of the NVU, we report here the first application of 2-photon laser scanning microscopy (TPLSM) to functional imaging of intrinsically fluorescent ß-nicotinamide adenine dinucleotide (NADH) as a means to visualize single cell metabolism *in vivo*. We demonstrate, through this new imaging modality, that astrocytes respond readily and rapidly to evoked neuronal activity. We suggest that, contrary to what is indicated by their calcium activity, astrocytes are actually very sensitive to neuronal activity, and do respond on a relevant time scale, but do not necessarily act as mediators in translating neuronal activity to the vasculature. Given their prominent yet mysterious place within the NVU, there is a great need to identify suitable methodologies to describe the large repertoire of astrocytic calcium dynamics, ranging from subcellular compartments to network-level waves. Toward this end, we report on the application of optical flow image analysis to calcium signaling dynamics in spontaneously forming networks of astrocytes and neurons. By using information gained from a reduced preparation in conjunction with the whole animal approach, we hope to contribute to the set of tools that will be necessary to accurately assess the role(s) of astrocytes within the NVU.

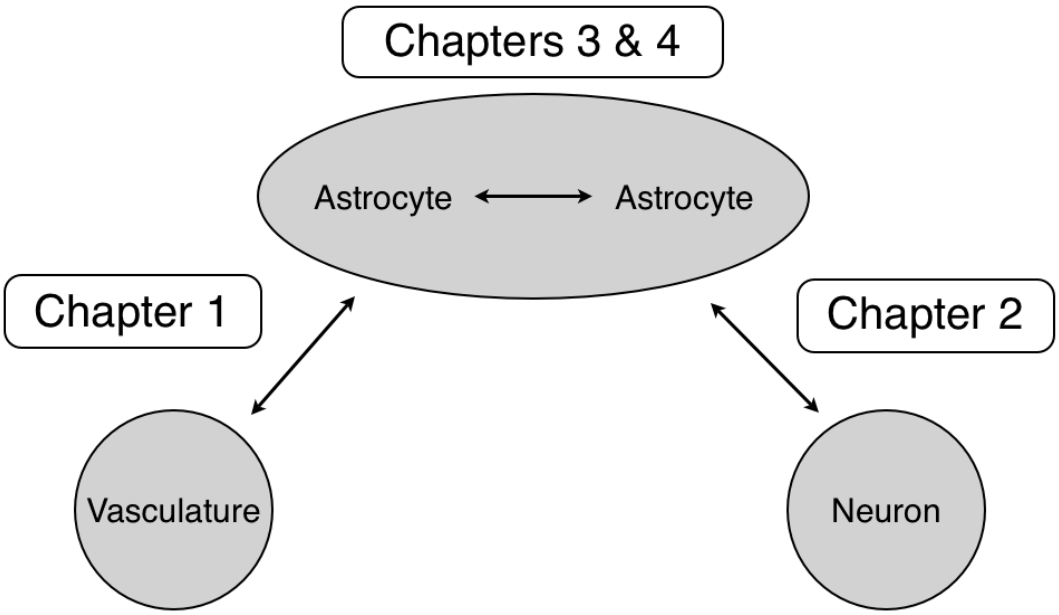

Figure A.1 Components of the neurovascular unit (NVU) and chapter layout.

INTRODUCTION

High levels of activity of neurons in a specific brain region lead to an increase in blood flow to that area in a temporally and spatially coordinated manner (Roy, 1890). The term “neurovascular coupling” refers to this linking of local neuronal activity to blood flow and the delivery of glucose and oxygen for energy metabolism. Despite the implication of a number of vasoactive molecules and specific cell-types through *in vitro* experiments, the exact mechanism of transformation of stimulus-induced activation of neuronal circuits to hemodynamic changes remains unclear, primed for direct interrogation via *in vivo* imaging. To probe this question of neurovascular coupling on a microscopic scale, we turn to the *in vivo* mouse model of somatic stimulation and TPLSM imaging of populations of cells, both neuronal and astrocytic, adjacent to components of the microvasculature. Using this preparation, we evaluate the validity of two of the leading hypotheses regarding the mechanism of neurovascular coupling: (1) calcium-dependent release of vasoactive gliotransmitters, referred to as the “astrocytic” hypothesis, and (2) the generation of vasoactive metabolites, referred to as the “metabolic” hypothesis.

The astrocytic hypothesis of neurovascular coupling

Recently, it has been proposed that vascular dilation in response to an increase in neuronal activity is mediated by calcium-dependent release of vasoactive gliotransmitters (Iadecola and Nedergaard, 2007). In Chapter 1, we investigate the temporal relationship between astrocytic increase in intracellular calcium and cerebrovascular dilation. Through simultaneous observation, we uncover an unreliable and significantly delayed astrocyte calcium response to stimulus-evoked neuronal activity. These characteristics of response argue against the “astrocytic”

hypothesis, and indicate that it is unlikely that astrocytes play a significant role in generation of the dilatory response to brief stimulation in healthy subjects. Thus, astrocytes may be of limited relevance, ultimately, to the interpretation of fMRI signals generated using event-related stimulus paradigms. Given that they do not reliably elevate calcium, we asked then, is there another, more reliable, component to the astrocytic response to elevated neuronal activity?

The metabolic hypothesis of neurovascular coupling

According to the "metabolic" hypothesis of neurovascular coupling, the state of neuroglial energy consumption directly determines the regional blood flow through the production of vasoactive metabolites (Magistretti, 2006). This hypothesis has been directly challenged by the observed dissociation between increased blood oxygenation/flow and 2-deoxyglucose (2-DG) uptake. Vasoconstriction, rather than vasodilation, can be observed in the presence of increased 2-DG uptake and increased neuronal spiking in ipsilateral SI (Devor, 2008), indicating that increased energy (glucose) consumption by neurons is not sufficient to produce neurovascular coupling. In a related fashion, it has been theorized that cerebral blood flow (CBF) could be coupled directly to energy consumption and oxygen metabolism through an erythrocyte based mechanism where deoxygenated hemoglobin triggers the release of vasoactive metabolites. The prevention of hemoglobin deoxygenation via hyperbaric hyper-oxygenation has demonstrated that it is not necessary for neurovascular coupling (Lindauer, 2010). Together, these studies indicate that neither neuronal energy consumption, nor the shortage of energy substrates, is responsible for the tight coupling between neuronal activity and CBF changes. However, metabolic signaling between neurons and the vasculature could still be

mediated through astrocytes, as astrocytes have yet to be examined *in vivo* in terms of their energy consumption on a single-cell level. In Chapter 2, NADH fluorescence imaging is used as a means to monitor single-cell metabolism *in vivo*. We utilize this technology to assess another potential dimension of astrocytic responsiveness to changes in the NVU. The time-course of fall in NADH fluorescence suggests that, in terms of oxidative metabolism, astrocytes respond readily and rapidly to evoked neuronal activity and have the potential to act as mediators in translating the energy demand of neuronal activity to the vasculature.

Astrocytic networks respond to both acute and chronic injury

In the literature regarding astrocyte-to-astrocyte signaling, there exists a significant discrepancy between *in vitro* and *in vivo* results. Intercellular calcium waves have long been observed in the contexts of cultured astrocytes and brain slices. These waves can be elicited by a wide variety of stimuli, including mechanical perturbation and purinergic receptor agonists. However, until last year, the *in vivo* existence of intercellular calcium waves was doubted. Even now, spontaneous intercellular calcium waves have only been observed in the specialized cases of cerebellar Bergmann glia, Muller cells of the retina, and within the plaque expressing Alzheimer's disease (AD)-model mouse cortex. The third chapter of this thesis seeks to answer the question of why this discrepancy exists. It is a well known fact that astrocytes are organized into networks anatomically, but it remains unclear how these networks actually operate, functionally. One approach is to assess the particular environmental cues and conditions necessary to activate the astrocyte's long-range signaling machinery. A complete understanding of the highly variable calcium dynamics of astrocytes will require detailed examination of the

calcium “wave.” We question whether this type of calcium activity in cortical astrocytes is a strictly AD-related pathological phenomenon, varying tunable parameters of the experimental preparation in order to gauge their effects on emerging calcium dynamics. None of our manipulations change the sporadic, unpredictable nature of astrocyte calcium activity, but phenomenological instances of spontaneously correlated, oscillatory behavior do emerge, indicating the existence of network-level astrocyte activity in the acutely injured mouse cortex, and not exclusively in the context of chronic pathology like AD.

Finally, we take up the issue of identifying signal processing methods useful to the detection and description of highly variable, spontaneous astrocyte calcium signals. This is important and necessary given the findings described in Chapter 3 indicating that spontaneous calcium activity could potentially serve as a biomarker of acute stress or chronic disease. Optical flow, by measuring the direction, speed, and ultimately path that a signal might take, can supplement information obtained through methods that analyze the dynamics of individual cell bodies. Optical flow vectors can, additionally, show the direction that a signal travels along a cell projection, which can complement correlation studies by identifying the directionality of signaling between cells. Optical flow is a well established method of image analysis -- we show how it can be used with calcium signaling data, and discuss what kinds of novel information it can provide the investigator.

Chapter I : Delayed and infrequent calcium response does not support the hypothesis of calcium-dependent astrocytic triggering of vasodilation

ABSTRACT

Understanding the mechanisms that control cerebral blood flow is crucial for the development of new strategies for treatment of cerebrovasular disease and for better interpretation of noninvasive neuroimaging data. Recently, it has been proposed that vascular dilation in response to an increase in neuronal activity is mediated by calcium-dependent release of vasoactive gliotransmitters. However, it remains unclear whether the onset of astrocytic calcium response precedes the onset of vasodilation, as would be expected if the former triggers the latter. To investigate the temporal relationship between astrocytic increase in intracellular calcium and microvascular dilation, we used TPLSM to simultaneously image neuroglial calcium activity and diameter changes in nearby arterioles and capillaries. Our results indicate that, despite the robust dilation response, astrocytic calcium increase was observed only infrequently and was considerably delayed relative to the onset of the arteriolar/capillary dilation. Within the measured depth range, down to 500 μm from the pial surface, astrocytes in the immediate vicinity of dilating arterioles did not exhibit a more reliable calcium response than those around surfacing venules. The slow onset and infrequent occurrence of the astrocytic calcium response challenge the hypothesis of an astrocytic role in triggering the vascular dilation of neurovascular coupling.

INTRODUCTION

A basic, cellular, mechanistic level understanding of the physiological regulation of blood flow should start with understanding the bidirectional interactions of each of the components of the neurovascular unit (NVU). A mechanistic understanding of CBF regulation is necessary to fully capitalize on the potential of fMRI as a diagnostic tool, with its potentially useful application to patient populations with diseases where blood flow has been compromised, such as AD, Parkinson's disease, stroke, and cerebrovascular dementia.

Astrocyte ability to sense and modulate their environment is a topic of great interest given their unique positioning in the cellular architecture. Astrocyte processes are in close contact with both neuronal synapses (Ventura et al., 1999) and cerebral arterioles (Paspalas et al., 1998). Each individual astrocyte extends at least one process with endfeet surrounding a blood vessel (Simard et al., 2003). In contrast, processes from neurons rarely come in direct contact with intraparenchymal blood vessels. In addition, astrocytes have many fine processes that extend beyond the large processes that typically stain for intermediate filaments. Its fine processes have minimal spatial overlap with the processes of other astrocytes, and results in individual astrocytic domains (Bushong, 2002), positioning them well to shape the spatial distribution of the vascular responses evoked by neural activity. These anatomical relationships have led to the hypothesis that astrocytes play a pivotal role in the dynamic regulation of the cerebral circulation. According to this hypothesis, vascular dilation in response to an increase in neuronal activity is mediated by the calcium-dependent release of vasoactive gliotransmitters (Zonta, 2003; Iadecola, 2007).

A quantitative understanding of how neuronal activity may drive changes in blood flow and energy metabolism is key to the proper interpretation of functional neuroimaging studies in humans. Functional magnetic resonance imaging (fMRI), based on the blood oxygenation level dependent (BOLD) response, has become a widely used tool for exploring brain function. Despite its widespread use, fMRI has had remarkably limited impact on clinical practice. This is because the signal is straightforward and robust to localize, but, given its physiological complexity, difficult to interpret in terms of the magnitude, and even polarity, of change in neuronal activity that it represents.

The BOLD magnetic resonance signal reflects the loss of oxygen from hemoglobin, which causes its iron to become paramagnetic, allowing it to influence the magnetic field experienced by protons in surrounding water molecules. The BOLD effect results from the fact that cerebral blood flow (CBF) increases much more than the cerebral metabolic rate of oxygen ($CMRO_2$) consumption (oxidative metabolism) in response to increased neural activity. This relative hyperemic response results in a net decrease of deoxygenated hemoglobin. Thus, functional hyperemia can also be detected as a localized increase in blood oxygenation. This increase is what is detected in BOLD imaging studies. The magnitude of this increase depends on the relative changes in CBF and $CMRO_2$, and cannot serve, itself, as a direct reflection of the magnitude of change in neuronal activity. Better understanding of the relationships between neuronal, CBF (vascular), and $CMRO_2$ (metabolic) responses is needed to interpret fMRI signal in a more quantitative and physiologically meaningful manner.

Experiments in brain slice have shown that blood vessels can both dilate and constrict in response to elevated astrocytic intracellular calcium concentration (Metea and Newman, 2006; Mulligan and MacVicar, 2004; Filosa et al. 2004; Gordon et al. 2008). Changes in astrocytic calcium are known to mediate the synthesis and/or release of vasoactive agents, with vasodilatory (e.g., epoxyeicosatrienoic acids (EETs), and prostaglandins) or vasoconstricting (e.g., 20-hydroxyeicosatetraenoic acid (20-HETE)) effects, which are involved in the control of the brain microcirculation. Importantly, both dilators and constrictors are synthesized in a calcium-dependent manner from common precursors (reviewed in (Straub, 2007)). In addition, some of the variability (dilation or constriction) in vascular response observed in slice experiments could also be explained by the baseline state of smooth muscle cells in the absence of normal blood pressure and flow (Blanco, 2008).

In the majority of *in vivo* studies of physiological sensory stimulation, induced astrocytic calcium transients have been shown to be significantly delayed with respect to the onset of stimulation, neuronal response, and the known dynamics of vascular responses (Wang, 2006; Gobel, 2007). In fact, a recent study in ferret visual cortex, where both calcium and hemodynamic responses were measured, reported an increase in blood volume preceding an increase in astrocytic calcium by several seconds (Schummers, 2008) (see also (Koehler, 2009) for further discussion on the discrepancy of astrocytic and blood flow response time scales). Thus, we hypothesize that astrocytic calcium response to physiological stimulation will exhibit a significantly delayed time course relative to the neuronal and vascular components of the NVU response.

Although astrocytes express receptors for numerous neurotransmitters and neuropeptides, most studies have focused on glutamate. Specifically, it has been shown that glutamate activates metabotropic receptors (mGluR) that cause calcium influx from intracellular stores (Porter, 1996; Zonta, 2003). Experiments in brain slices have shown that astrocytes respond to neuronal activity by elevation in intracellular calcium concentration (Zonta, 2003; Simard, 2003; Gordon, 2008). Astrocytes are well-positioned to sense glutamatergic synaptic activity over a large spatial domain via activation of mGluRs and subsequent calcium signaling, and via energy-dependent glutamate transport. In addition, activation of astrocytic GABA receptors has also been shown to produce calcium transients (Nilsson 1993). Other receptors, including acetylcholine (ACh), noradrenaline (NA), vasopressin (VIP), somatostatin (SOM), and more, are less understood, although most of them are also metabotropic and their activation is expected to elevate astrocytic calcium concentration. The elevation of intracellular calcium can, in turn, trigger the synthesis and release of vasoactive gliotransmitters (Zonta, 2003; Mulligan, 2004).

Given previous studies which measured both cerebrovascular dilation and astrocyte calcium dynamics, we suspect that there exists a temporal mismatch between these two events, such that astrocytic calcium transients do not precede (and therefore, cannot trigger) vascular dilation in response to neuronal activity. In order to fully characterize the calcium responsiveness of astrocytes to neuronal activity in these experiments, temporal profile, depth relationship, vessel relationship, and potential subcellular compartmentalization will be assessed.

MATERIALS AND METHODS

Animal preparation

Sprague-Dawley rats (n = 6; females; 120-200g) and ICR mice (n = 12; 20-45 g) were used. All experimental procedures were approved by the University of California at San Diego Institutional Animal Care and Use Committee. In rats, glycopyrrolate (0.4 mg/kg, SC) was administered 15 minutes prior to the initiation of anesthesia. Rats and mice were anesthetized with 1.5% (v/v) isoflurane in oxygen and placed on a heating blanket to maintain body temperature at 37ºC. All incisions were infiltrated with 2% lidocaine. Tracheotomy was performed and a cannula was inserted in the femoral artery. Following tracheotomy, animals were ventilated with ~1.0% isoflurane in a mixture of air and oxygen. Ventilation parameters were consistently adjusted to maintain PaCO2 between 35 and 45 mmHg, PaO2 between 140 and 180 mmHg, and pH between 7.35 and 7.45. An area of skull overlying S1 was removed, and the dura matter was dissected to expose the underlying cortical tissue. To avoid herniation of the exposed brain caused by excessive intracranial pressure, cerebro-spinal fluid (CSF) was drained from the fourth cerebral ventricle in the following way: dorsal neck muscles over the cerebellum and the first two cervical vertebrae were pulled apart to expose the dura matter at the junction between the cerebellum and the spinal cord. The dura was punctured using a #11 scalpel blade to release CSF. A metal frame and a glass coverslip lid to the craniotomy were glued with dental acrylic to the exposed skull. The space between the exposed brain surface and the coverslip was filled with 1.5% (wt/vol) agarose (Sigma) in artificial cerbrospinal fluid (ACSF: 142mM NaCl, 5mM KCl, 10mM glucose, 10mM HEPES, Na Salt, 3.1mM $CaCl_2.6H_2O$, 1.3mM $MgCl_2.6H_2O/MgSO_4.7H_2O$).

Following surgery, isoflurane was discontinued, and anesthesia was maintained with 40 mg/kg intravenous bolus of α-chloralose followed by continuous intravenous infusion at 40 $mg*kg^{-1}*h^{-1}$. Heart rate, blood pressure, expired CO2, SpO2, and body temperature were continuously monitored. Blood pressure was monitored invasively through the femoral arterial line and maintained below 120 mmHg. Heart rate was maintained below 800 beats per minute (bpm) for mice and 400 bpm for rats. Following the first successful imaging experiment, and given stable readings of physiological parameters and stable anesthesia conditions, animals were paralyzed with a 0.4 mg/kg bolus of pancuronium followed by continuous intravenous infusion at 0.4 mg/kg/h.

In separate experiments, anesthesia was maintained throughout both surgery and imaging with boluses of either 50 mg/kg urethane or a mixture of 100 mg/kg ketamine + 15 mg/kg xylazine, re-injected every 45-60 minutes.

Surface potential recordings

Recordings were made using a silver ball electrode positioned in direct contact with the cortical surface. Ball electrode recordings were made from 4-6 locations within a ~ 2 x 2 mm exposure. The signals were amplified and filtered between 0.1 Hz and 10 kHz.

Cell labeling

Suforhodamine 101 (SR101) is a water-soluble red fluorescent dye that readily and specifically stains astrocytes in the neocortex of rats and mice. Brief topical application of SR101 to the exposed surface of the intact neocortex results in bright staining of the astrocyte network (Nimmerjahn et al. 2004). Injection bulk loading of neurons and astrocytes with a Ca2+ indicator, and rapid, non-invasive labeling with SR101 allow for the discrimination of calcium transients in neurons from astrocytes.

The membrane-permeable acetoxymethyl(AM)-ester form of fluorescent indicators of intracellular calcium can be loaded into neuronal and glial cell populations in the neocortex *in vivo*. It is nonspecifically taken up and trapped inside cells once the ester groups have been cleaved by endogenous esterases. Oregon-Green-BAPTA-488/AM (OGB) labels both neuronal and glial networks and permits counterstaining with red fluorescent SR101.

The calcium indicator OGB (50 µg in 40 µL artificial cerebro-spinal fluid (ACSF) plus 4 µL of 20% pluronic acid in DMSO) was microinjected at the center of the neuronal response as determined by surface potential mapping performed immediately before the injection. SR101 was dissolved in ACSF, yielding a final concentration of ~10 µM and applied topically to the exposed cortex for 3-5 minutes, after which unbound dye was washed away with repeated applications of ACSF.

Intravascular labeling

Visualization of the vasculature was achieved by injection of green fluorescent dye (~300 µL (rats) or 50 µL (mice) of 5% (wt/vol) solution of 2MDa fluorescein-conjugated dextran (FD-2000S; Sigma) in physiological saline) into the blood stream through the femoral artery catheter. High-molecular-weight carrier molecules (2 MDa dextran) were used to minimize the excretion of the dye. The labeling stains only the blood plasma, allowing the flowing red blood cells (RBCs) to appear as dark shadows against a bright background. This allows for the quantification of various parameters of microcirculation, including the topological organization of local blood flow and the density, flux, and speed of the RBCs.

Additionally, in separate experiments, the following two quantum dots were intravenously injected:

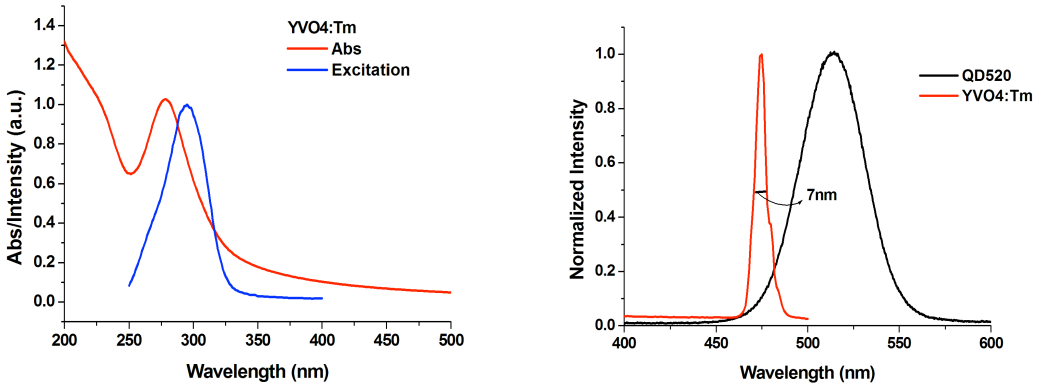

Figure 1.1 Absorption and emission spectra of Yttrium Vanadate Colloid. Thulium Doped Yttrium Vanadate Colloid 1µM solution (blue fluorescent quantum dots, Sun Innovations - Phosphor Dots - http://www.nanomaterialstore.com/nano-phosphor.php)

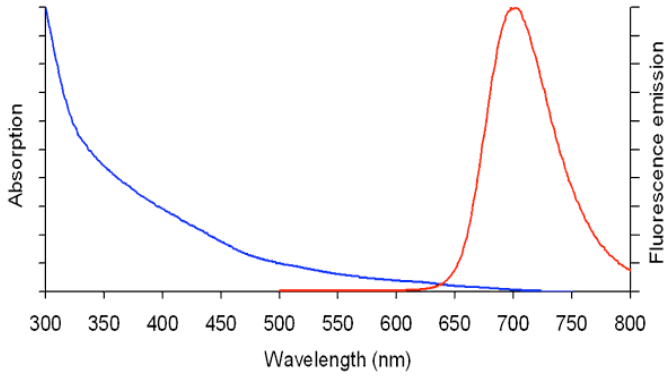

Figure 1.2 Absorption and emission spectra of Qdot 705 streptavidin conjugate in pH 7.2 buffer. Qtracker® 705 non-targeted quantum dots 2 µM solution (deep red dddfluorescent quantum dots, Invitrogen).

These dots were designed for small animal in vivo imaging, and especially for studying vascular structure after microinjection. These nanocrystals exhibit extremely intense fluorescence, red-shifted emission for increased tissue penetration, and a

PEG surface coating specially developed to minimize nonspecific interactions and reduce any immune response by the tissue.

Labeling of the vasculature with quantum dots was attempted on four separate occasions at the following volumes: 40µL Qtracker (2µM solution) in 100µL saline, followed by another 40µL of Qtracker. 100µL Qtracker in 100µL ACSF. 100µL Yttrium Vanadate Colloid (1µM solution) in 100µL saline. 100µL Yttrium Vanadate Colloid in 100µL ACSF. In all cases only extremely faint fluorescent signal was observed intravascularly and with poor contrast at multiple laser excitation wavelengths ranging from 780-820 nm.

Two-photon microscopy

Imaging was done within a 1-mm radius from the center of neuronal response as determined prior to the imaging session by surface potential recordings. Images were obtained using a 4-channel Ultima 2-photon microscopy system from Prairie Technologies (Middleton, WI). A 4x air objective (XLFluor 4x/340; numerical aperture (NA)=0.28; Olympus, Tokyo, Japan) was used to image the surface vasculature across the entire cranial window to aid in navigating around the cortical vasculature. 20x (XLUMPlanFI 20x; NA=0.95, Olympus) and 40x (Plan-Apochromat 40x; NA=0.8, Zeiss, Oberkochen, Germany) water-immersion objectives were used for high-resolution functional imaging. The laser (Ultra II, Coherent, Santa Clara, CA) was tuned to 800 nm. Four-channel detection of emission wavelength was achieved by using a 565 nm dichroic mirror (Chroma, Bellows Falls, VT) and four external photomultiplier tubes (Fig. 1.3). Images were acquired in a frame mode with a frame rate of ~10 Hz.

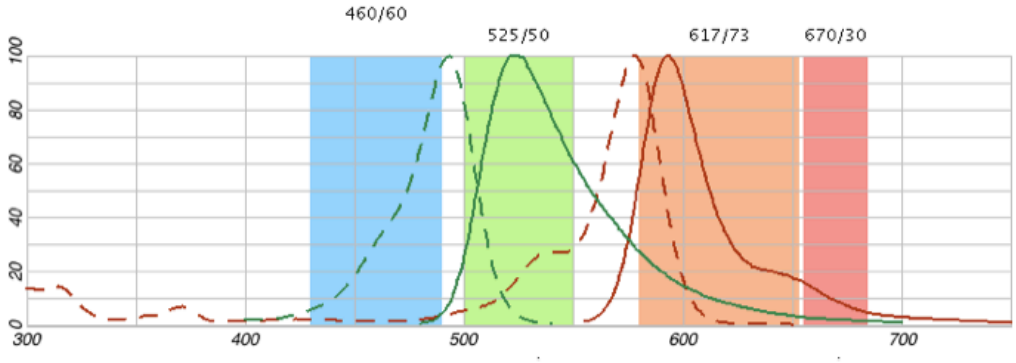

Figure 1.3 Fluorescence excitation and emission spectra of OGB and SR101 plotted along with the filter wavelength settings for each of four PMTs. Invitrogen - Molecular Probes - Fluorescence Spectra Viewer (http://probes.invitrogen.com/servlets/spectraviewer)

Stimulation

The stimulation in the majority of experiments lasted 2 seconds and consisted of a train of 6 electrical pulses (3 Hz, 300 μs, ~1mA) with interstimulus interval (ISI) of 25 s delivered to a forepaw through a pair of thin needles implanted under the skin. In separate subsets of experiments, the same forepaw stimulation laster 4 seconds, consisted of a train of 12 electrical pulses (3Hz, 30 μs, ~1mA) with ISI of 30 s, and stimulation lasted 5 s, consisted of a train of 15 electrical pulses (3 Hz, 300 μs, ~1mA) with ISI of 60 s delivered to the whisker pad through a pair of thin wires implanted under the skin. The intensity of the stimulus was adjusted to provide stimulation just below the movement threshold.

Stimulation was presented using a separate PC that also acquired TTL timing signals for data acquisition (“trigger out” TTLs for each frame) using a National Instruments IO DAQ interface controlled by in-house software in Matlab. The TTL

data were used to determine the timing of each frame relative to the stimulus onset during data analysis performed in Matlab.

Calcium data analysis

Bolus loading of calcium indicator results in unspecific staining of cells within a volume with a diameter of several hundred micrometers (Stosiek, 2003), necessitating the use of SR101 to discriminate neuronal and glial subpopulations. A critical issue in our data analysis was to correctly distinguish the fluorescence signals intrinsic to astrocytes from the "bleed through" of other neuropil signals. Because astrocytes are spongiform in nature there is a lack of defined border to the volume of space occupied by each astrocyte, and the "surrounding" neuropil can actually be thought of as being made up of the close apposition of astrocytic fine processes with neuronal processes.

Based on the morphological understanding of astrocytes gained from electron microscopy studies (Bushong, 2002), we model the astrocyte region of interest (ROI) as a two-dimensional plane of pixels whose fluorescence intensities can be attributed either to the astrocyte or to neuropil. There is a central density of pixels attributable to the astrocyte, corresponding to the astrocyte cell body, and more pixels attributable to neuropil as one moves toward the edge of the astrocytic ROI. This assumption is supported by the fact that stripping pixels from the edges of the ROI results in less and less contamination of the astrocytic signal with neuropil fluorescence. Furthermore, when astrocytes are well in focus at the plane of the 2-photon laser scan, there is virtually no cross-contamination of the astrocytic fluorescence signal with neuropil signal. In contrast, when the astrocyte is poorly in focus (lying primarily outside of the plane of laser scanning) there is a great deal of neuropil contribution. In addition, when astrocytes are topically loaded with Fluo-4,

the selective labeling of astrocytes and non-labeling of neurons always yields an uncontaminated astrocytic calcium fluorescence time course. Given these observations, we implemented a regression method for filtering out those pixels within the ROI with fluorescence signal matching the time course of fluorescence present in the neuropil as it responds to stimulus, averaging only those pixels that were attributable to the astrocyte itself.

RESULTS

I-1 The timing of microvascular dilation in response to sensory stimulation depends on the cortical depth.

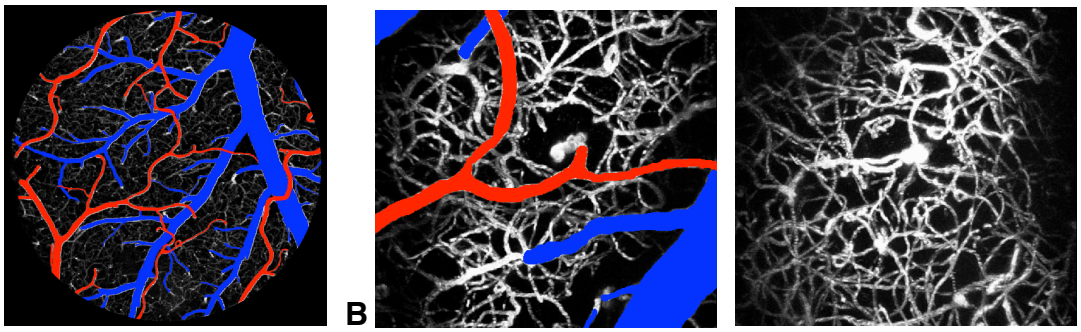

Figure 1.4 Example of cortical vasculature imaged with IV injection of a fluorescent contrast agent. (A) Maximum intensity projection (MIP) of a low magnification image stack showing the surface vasculature. (B) Two consecutive in depth high resolution MIPs of 0-300 µm and 300-525 µm of the region of interest (ROI).

We generated a body of TPLSM measurements of vascular diameters along the branching arteriolar trees all the way into capillary beds at different cortical depths. The depth limit of scanning was 550um, which corresponds to layer III in rat, but layer IV in mouse. These data strongly suggest that the first dilation occurs deeper than our penetration limit, probably in layer IV.

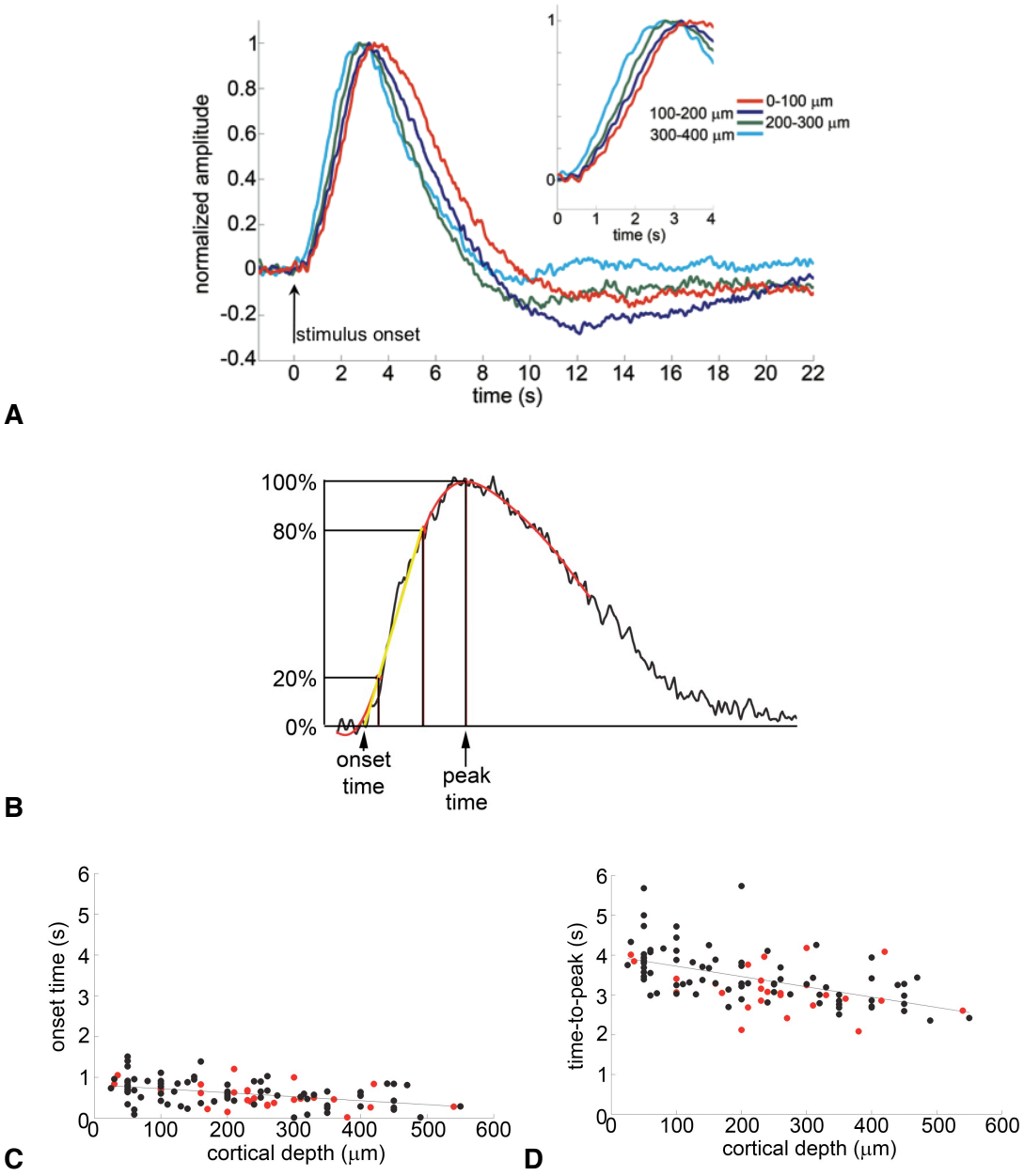

Figure 1.5 The onset and time-to-peak of arteriolar/capillary dilation decreases with increasing cortical depth. (A) Super-imposed time courses of diameter change across the categories of depth. (B) An example illustrating estimation of onset and time-to-peak. (C) Onset time as a function of the cortical depth. (D) Time-to-peak as a function of the cortical depth. Red dots indicate measurements from vessels with baseline diameter < 10μm.

I-2 The majority of astrocytes do not exhibit an increase in intracellular calcium in response to a brief sensory stimulation known to cause vasodilation.

Overall, only 9% of cells were “responsive” to the brief (2 s) forepaw stimulation which was presented. A “responsive” astrocyte was defined as one exhibiting an increase in ΔF/F within a 25 s window following stimulus presentation for at least one out of 10 trials. We further divided the analysis of responsiveness into subgroups of astrocytes which were “on” or “near” arterioles and venules as opposed to astrocytes associated with capillaries in the tissue. “On” refers to those astrocytes whose bodies wrap around the outer wall of the vessel it is associated with. “Near” was defined as the cell body being located < 50μm from the nearest vessel. Note, responding astrocytes were observed also around venules despite the fact that venous diameters cannot be actively controlled.

Overall, the slow kinetics of the calcium transient observed whenever a response was present is in agreement with previous studies (Gobel, 2007; Schummers, 2008; Wang, 2009). Where these findings differ from previous studies (Wang, 2006) is in the statistical quantification of how often responses were observed. No comparable statistics were provided for the previously observed “robust” astrocytic calcium responses to physiological stimulation.

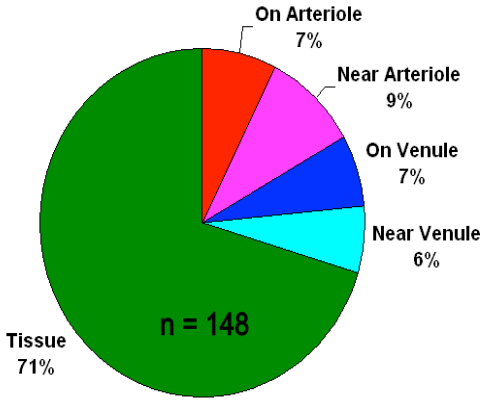

Layer I (< 100 µm)

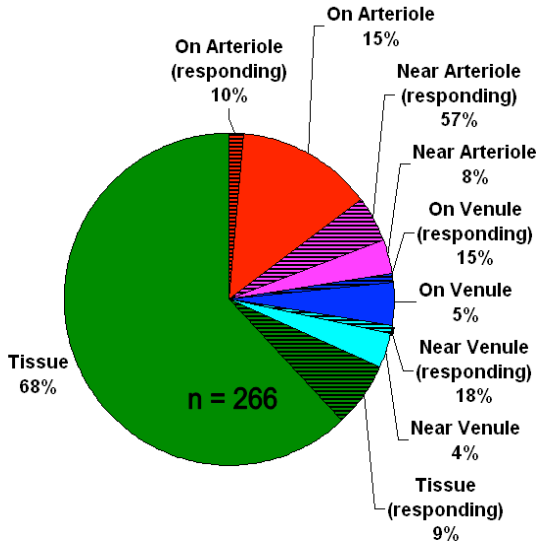

Layer II (100 - 225 µm)

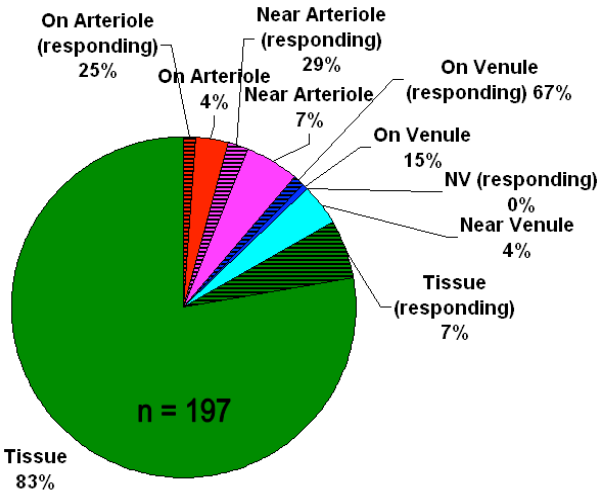

Layer III (225 - 410 µm)

Figure 1.6 Astrocytic increase in intracellular calcium ("astrocytic calcium response") following sensory stimulation is a rare event in SI. There were no responding cells in layer I (<100 μm depth).

On average, the responding astrocytes in layer II (100-225 μm depth) exhibited calcium transients to 1.8 out of 10 trials. The responding astrocytes in layer III (225-410 μm depth) exhibited calcium transients in response to 1.5 out of 10 trials.

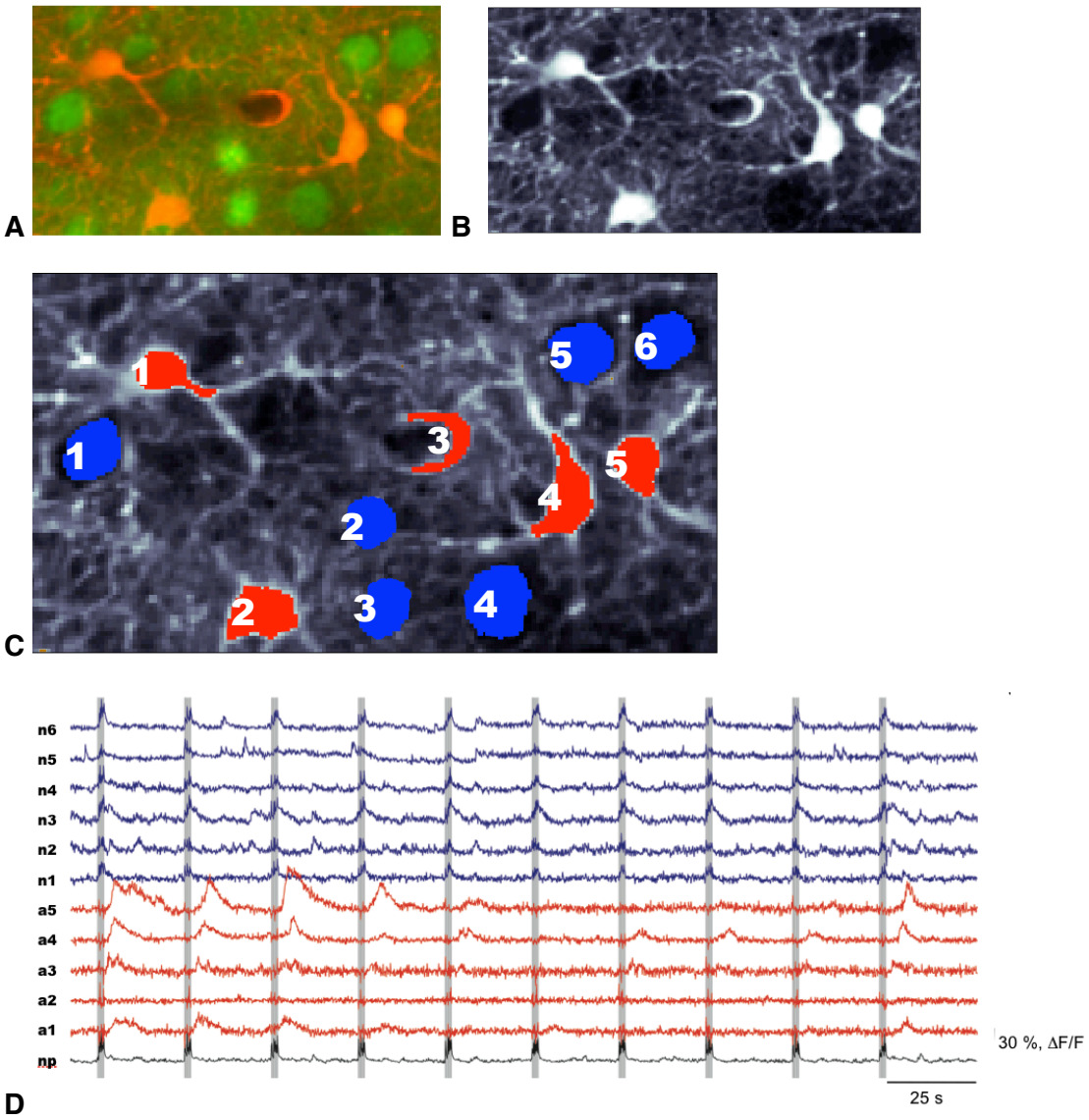

Figure 1.7 The best example of astrocytic calcium response. (A) Composite two-photon image of OGB and SR101 fluorescence at baseline. (B) SR101 image used to define astrocytic ROIs. (C) Astrocytic and neuronal ROIs. (D) Calcium signal time-courses extracted from the ROIs in C, expressed in % change relative to the pre-stimulus baseline. Gray bars indicate the stimulus duration (2 sec).

I-3 Simultaneous measurements demonstrate vasodilation in the absence of measurable astrocytic calcium response.

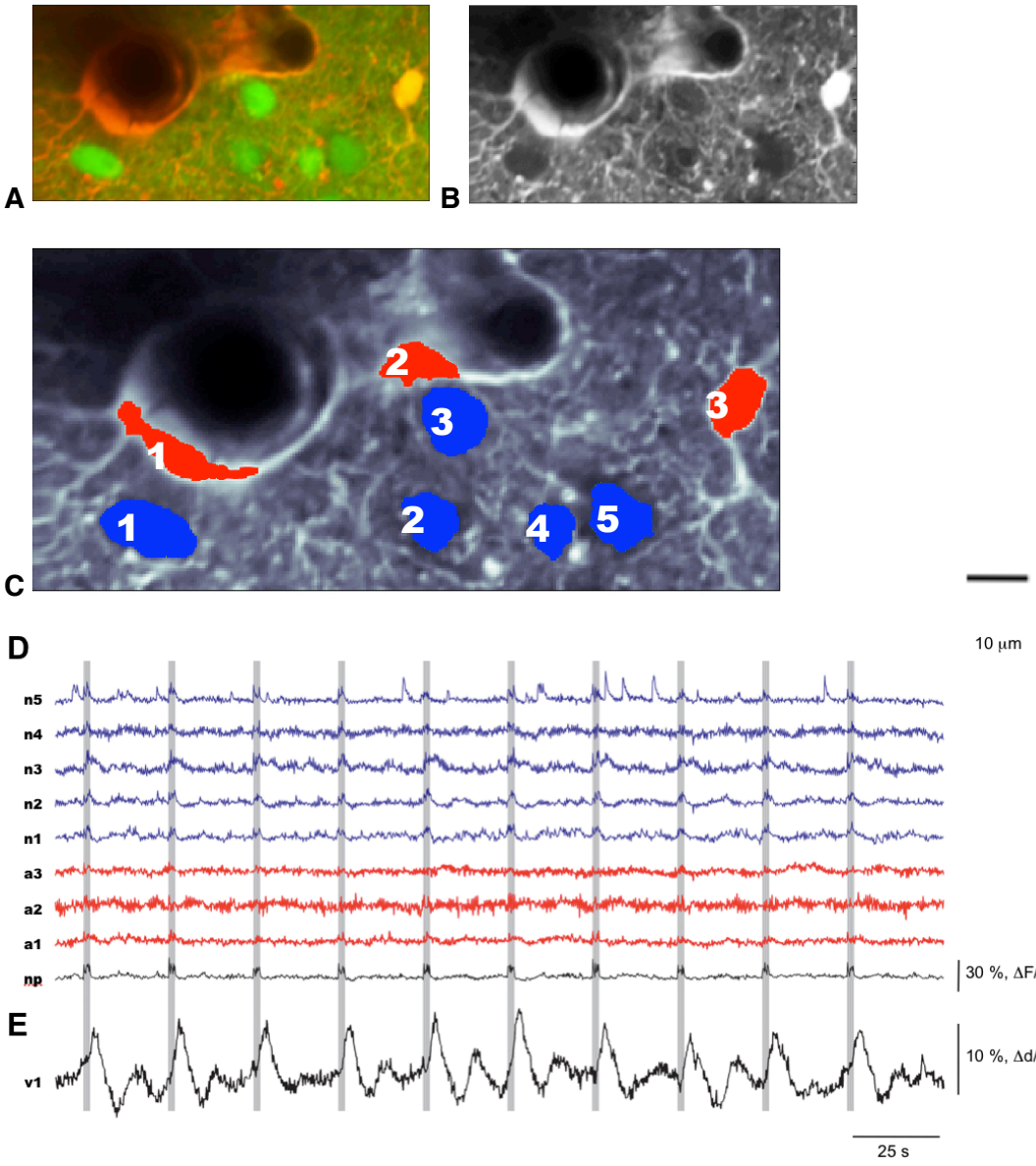

Figure 1.8 Simultaneous measurements of vascular diameters and calcium imaging. (A) Composite two-photon image of OGB1 and SR101 fluorescence at baseline. (B) SR101 image used to define astrocytic ROIs. (C) Astrocytic and neuronal ROIs. (D) Calcium signal time-courses extracted from the ROIs in C, expressed in % change relative to the pre-stimulus baseline. (E) Dilation time-course extracted from vessel (V1), expressed in % change relative to the pre-stimulus baseline.

Figure 1.9 (facing page) Same field of view as (Figure 1.8) except with a 4 second stimulus duration. (A) Composite two-photon image of OGB1 and SR101 fluorescence at baseline. (B) SR101 image used to define astrocytic ROIs. (C) Calcium signal time-courses extracted from the ROIs in 1.8 C, expressed in % change relative to the pre-stimulus baseline. (D) Calcium signal time-courses calculated using the AstroTracker, expressed in % change relative to the pre-stimulus baseline. This signal processing step eliminates the post-stimulus hemodynamic artifact of a dip in fluorescence due to light absorption by hemoglobin in overlying vessels.

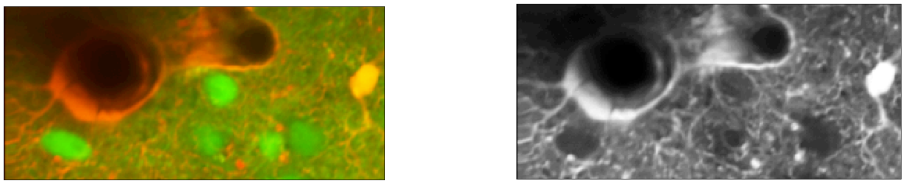

A B

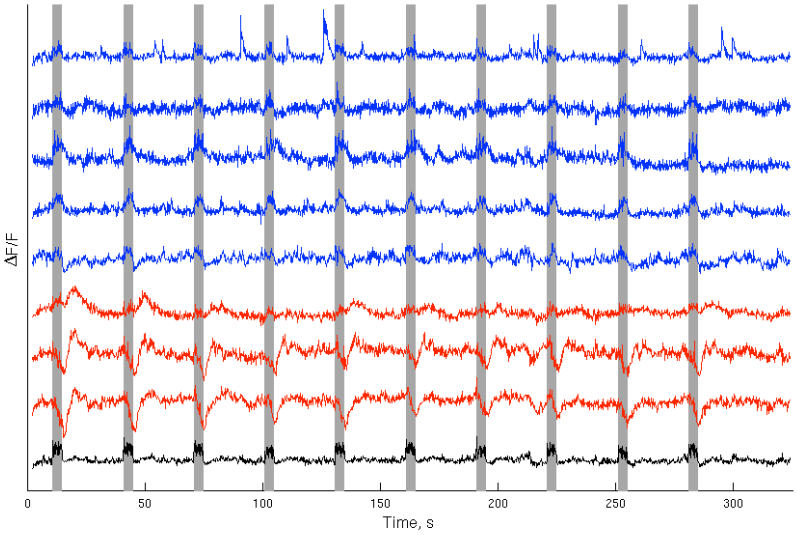
ΔF/F
0
50
100
150
200
250
300
Time, s

C

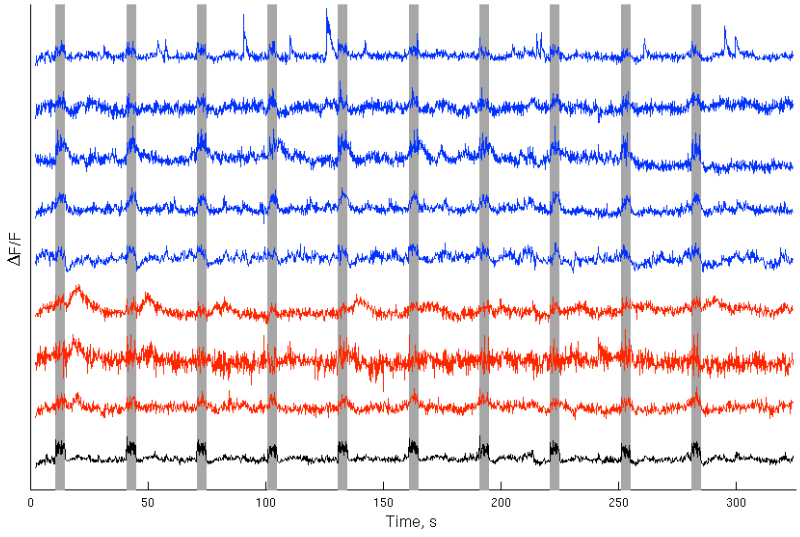
ΔF/F
0
50
100
150
200
250
300
Time, s

D

I-4 Explanation of the AstroTracker

This protocol was applied to all calcium imaging data prior to further group-based analysis. The user inputs the number of astrocytes in the field of view, a stack of images taken using the calcium channel filter (green), and a stack of images taken using the SR101 channel filter (red). The program thresholds the SR101 channel images such that only pixels that are 3 standard deviations above the average pixel intensity are looked at. It then smooths these pixels to form large regions to count as individual astrocytes (see Fig. 1.10 A). The number of regions must match the inputed number of astrocytes. The thresholded SR101 image then undergoes a distance transform (see Fig. 1.10 B) and a watershed transform (ROI erosion and dilation, respectively) to separate regions even if they are touching each other. Next, each separate region is labeled (Fig. 1.10 C) and the program extracts an average intensity value from all pixels belonging to each region (Fig. 1.10 D). This calculation and establishment of a new ROI occurs for each individual frame (Fig. 1.10 E shows an example frame) of the “movie” such that the ROI is capable of “tracking” the astrocyte of interest as it moves with vasodilation.

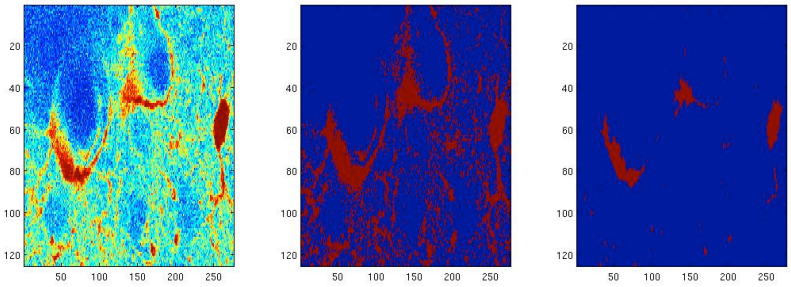

A

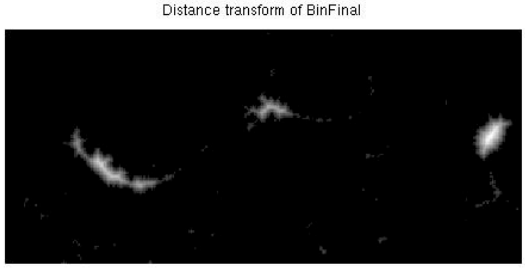

B

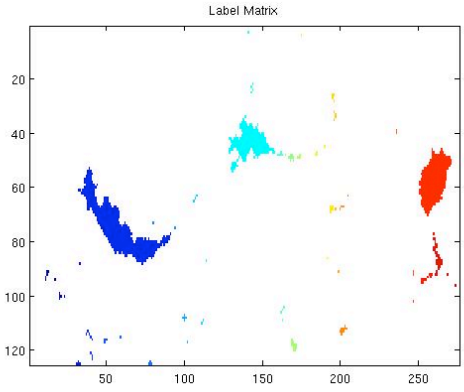

C

Figure 1.10 Explanation of the AstroTracker. (A) Thresholded and smoothed SR101 image. (B) Distance transform (ROI erosion) of the identified astrocyte ROIs. (C) Labeled ROIs colored according to each individual astrocyte. (D) Average intensity values extracted from pixels belonging to each ROI. (E) Example frame of “movie” showing the identified ROIs outlined and overlaid on the SR101 image (left) and the calcium image (right).

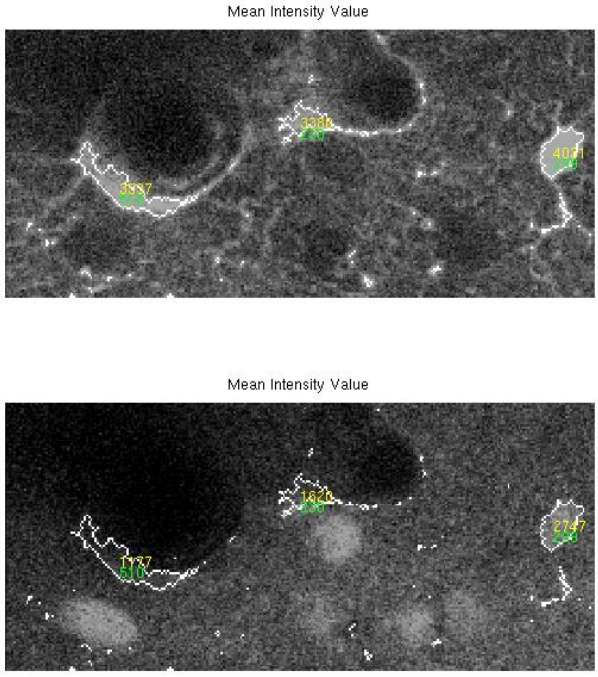

D

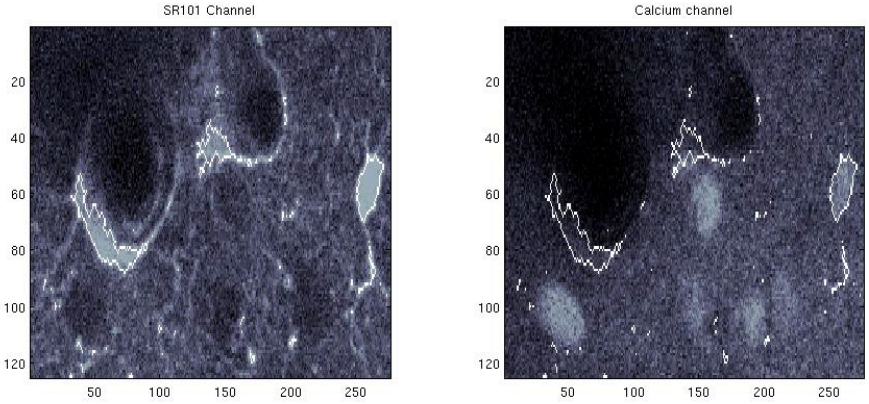

E

Figure 1.10 (continued)

I-5 When observed, astrocytic response is too slow to account for the onset of vasodilation.

Dilation is observed without astrocytic calcium response and has faster kinetics. Delay from stimulus to dilation = 400-500 ms. Delay to calcium transient ~ 2.5 s.

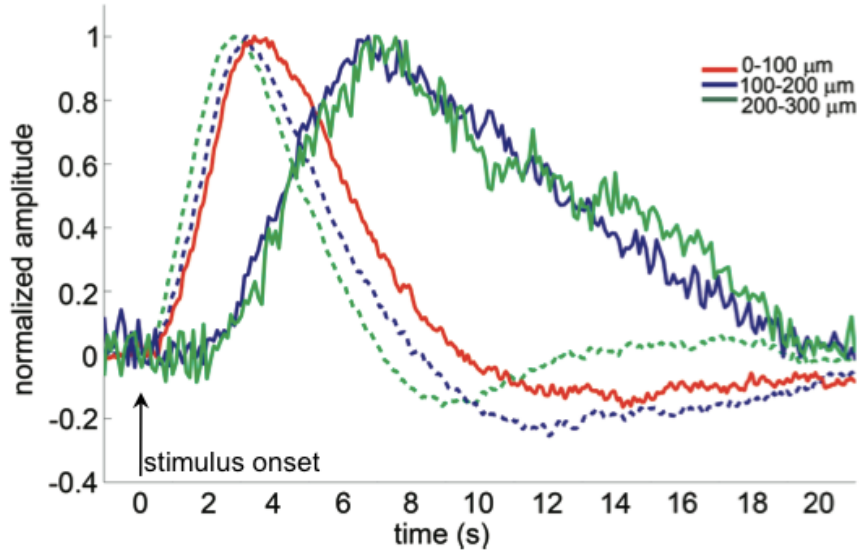

A

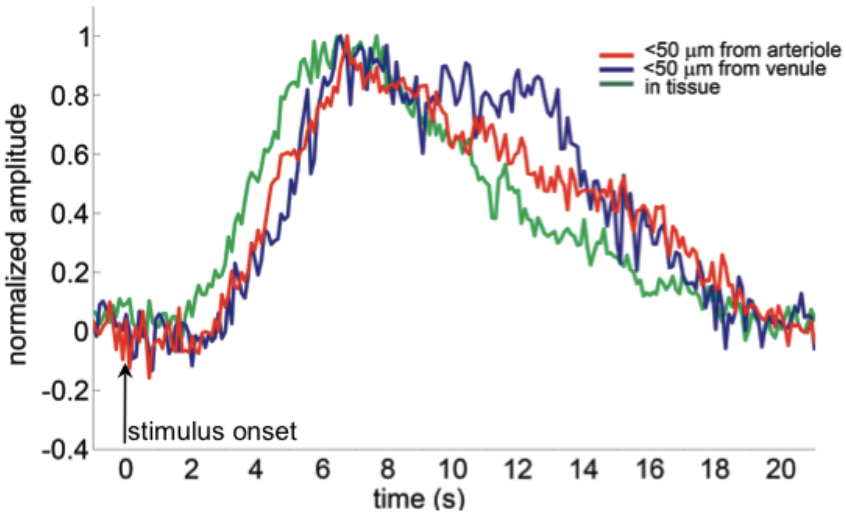

B

Figure 1.11 Comparison of the onset and time-to-peak of vasodilation and astrocytic calcium response. (A-B) All measured astrocytic calcium responses grouped by the cortical depth and their vessel relationship. Vasodilation time-courses from the corresponding depths are overlaid as dotted lines.

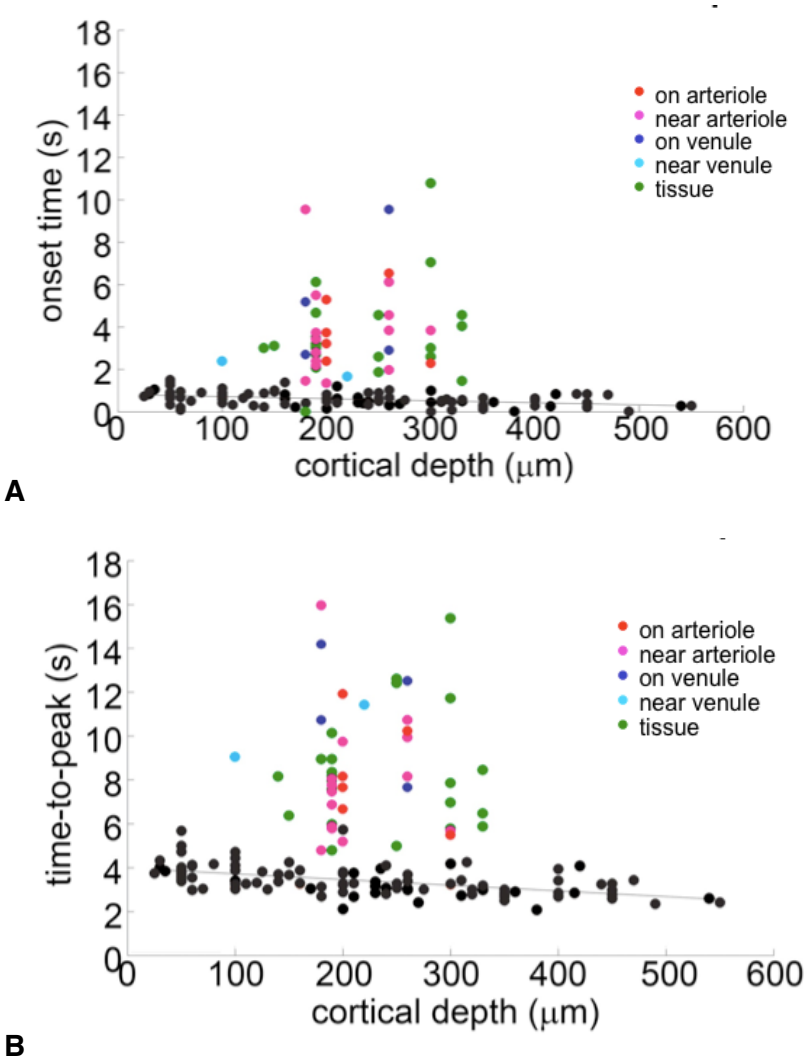

Figure 1.12 Comparison of onset and peak time distributions. Vascular (black) and astrocytic (color coded according to vessel relationship) measurements are overlaid. (A) Onset time as a function of the cortical depth. (B) Time-to-peak as a function of the cortical depth. Vascular and astrocytic measurements are overlaid.

Figure 1.13 (facing page) Measurement of evoked calcium response in astrocytic endfeet. (A) Composite 2-photon image of OGB and SR101 fluorescence at baseline. (B) A zoomed-in image of an astrocyte with its endfoot surrounding a diving arteriole. (C) Layer distribution of endfoot calcium responses. (D) Extracted time-courses from ROIs corresponding to the cell body and the endfoot. Individual stimulus trials are overlaid in black. The red curve represents the trial-averaged time-course. Arteriolar dilation is superimposed on the endfoot time-course in green.

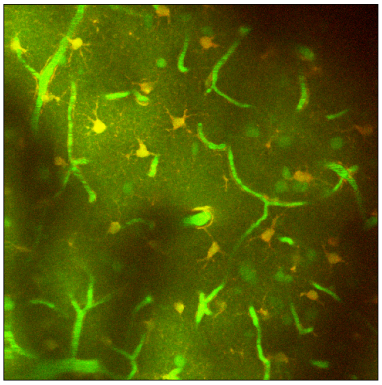

A

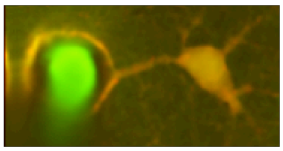

B

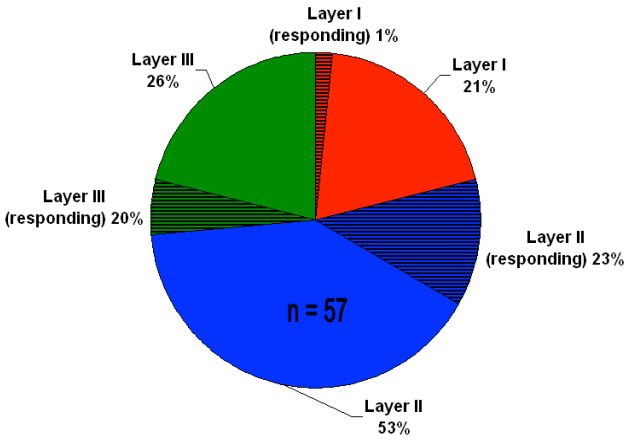
Layer I
(responding) 1%
Layer III
26%
Layer I
21%
Layer III
(responding) 20%
Layer II
(responding) 23%
n = 57
Layer II
53%

C

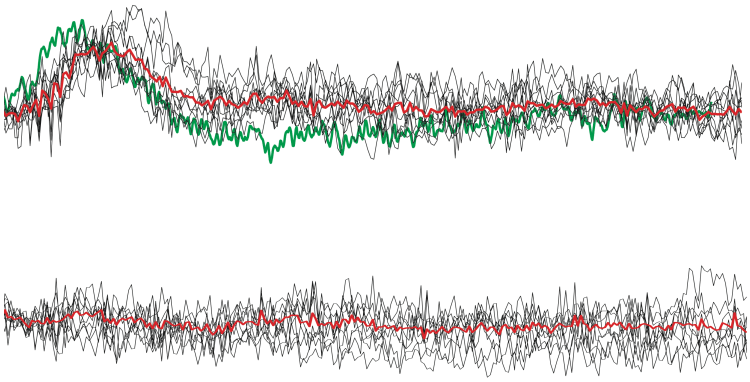

D

Among 57 cases where both the cell body and endfoot were imaged, only one had a calcium response in the endfoot in the absence of a response in the cell body (Fig. 1.11). The endfoot calcium response still had a significantly delayed onset relative to the simultaneously measured arteriolar dilation (Fig. 1.11 D).

In two cases, a calcium response in the endfoot was observed to slightly precede the response in the cell body (Fig. 1.7). However, in all cases the endfoot calcium increase was significantly delayed (~2 s) relative to the dilation onset, and as infrequent in occurrence as the somatic response.

In addition to the 2 second forepaw stimulus presented in the data here, we also attempted to stimulate the neuronal population for longer periods of time (4 s, 5 s, and 20s), to stimulate a different neuronal population (whisker barrel cortex), to vary the modality of stimulation (electrical, tactile, or air puff), and to stimulate the neurons under different anesthetic conditions (isoflurane, urethane, and ketamine/ xylazine). See Table 1-1 for the number of animals included in each set of experimental conditions. None of these changes to the experimental conditions produced any difference in the overall responsiveness of the astrocytes to neuronal activity. There was also no observable difference between the astrocytic calcium responsiveness in rat and in mouse somatosensory cortex.

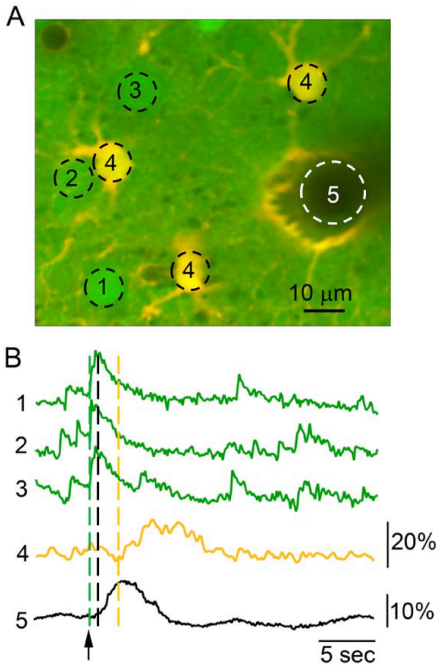

Figure 1.14 Neuronal (1-3, green) and astrocytic (4, yellow) calcium response time-courses in (B) were extracted from the corresponding ROIs indicated in (A). Diameter change of a diving arteriole (5, black) was measured simultaneously. The color-coded dashed lines in (B) indicate that the onset of astrocytic calcium response lags behind the onset of vasodilation.

Table 1-1 Number of animals in each experimental condition: varied type of anesthetic, stimulus modality, and stimulus duration. N = rat ; n = mouse.

	α-chloralose	**urethane**	**ketamine / xylazine**	**isoflurane**
forepaw / 2 sec	N = 1 ; n = 11		n = 2	n = 2
forepaw / 4 sec	n = 3	n = 3		
whisker pad / 2 sec	N = 1 ; n = 1		n = 2	
whisker pad / 5 sec	N = 4	n = 3	n = 7	n = 4
whisker (tactile)	N = 1			
whisker (air puff)	N = 1			n = 1

DISCUSSION

Within the center of cortical forepaw region in SI, small arterioles and their branches have a robust dilatory response to a brief (2s) stimulus. The onset of dilation following the stimulus onset varies as a function of the cortical depth: from ~0.5 s in layer IV to ~1 s close to the cortical surface. Similar observations of this depth effect on timing of the dilatory response have previously been made in the rat SI (Tian, 2010). The majority of astrocytes (91 %) do not exhibit reliable calcium transients temporally locked to the stimulus. When observed, the onset of astrocytic calcium response is delayed by > 2 s relative to the onset of arteriolar/capillary dilation. This slow and delayed astrocytic increase in intracellular calcium does not support the hypothesis that astrocytes trigger vasodilation and the associated blood flow response through calcium-dependent mechanisms. Given the significant temporal mismatch, astrocytes are unlikely to play a role in generation of the dilatory response to a brief stimulus in healthy subjects and, therefore, might not be relevant for interpretation of fMRI signals using event-related stimulus paradigms.

Limitations of past studies

A possible limitation of the previous study which reported robust astrocytic responses to sensory (whisker) stimulation (Wang, 2006) was the use of topical loading. This is an astrocyte-specific labeling method that uses prolonged incubation in high DMSO and pluronic detergent without the protection of the overlying dura. (See Chapter III for more discussion of the problems associated with using topically loaded calcium indicators such as Fluo-4) This method does not allow for the simultaneous optical monitoring of neighboring short latency neuronal calcium responses to verify tissue health and imaging quality in the targeted region of the somatosensory cortex. Network level astrocytic functionality is a complex

physiological phenomenon, contributing to the discrepancies in the literature. Much of the confusion over astrocyte function stems from a lack of standardization when it comes to the main tasks of studying calcium dynamics *in vivo*: anesthesia, loading of cells with an appropriate indicator, and subsequent interpretation of the signals that become visible.

One study stands apart from the others with respect to the kinetics of astrocytic calcium response (Winship, 2007). Using SR101 labeling to identify astrocytes, this study reported that a small percentage of astrocytes exhibited a fast response to hindlimb stimulation, similar to nearby neurons. This opens the possibility of heterogeneity within the astrocytic population. The other possibility is that a small percentage of SR101 labeled cells were actually neurons. While it has been shown that SR101 exclusively labels astrocytes using topical loading (Nimmerjahn, 2004), Winship et al. (2007) injected the dye into the tissue (Stosiek, 2003), and this might have resulted in a small subpopulation of neuronal uptake. The apparent fast response in a small number of astrocytes could also result from a technical error related to the employed subtraction procedure. Difference images were used to identify responsive astrocytic somata visible above the response of the neuropil. However, there remains the possibility of neuronal contribution to the astrocyte signal in (rare) cases where a neuron and an astrocyte overlap in the x and y dimensions, and share very close z-axis locations. Furthermore, given the spongiform nature of astrocytes, a contribution of neuropil signal to the astrocyte region of interest (ROI) cannot be entirely ruled out by simply applying a criterion of astrocytes having a greater stimulus-driven increase in fluorescence than surrounding neuropil. See Materials and Methods for discussion of neuropil contamination of the astrocyte signal and how it was separated from the true astrocytic response.

Astrocytic heterogeneity

Nevertheless, it is possible that astrocytes are heterogeneous across and within cortical layers. Specifically, the higher density of cytochrome oxidase in neurons in layer IV reflect the higher metabolism of this layer relative to the other layers (Woolsey, 1996). It is possible that astrocytes in layer IV may have faster or more efficient responses to elevated neuronal activity. Schummers et al. (2008) found that not only did astrocytes respond to visual stimuli individually (and not as a gap junction linked syncytium), but that they also shared the receptive fields of the surrounding neurons, often with sharper orientation tuning. Also of note is a recent in vivo study in olfactory glomeruli that demonstrated astrocytic calcium responses preceding vasodilation (Petzold, 2008) suggesting that neurovascular coupling in this specialized system might be different from SI.

Support for the neurogenic hypothesis of neurovascular coupling

Arteriolar smooth muscle cells express a variety of receptors for neurotransmitters and neuropeptides, suggesting that vascular diameters can be regulated independently of astrocytic activity (for review, see Hamel, 2004, 2006). The extensive innervation of cerebral blood vessels also suggests that neurons could be in direct control of local changes in CBF. According to the “neurogenic” hypothesis (Atwell and Iadecola, 2002; Iadecola, 2004; Logothetis, 2008; Lauritzen, 2005; Hamel, 2006) neuronal release of vasoactive messengers regulates vasodilation/constriction. In cortical slice work, it has been shown that evoked firing of single GABAergic interneurons in whole-cell recording was sufficient to either dilate or constrict neighboring microvessels. Specifically, the interneurons eliciting dilation expressed VIP and nitric oxide synthase (NOS) while those eliciting contraction expressed SOM and neuropeptide Y (Cauli, 2004). In fact, constrictions

appeared spatially restricted, maximal at the level of neurite apposition, and associated with smooth muscle contraction. Thus, it is an attractive proposal: neuronal signaling directly inducing vasodilation in a feed-forward, anticipatory manner.

Some neurotransmitters are directly vasoactive (Cauli, 2004; Hamel 2004, 2006) or trigger the synthesis of vasoactive messengers. For example, glutamate activates NMDA receptors that elevate intracellular concentration of calcium and trigger synthesis of a vasodilator nitric oxide (NO) by a neuronal enzyme called nitric oxide synthase (nNOS) (Iadecola and Niwa, 2002). Neuronal excitation is expected to cause dilation of surround arterioles. Application of the $GABA_A$ receptor agonist muscimol has been reported to cause dilation in brain slices (Fergus and Lee, 1997).

Inhibitory interneurons release, in addition to GABA, other signaling molecules called neuropeptides. Cortical interneurons containing the neuropeptides somatostatin and neuropeptide Y, also known as Martinotti cells, not only cause arteriolar vasoconstriction *in vitro*, but extend their axons to neighboring cortical columns, representing a good candidate for mediators of the phenomenon of "surround inhibition" (Devor, 2007). Indeed, *in vivo* imaging experiments have reported that surround inhibition was correlated with arteriolar vasoconstriction and a decrease in blood oxygenation ("negative BOLD") (Devor, 2007; Boas, 2008). Activation of these neurons is expected to result in surround vasoconstiction, but direct *in vivo* evidence showing that the selective activation of Martinotti cells, or release of somatostatin, correlates with vasoconstriction, remains lacking.

If neurotransmitter/neuropeptide release during synaptic transmission represents a critical factor in the generation of the hemodynamic response, then activation of the same cortical circuit by different inputs would be expected to lead to

different degrees of vasodilation and vasoconstriction, reflective of differential engagement of particular cell types. Experiments in vivo have shown that, indeed, vasodilation is replaced by vasoconstriction within the same forepaw area of SI following ipsilateral rather than contralateral forepaw stimulation. With contralateral forepaw stimulation, the circuit is excited by thalamic inputs to layer IV, while ipsilateral SI is activated via transcallosal afferents synapsing below and above layer IV.

Propagation of neuronal activity within a cortical column happens within a couple of milliseconds, while the hemodynamic response is delayed by approximately 500 ms. The onset of dilation in response to a brief single-whisker deflection occurs well past the return of neuronal activity to baseline. Therefore, laminar hemodynamic/vascular delays are unlikely to be explained by neuronal propagation between cortical layers. However, the magnitude of neuronal / neuropil response could potentially show laminar differences, increasing with increasing cortical depth, and thus, be negatively correlated with dilation onset time and time to peak. This potential relationship between neuropil and neuronal response, and microvasculature dilation would suggest that the magnitude of neuronal response may drive laminar differences in functional dilation onset.

Chapter II : In vivo functional NADH imaging with single-cell resolution confirms neural activity triggers neuronal followed by astrocytic oxidative metabolism

ABSTRACT

In vivo imaging of cell-specific metabolic activity is of key importance for understanding of a wide range of clinical conditions, such as: compromised blood perfusion following stroke, and the decrease in efficiency of single-cell respiratory processes that occurs in neurodegenerative diseases such as Parkinson's disease. However, *in vivo* imaging of metabolic activity at the single-cell level, with sufficient temporal resolution to resolve fast metabolic events related to ongoing neuronal electrical activity and neuronal responses to stimulation, remains an unmet challenge for today's imaging methods. Calcium transients reflect only one aspect of function (or dysfunction) of brain tissue. While a few recent studies have used calcium imaging in conjunction with intravenous injection of fluorescent dyes to track changes in vascular diameters and the velocity of blood flow, metabolic changes that accompany increases in neuronal activity have only been measured on the macroscopic scale. In Chapter 2, we report the application of TPLSM to functional imaging of intrinsic fluorescence of B-nicotinamide adenine dinucleotide (NADH) *in vivo* within single neurons and astrocytes in rodent primary somatosensory cortex (SI). This is done in order to investigate the metabolic responsiveness of astrocytes under the same conditions where a reliable calcium response was not observed, using NADH fluorescence as a biomarker for metabolic function. In the chapter that follows, we show that astrocytes reliably respond to neuronal activity with metabolic activity that fails to be reflected in their calcium dynamics.

INTRODUCTION

Information processing by neurons is metabolically expensive -- the brain accounts for 20% of the body's resting metabolism. The generation, processing, and transmission of action potentials by neurons requires a constant input of energy. 40-50% of total ATP produced in nervous tissue is used to maintain Na+, K+, and Ca2+ in electrochemical disequilibrium across the plasma membrane. Thus, one of the most important roles of astrocytes is to provide metabolic support for neurons. ATP synthesis in the brain occurs via both mitochondrial oxidative phosphorylation and cytosolic glycolysis. Glucose is the main source of energy for the brain, and enters through endothelial cells and astrocytic end-foot processes via the GLUT1 transporter. Alternatively, it may enter neurons directly via GLUT3. In astrocytes, glucose is used for glycolysis, producing lactate which is then transported out of the astrocyte via the H+ coupled monocarboxylate transporters (MCTs) MCT1 and MCT4. Extracellular lactate is transported into neurons via MCT2 and converted to pyruvate for use in the citric acid (TCA) cycle.

Neurons have a lower glycolytic rate than astrocytes, and prefer to use astrocytic lactate rather than producing it themselves. It has been shown that neurons can utilize lactate as their major metabolic substrate, while glucose is used for maintaining the neuron's antioxidant status through cellular functions such as the synthesis of NADPH(H^+), ribose-5-phosphate, and glycerol-borne lipids. This can be considered active down-regulation of glycolysis to spare neuronal glucose for non-bioenergetic purposes, and creates a neuronal dependence on astrocytic lactate. In addition, astrocytes are the only neuronal cell type capable of storing glucose as glycogen. Under hypoglycemic conditions and periods of increased tissue energy demand, astrocytic glycogen provides the energy substrate for the brain.

Since NADH is auto-fluorescent while NAD^+ is not, intrinsic NADH fluorescence is able to serve as an indicator of the cellular redox state. NADH is the principal electron carrier in glycolysis, the Krebs cycle, and the mitochondrial respiratory chain. During glycolysis, NADH is generated in the cytosol, and then directly, or via electron shuttles, transported into mitochondria. In mitochondria, NADH is oxidized to NAD+ in the electron transport chain, establishing a potential across the inner mitochondrial membrane which enables the production of ATP. Still within mitochondria, NADH is regenerated from NAD^+ through the TCA cycle. Conversion of pyruvate into lactate, with subsequent secretion of lactate into the extracellular space, also acts to decrease the NADH pool, but on a slower time scale (Hu and Wilson, 1997). Altogether, these relationships complicate the interpretation of the NADH/NAD^+ ratio. Still, the rates of both oxidation and reduction accelerate with an increase in the demand for metabolic energy that accompanies an increase in neuronal activity. However, during a transient metabolic response to neuronal perturbation, the rates are not exactly balanced. Since the NADH molecule is fluorescent while NAD^+ is not, a change in the ratio of NADH/NAD^+ can be observed as a change in NADH fluorescence.

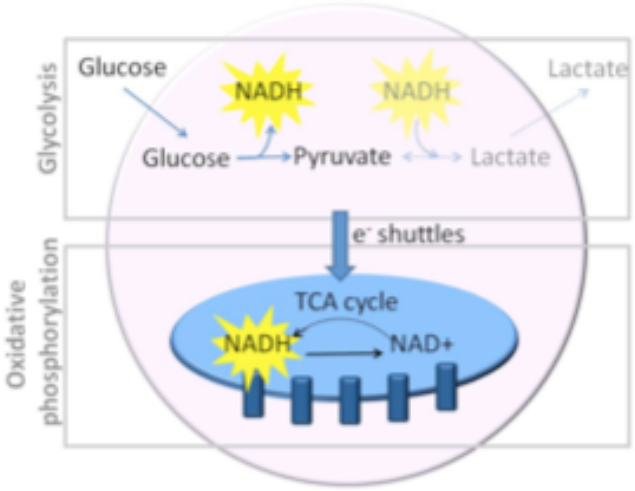

Figure 2.1 The NADH cycle. A diagram showing that a decrease in NADH fluorescence is attributed to mitochondrial respiration, while an increase - to glycolysis and regeneration in TCA cycle.

On the macroscopic level, it has been shown that NADH auto-fluorescence of brain tissue decreases in response to stimulation, cortical spreading depression, or seizures throughout the duration of the stimulus as far as blood flow is not compromised (Foster, 2005; Takano, 2007), and increases in response to hypoxia or ischemia (Mironov, 2001). On a microscopic scale, a recent study in hippocampal brain slice reported a higher resting NADH fluorescence in astrocytes than in neurons, as well as an astrocytic response to Schaffer collateral stimulation with an increase in NADH signal (Kasischke, 2004). NADH behavior in vitro may differ from in vivo because of the limited O2 availability in the absence of blood flow and O2 carriers (Devor, 2009).

Thermodynamic studies have shown that glycolysis (NADH production) occurs faster than the conversion of pyruvate to lactate (NADH oxidation). Empirical optical data show that changes in NADH fluorescence can be observed in neurons and astrocytes following an increase in neuronal activity (Kasischke, 2004; Takano,

2007). Previous studies *in vivo* and *in vitro* concluded that an increase in neuronal activity triggers a transient decrease in NADH fluorescence. The decrease in NADH signal may be followed by an overshoot above the baseline, a controversial finding that has been observed in vitro but not under normal conditions *in vivo.*

A number of hypotheses have been proposed to account for the time-course of the NADH response including differences in oxygen availability and possible specificity of the negative and positive signals to different cell types. However, the lack of direct in vivo measurements of the microscopic NADH response in neurons and astrocytes prevent validation of these hypotheses. The idea has been put forth that neurons use mostly oxidative phosphorylation while astrocytes use mostly glycolysis (Magistretti, 1999).

In agreement with this idea, 2-photon NADH imaging in astrocytes in brain slice revealed an early dip in NADH fluorescence, sensitive to blocking of postsynaptic neuronal activity, followed by an increase in fluorescence in astrocytes (Kasischke, 2004). However, it can be assumed that this was all done under conditions of limited O2 diffusion (deeper than 50um from slice surface, where neurons are minimally damaged by the slicing procedure). There remains the need to probe NADH dynamics in neurons and astrocytes under healthy conditions via in vivo 2-photon studies with cellular resolution.

MATERIALS AND METHODS

Mice and rats were anesthetized, the craniotomy performed over SI, and the general physiology monitored, as described in the Materials and Methods section of Chapter I. Heart rate, blood pressure, hemoglobin oxygenation and expired pCO_2 were continuously monitored to test for potential systemic effects. Imaging was done

within a 1mm radius from the center of neuronal response as determined prior to the imaging session by surface potential recordings. Astrocytes were labeled with a sulforhodamine dye (SR101) that specifically stains glia when applied topically. Since NADH is intrinsically fluorescent, no dye application was required for its visualization. Images were obtained using a 4-channel Ultima 2-photon microscopy system from Prairie Technologies. A 4x objective (Olympus, XLFluor4x/340, NA=0.28) was used to obtain images of the surface vasculature across the entire cranial window to aid in navigating and a 20x water-immersion objective (Olympus, XLUMPlanFI20x NA=0.95) for high-resolution functional imaging. The optimal 2-photon excitation for NADH is between 710-740 nm according to prior reports. Accordingly, all fluorophores were excited using 2-photon laser illumination at 740 nm, near the peak excitation of NADH. Although the 740 nm illumination is sub-optimal for calcium indicators, they still can be sufficiently excited.

Frame scans at a given depth (focal plane) were performed at >10 Hz to allow detection of neuronal spikes. To increase the number of simultaneously measured cells, line scan along a user-defined line in the focal plane ("free" line scan) was used. Lines were drawn through all cells in focus. In line scan mode we achieve temporal resolution of >10 Hz for simultaneous imaging of >50 cells.

Stimulation

The stimulation lasted 2 seconds and consisted of a train of 6 electrical pulses (3 Hz, 300 μs, ~1mA) with interstimulus interval (ISI) of 25 s delivered to a forepaw through a pair of thin needles implanted under the skin. In a separate set of experiments, stimulation lasted 5 seconds, consisted of a train of 15 electrical pulses (3 Hz, 300 μs, ~1mA) with ISI of 60 s delivered to the whisker pad through a pair of thin wires implanted under the skin. The intensity of the stimulus was adjusted to

provide stimulation below the movement threshold. Stimulation was presented using a separate PC that also acquired TTL timing signals for data acquisition ("trigger out" TTLs for each frame) using a National Instruments IO DAQ interface controlled by in-house software in Matlab. The TTL data were used to determine the timing of each frame relative to the stimulus onset during data analysis performed in Matlab.

The center of neuronal response to forepaw stimulation was mapped using surface potential recording. NADH and GFP were excited using laser illumination of 740nm and 905nm, respectively. SR101 has a broad 2-photon excitation spectrum and was visible at both illumination wavelengths. Fluorescein dextran (FITC) was injected intravenously following functional NADH imaging for easy registration of the measurement locations and prior electrophysiological surface potential mapping with respect to the cortical vasculature.

For functional NADH imaging, masks were defined corresponding to cell bodies of the inhibitory neurons and astrocytes based on GFP and SR101 fluorescence, respectively. Cell bodies of the excitatory (pyramidal) cells were defined as "black holes" in the composite GFP/SR101 image.

RESULTS

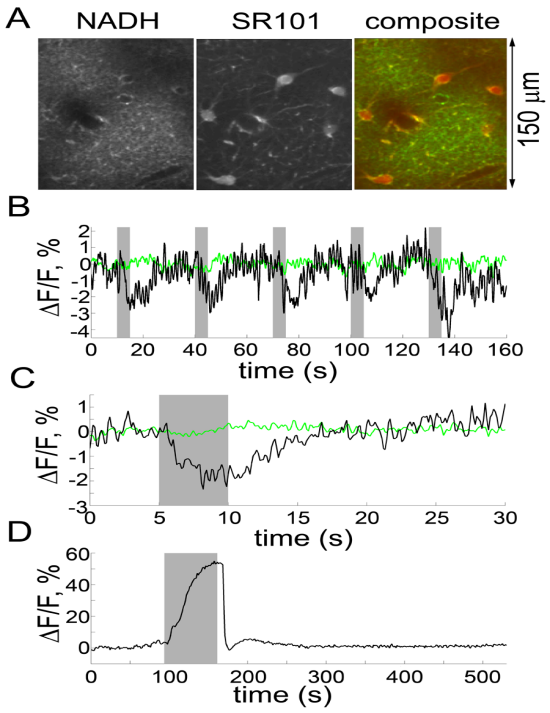

Figure 2.2 NADH imaging in vivo. (A) Corresponding NADH and SR101 images from the rat SI. (B) Time-courses of NADH (black) and SR101 (green) extracted from the entire image during 5 consecutive stimulus trials. C, Averaged response over 10 stimulus trials. D, NADH time-course during a 60-sec breath hold

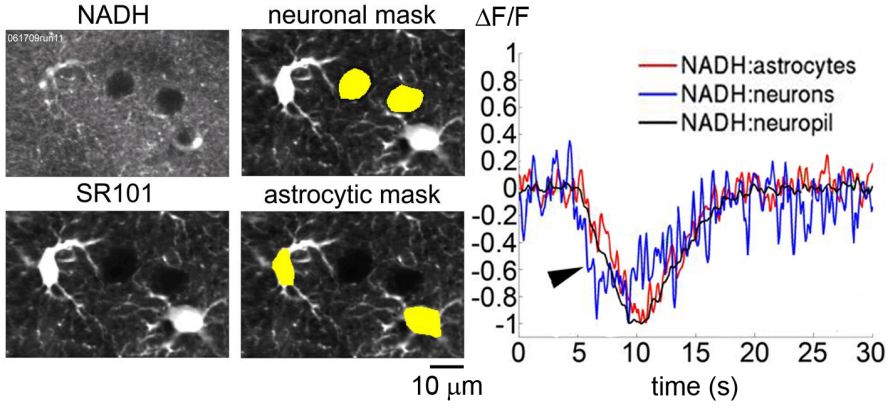

Figure 2.3 NADH fluorescence changes in nearby neurons and astrocytes evoked by the sensory stimulus. Left: Corresponding NADH and SR101 images and masks for extraction of time-courses. Right: Time-courses averaged over 9 trials. The arrow points to fast neuronal response.

Our data indicate that we can easily resolve astrocytic cell bodies and their proximal processes based on a higher resting level of NADH fluorescence in the cytosol (Figure 2.2 A). This is consistent with studies in isolated cells showing that a major fraction of astrocytic NADH is cytosolic. Single astrocytes have been resolved with TPLSM based on NADH fluorescence in a hippocampal slice preparation, but never before in vivo. Consistent with previous 1-photon studies that measured NADH fluorescence from the cortical surface in live animals, our 2-photon data demonstrated a decrease in NADH fluorescence of brain tissue in response to sensory stimulation (Fig. 2.2 B-C) and an increase in fluorescence in response to a respiration arrest (Fig. 2.2 D). On the level of singe cells, both neurons and astrocytes respond with a decrease in NADH fluorescence to a sensory stimulus under normal conditions (Fig. 2.3). Since activation of astrocytes depends on neurotransmitter release, their metabolic response is expected to be temporally delayed relative to that of neurons. Indeed, astrocytic decrease in NADH signal lagged ~ 1s behind neurons.

In vivo, hemoglobin in the microvasculature absorbs the illumination and emitted NADH fluorescence. In particular, vasodilation during the hemodynamic response causes an increase in the amount of red blood cells in the capillary bed above the imaging plane and leads to a transient darkening of the image. This effect is negligible near the top of cortical layer I but causes significant interference when imaging in layer II/III. To correct for the signal attenuation introduced by hemoglobin we have developed an algorithm that utilizes hemoglobin influence on a second, non-functional, fluorophore (e.g., SR101) that is detected simultaneously with NADH. The absorption of hemoglobin is wavelength dependent and is approximated by a linear scaling of the non-functional time-course with respect to extinction coefficient

of the absorbing medium. The scaled SR101 time-course yields the correction curve that is used to extract the true NADH functional signal. To validate the hemoglobin correction, we used an intravascular injection of a bolus of saline to dilute hemoglobin. This procedure resulted in brightening of the image of both NADH and SR101 yet did not affect the corrected NADH signal.

The optical design for detection of the emitted NADH fluorescence was further optimized by: (1) including optical filter selection (2) implementation of GaAsP photodetectors and (3) incorporation of a pulse splitter. The optimized filter design increased the efficiency of NADH detection by >20% in comparison with the filter used previously, while minimizing the overlap with calcium indicators (OGB) and SR101 (red). It should be noted that green calcium dyes such as OGB might absorb some of the NADH fluorescence; therefore an increase in OGB signal during the functional response can interfere with NADH detection. In the future, red calcium dyes such as X-Rhod-1 could be employed during simultaneous calcium and NADH imaging to avoid potential interference. The pulse splitter is expected to reduce the photodamage for a given laser power while taking advantage of the entire power range.

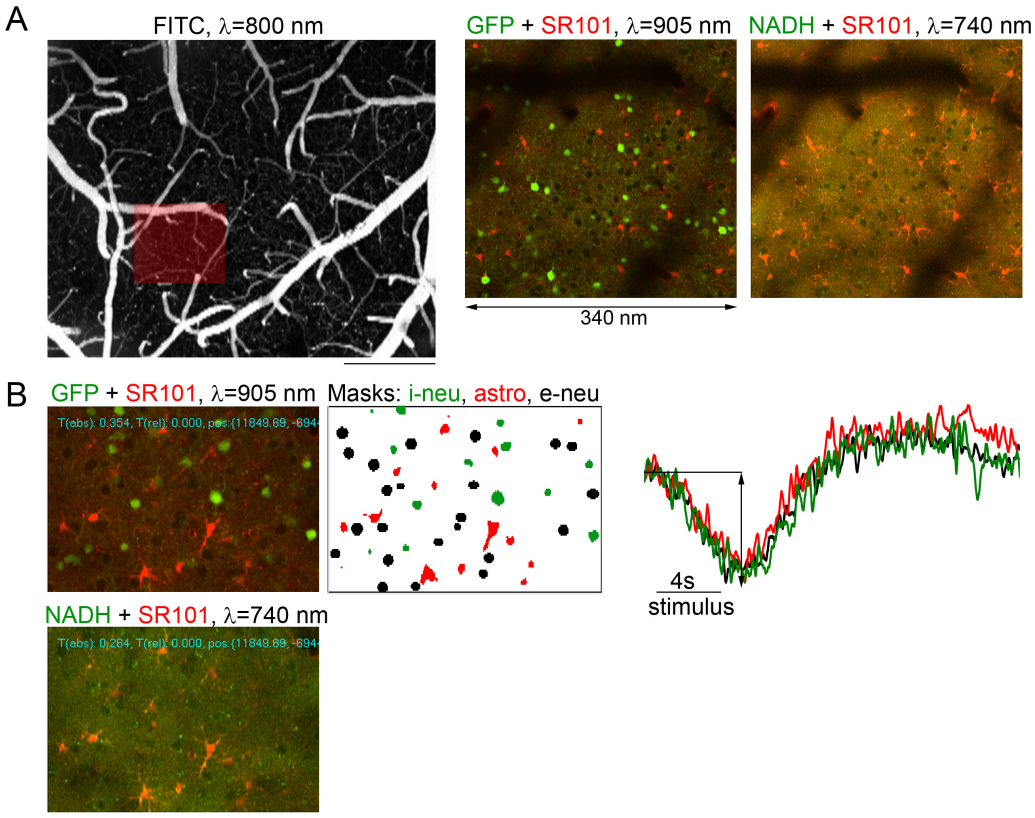

Figure 2.4 NADH imaging in GAD67-GFP mice. (A) Corresponding GFP/SR101 and NADH/SR101 images from cortical layer II, 150µm below the surface. The location within the exposure is indicated by the red rectangle on the vascular image on the left. (B) NADH imaging in response to sensory stimulation. Left: reference images; middle: masks for extraction of time-courses; right: trial-averaged time-courses (5 trials).

Consistent with our previous observations in the rat, NADH fluorescence decreased in response to stimulation in mice. The decrease was observed in all cell types: inhibitory neurons, pyramidal neurons and astrocytes. Also as was observed previously in the rat, astrocytic decrease in NADH followed that of neurons.

DISCUSSION

Our data show that neuronal electrical activity is accompanied by an increase in oxidative metabolism in neurons followed by that in astrocytes. This is the first time that neuronal and astrocytic metabolic activity has been imaged with single-cell resolution in intact cerebral cortex sufficiently fast to visualize a transient response to sensory stimulation. Furthermore, we have demonstrated our ability to perform NADH imaging in GFP-positive transgenic mice, where GFP expression can be used to define specific neuronal cell types. This is the first demonstration of specificity of the baseline and evoked NADH response to neuronal sub-types (inhibitory interneurons versus pyramidal cells). These results open an unprecedented possibility of studying in vivo metabolism in different neuronal cell types both at resting conditions and during neuronal activation.

The observed decrease in NADH fluorescence we report here does not rule out the presence of glycolysis, but does suggest that oxidative phosphorylation dominates the transient, stimulus-induced metabolic response in both neurons and astrocytes under normal physiological conditions. In agreement with an oxidative phosphorylation dominated metabolic response to increased neuronal activity, Lin et al. (2010) recently showed, using quantitative MRI and spectroscopy methods, that the increased energy demand produced by neuronal activation was linearly correlated with an increase in $CMRO_2$ (representative of aerobic metabolism). This implication is also consistent with the abundant presence of mitochondria in both neurons and astrocytes.

Additionally, it is interesting to note that the astrocytic increase in oxidative metabolism appears to lag behind the metabolic response of neurons to increased activity. According to the “metabolic” hypothesis of neurovascular coupling, the state

of neuroglial energy consumption directly determines the regional blood flow through the production of vasoactive metabolites (Magistretti, 2006). The delay reported here suggests that even under the metabolic hypothesis, temporally speaking, it is unlikely that astrocytes are responsible for the rapid coupling of neuronal activity to the CBF response. Furthermore, the observations we have made thus far indicate that an increase in neuronal activity is always accompanied by an increase in neuronal metabolism, astrocytic metabolism, and arteriolar vasodilation. However, none of these processes appear to require an astrocytic increase in intracellular calcium to occur.

The next step in the investigation of NADH as an intrinsic marker of metabolic response is further validation of the signal source. This will involve the use of pharmacological interventions to inhibit the mitochondrial respiratory chain, glycolysis, or to disrupt neuroglial communication. The contribution of oxidative metabolism can be tested by using sodium cyanide to block the mitochondrial complex V, which should force both neuronal and astrocytic glycolysis. This should be manifested as an increase in NADH fluorescence as has been observed in previous 1-photon studies (Galeffi, 2007). We hypothesize that blocking of the mitochondrial respiratory chain would not only lead to an increase in the baseline NADH fluorescence but also reverse the polarity of astrocytic NADH response to stimulation (from negative to positive). Although the previously reported “overshoot” in NADH fluorescence (Kasischke, 2004) was not detected here, the use of iodoacetic acid (IAA) (an inhibitor of the glycolytic catalyst glyceraldehyde 3-phosphate dehydrogenase) would further confirm an involvement of glycolysis if application of IAA increases the amplitude of the NADH dip.

To confirm the specificity of NADH signals to neurons and astrocytes, we will need to employ pharmacological manipulations aimed at disrupting neuroglial communication. Specifically, the application of MPEP (6-methyl-2-(phenylethynyl)-pyridine) and TBOA (DL-threo-β-benzyloxyaspartate) to block astrocytic glutamate sensors (metabotropic glutamate receptors 5 (mGluR5) and the glutamate transporter, respectively) should eliminate astrocytic but not neuronal NADH response to stimulation because astrocytes will not be able to sense an increase in neuronal activity.

It will also be of interest to compare baseline and stimulus-evoked NADH changes in neurons and astrocytes before and during induction of mild hypoxia. Imaging NADH fluorescence under conditions of compromised oxygen availability will discern between a glycolysis and an oxidative phosphorylation dominated response to stimulation. A transient increase in glycolysis will manifest as an increase in NADH fluorescence, while an increase in oxidative phosphorylation will manifest as a decrease. This will determine whether functional NADH imaging may be used as a biomarker for tissue hypoxia. The ultimate goal is to combine TPLSM imaging of NADH with simultaneous TPLSM imaging of calcium and hemodynamic activity. This tripartite imaging approach would open unprecedented opportunities to study the functional interactions within the neurovascular unit (NVU) from a new metabolic angle, and would allow a comprehensive assessment of NVU physiology or dysfunction.

Chapter III : Astrocytes sense and respond to their individual environments with spontaneous calcium activity within the astrocytic network

ABSTRACT

Astrocytes express numerous receptors that enable them to respond to virtually all known neuroactive compounds, including neurotransmitters, neuropeptides, growth factors, cytokines, small molecules, and toxins. The expression of such receptors allows astrocytes to sense and modulate the neuronal environment. In the past few decades, the idea of an astrocytic syncytium -- a multinucleate mass of cytoplasm resulting from the fusion of cells -- has fallen out of favor, and been replaced by the recognition that glia are organized into networks, interconnected by gap junctions, and capable of intercellular communication. Neuro-glial and glio-vascular interactions need to be considered at a network level, beyond a dialogue between single cells. In order to study the network level interactions of astrocytes, it is important to first understand the significant environmental cues affecting glial cell signaling. Without doubt, a multitude of factors come together to cause astrocytes to generate spontaneous intracellular calcium activity in healthy cortex (Nimmerjahn, 2004; Hirase, 2004) and intercellular calcium “waves” in diseased cortex (Kuchibhotla, 2009), the cerebellum (Hoogland, 2009), and the neural retina (Newman, 2009). We must begin the study of such “spontaneous” activity with the systematic variation of controllable experimental and physiological parameters. An event remains “spontaneous” only as long as its causes remain unattributed.

INTRODUCTION

Astrocytes are extensively connected by gap junctions, aqueous channels that connect the cytoplasm of adjacent cells and are permeable to positively or negatively charged molecules. They are responsible for the sharing of molecules up to 1-1.2 kDa and ~1.5 nm diameter in size, and may facilitate the diffusion of energy substrates (such as glucose) from vessels to neurons (Rouach, 2008). Gap junction channels are composed of connexins, which can be visualized by immunohistochemical staining in astrocytes that express GFAP, to reveal their expression between and within astrocytic domains and at contacts between endfeet that enwrap blood vessels. Gap junctions are evenly distributed along the astrocyte processes, often interconnecting adjacent astrocytic processes derived from the same cell. These 'reflexive' gap junctions could be a part of astrocytic microdomains and contribute to their integrative responses.

Different networks can be identified using fluorescent dye injection into a single cell. Injected dye will diffuse into adjacent cells if they are coupled by gap junctions. When performed in a brain slice from an hGFAP-eGFP mouse (in which the expression of enhanced green fluorescent protein is under the control of the human GFAP promoter) it can be demonstrated that not all eGFP positive astrocytes are dye coupled -- indicating the existence of multiple isolated (in terms of gap junction coupling) networks sharing the same cortical space.

Despite the abundance of immunohistochemical evidence of astrocytic networks, there is little *in vivo* evidence supporting the hypothesis that astrocytes form long-range signaling networks. Recently, Kuchibhotla et al. (2009) found that astrocytes in mice with cortical amyloid-β (Aβ) plaques showed functional coordination of their intracellular calcium signals at long distances. Furthermore,

they found that rare intercellular calcium waves, traveling up to 200 μm across the cortex at speeds of around 25 μm/s, could be observed in a subset of their transgenic mice expressing mutant human Aβ precursor protein (APP) and mutant presenilin 1 (PS1) (APPswe:PS1ΔE9) in neurons. These mutations lead to an increase in Aβ production and plaque deposition beginning at ~4.5 months of age. In mice with plaques, resting intracellular calcium concentration in astrocytes was higher than in wild- type animals. The same study also noted that calcium transients during an "intercellular calcium wave" were higher in magnitude than a typical spontaneous event, suggesting that the wave-like signal was different from that spread by non-wave activity. These rare intercellular, propagating calcium events are suggestive of an astrocyte-based network response to focal pathology. Thus, astrocytes form a structurally interconnected network, whose long-distance signaling properties, long demonstrated *in vitro*, have been proposed to be revealable *in vivo* only after "pathological trauma."

We sought to investigate the particular properties of "pathological trauma" which alter the astrocytic environment, and allow intercellular signaling to become visible. Given the sparse and irregular nature of spontaneous activity in astrocytes, and the lack of a direct way to manipulate input into the system, it is not possible to draw any direct conclusions regarding causality from the small sample of cells imaged in each field of view. We can, for now, only determine whether or not an individual cell is "active" or "quiescent" in terms of its level of calcium fluorescence. Such "active" cells showing intracellular calcium waves are the prerequisite components for "intercellular calcium waves." Thus, the proportion of "active" cells within a field of view is an important variable to measure when it comes to studying the environmental factors influencing astrocyte activity.

MATERIALS AND METHODS

C57/black 6 mice (n = 6) and APP(-/-) J9M mice (n = 14) (were anesthetized with either isoflurane (0.5-3% w/v), urethane (1.5 g/kg), or ketamine/xylazine (100mg/kg : 15 mg/kg). A craniotomy was performed over the region of the barrel cortex and the dura mater was removed as described in the Methods section of Chapter 1. Astrocytes were labeled with sulforhodamine 101 (SR101) and Fluo-4-AM (Invitrogen) that both selectively stain glia when applied topically. The mechanism behind this selectivity is unknown, but thought to be related to the presence of the glia limitans. The dye could be taken up by the glia limitans and transmitted throughout the astrocyte network via gap junctions. This loading method allows for visualization of only layer I/II (the top 50-150 μm) of cerebral cortex. Dye loading was accomplished via topical application and incubation in the dark, at room temperature, for 30 min in 40 μL of 100 μM green fluorescent calcium indicator Fluo-4-AM plus ~10 μM SR101, combined with 4 μL of 20% pluronic acid in DMSO. In one experiment, 8 μL of 20% pluronic acid in DMSO was added to the Fluo-4-AM / SR101 dye mixture.

In a separate set of experiments, mice were loaded with OGB via microinjection. The calcium indicator OGB (50 μg in 40 μL ACSF plus 4 μL of 20% pluronic acid in DMSO) was microinjected at the center of the neuronal response as determined by surface potential mapping performed immediately before the injection. SR101 was dissolved in ACSF, yielding a final concentration of ~10 μM and applied topically to the exposed cortex for 3-5 minutes, after which unbound dye was washed away with repeated applications of ACSF.

Images were obtained using a 2-channel Ultima 2-photon microscopy system from Prairie Technologies. A 20x water-immersion objective (Olympus,

XLUMPlanFI20x NA=0.95) and a 40x water-immersion objective (Zeiss, IR-ACHROPLAN 40x NA=0.80) were used for high-resolution functional imaging.

Stimulation

The stimulation lasted either 5 seconds, consisting of a train of 15 electrical pulses (3 Hz, 300 μs, ~1mA) with ISI of 60 s, or 2 seconds, consisting of a train of 6 electrical pulses (3 Hz, 300 μs, ~1mA) with ISI of 25 s, delivered to the contralateral whisker pad through a pair of thin wires implanted under the skin. The intensity of the stimulus was adjusted to provide stimulation below the movement threshold.

Stimulation was presented using a separate PC that also acquired TTL timing signals for data acquisition ("trigger out" TTLs for each frame) using a National Instruments IO DAQ interface controlled by in-house software in Matlab. The TTL data were used to determine the timing of each frame relative to the stimulus onset during data analysis performed in Matlab.

RESULTS

III-1 Topical loading of Fluo-4 makes astrocytes susceptible to 2-photon laser induced hyperactivity over long imaging periods

Topical Fluo-4 loading requires prolonged incubation time in a solution made up of 0.2% pluronic acid and 10% DMSO. The detergent effect of DMSO likely causes some damage to the integrity of the tissue beyond making it penetrable to the AM dye. To investigate the effects of prolonged incubation in detergent on astrocytic calcium dynamics, in one mouse the suggested (Ref.) 10% DMSO was doubled to 20% of the incubation solution. Out of 57 imaged astrocytes in that mouse, 27 (47%) exhibited one or more high amplitude (>20% ΔF/F) calcium oscillations, and were

therefore classified as “active.” This was a higher fraction of oscillating neurons than was observed in the rest of the Fluo-4 loaded mice (n = 4) in which, on average, 33% of imaged astrocytes were classified as “active” (n = 539 observed astrocytes) based on their spontaneous activity level during 5 trials of forepaw stimulation with 60 s ISI.

In a separate set of experiments (n = 2), duration of exposure to 2-photon laser imaging light was varied between 330 s and 660 s by consecutively imaging the same plane and field of view for either 5 or two sets of 5 stimulus trials. Figure 3.1 displays a characteristic example of two consecutive imaging periods of the same group of cells. During the first 330 s, spontaneous calcium transients were infrequent and irregular. During the second 330 s period of imaging, average baseline fluorescence increased compared to the first imaging period. The proportion of “active” cells increased in the set of second imaging sessions, from 35% active in the first imaging session, to an average of 49% in the second imaging session. The frequency of spontaneous calcium oscillations also increased (Figure 3.1B). In all cases, astrocytes did not appear to respond to the applied stimulus, regardless of the amplitude (varied between 0.6 mA and 4 mA) of electrical pulse which was delivered.

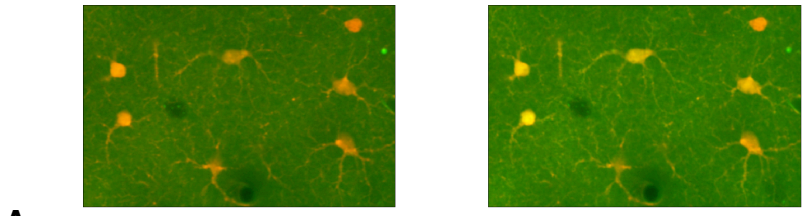

A

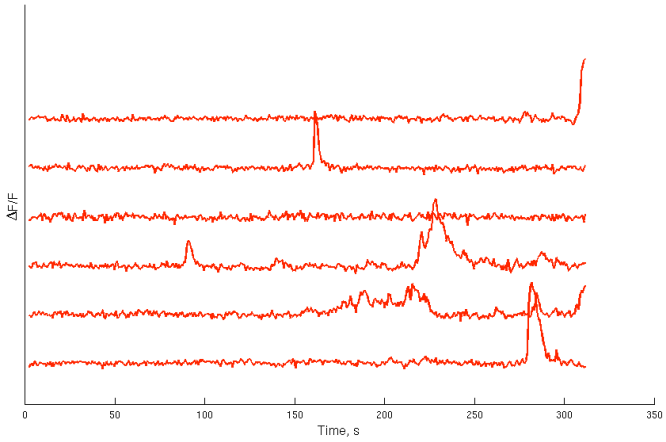

B

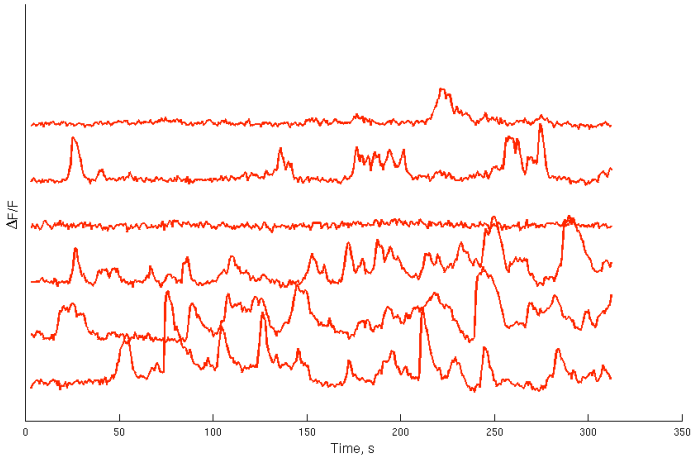

Figure 3.1 Topical loading of Fluo-4 makes astrocytes susceptible to 2-photon laser induced hyperactivity. (A) Baseline level of calcium fluorescence increases with prolonged imaging time. The image on the left is a composite of Fluo-4 and SR101 fluorescence, averaged over the entire duration of the first imaging period (330 s). The image on the right is fluorescence averaged over the duration of the consecutive imaging period (330 s). (B) Calcium time-courses extracted from each labeled cell in the field of view, expressed in % change relative to the pre-stimulus baseline.

Spontaneous calcium transients increased in frequency with prolonged imaging time. This is in agreement with previous reports that increased laser power can cause an increase in spontaneous calcium oscillations and waves (Wang, 2006; Helmchen, 2008), and further underlines the importance of keeping laser power as low as possible to avoid the generation of artifacts, especially when using Fluo-4 as the calcium indicator.

III-2 Astrocytic calcium oscillations in response to acute insult

In the next set of experiments, mice were anesthetized with ketamine/xylazine throughout both surgery and imaging, and loaded with OGB via bolus microinjection. In the vast majority of cases, calcium activity in astrocytes was extremely sparse, despite the robust responses to whisker stimulation visible in neighboring neurons and surrounding neuropil.

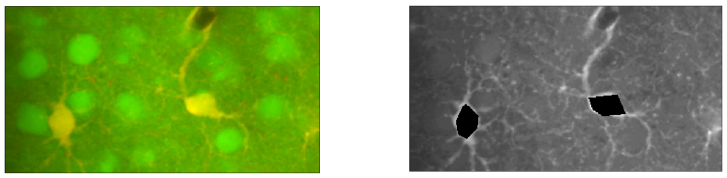

A

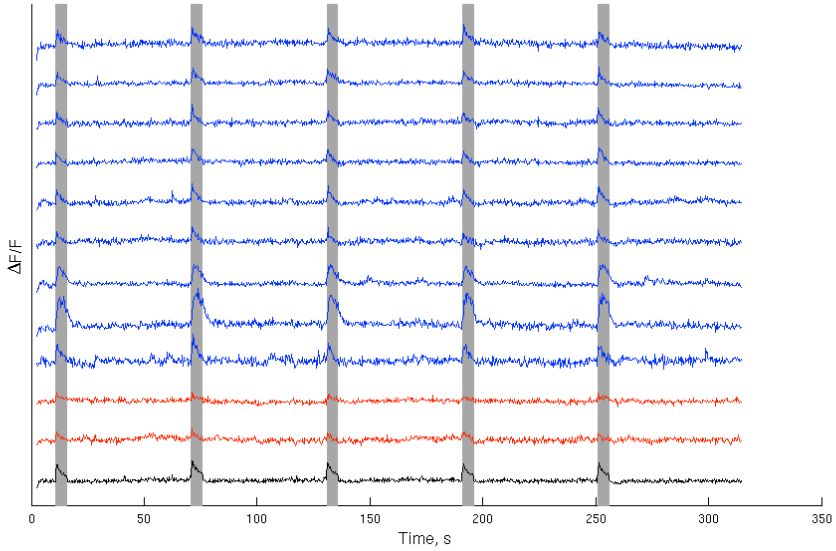

B

Figure 3.2 Astrocytic silence in the presence of robust neuronal and neuropil response to whisker stimulation. (A) Composite image of OGB and SR101 fluorescence on the left; masked regions of interest (ROIs) in black, corresponding to individual astrocytic domains on the right. (B) Calcium fluorescence time-courses extracted from each astrocytic domain, expressed in % change relative to the pre-stimulus baseline. Red = astrocyte, blue = neuron, black = neuropil. The stimulus durations are overlaid as vertical gray bars.

However, out of the 7 animals imaged under ketamine/xylazine anesthesia, 2 exhibited increased frequency of large amplitude astrocytic calcium transients. The two potentially acutely injured animals exhibited an average of 59% (n = 172

astrocytes) “active” astrocytes, as opposed to only 16% (n = 380 astrocytes) in the other five mice. The following figures are example sets of calcium time-courses from those two acutely injured mice during five consecutive 5 s stimulations (15 pulses, 3Hz, 300 µs, ~1.0mA).

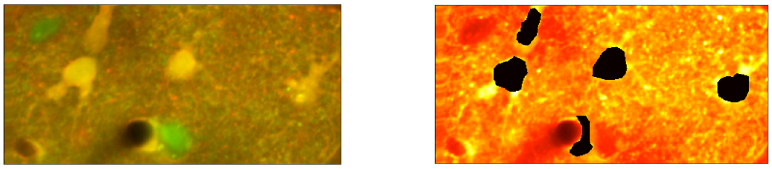

A

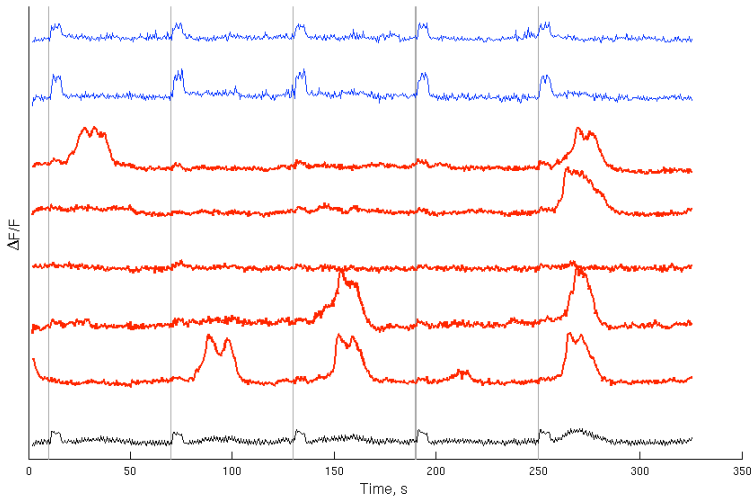

B

Figure 3.3 In acutely injured mouse cortex, astrocyte calcium oscillations in response to whisker stimulation occur with varying frequency and timing. (A) Composite image of OGB and SR101 fluorescence on the left; masked regions of interest (ROIs) in black, corresponding to individual astrocytic domains on the right. (B) Calcium fluorescence time-courses extracted from each astrocytic domain, expressed in % change relative to the pre-stimulus baseline. Red = astrocyte, blue = neuron, black = neuropil. The stimulus triggers are overlaid as vertical gray bars. Activity of each individual astrocyte appears independent of activity in its closest neighbors.

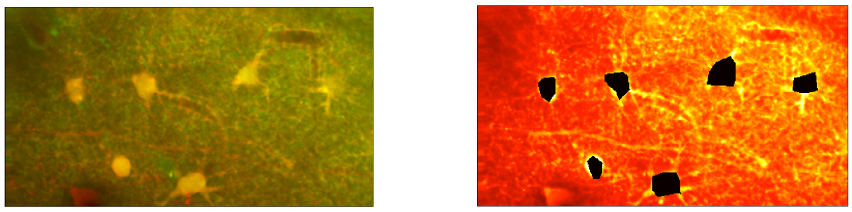

A

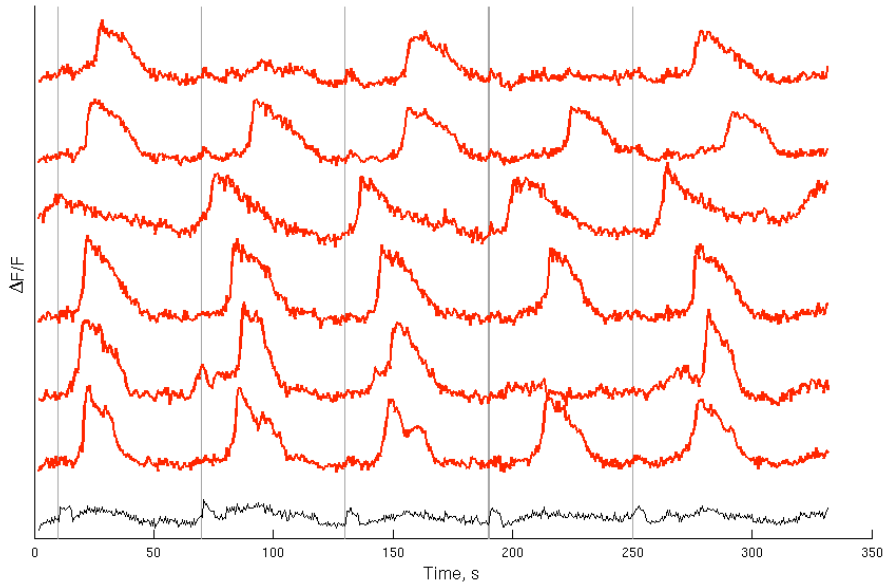

B

Figure 3.4 In acutely injured mouse cortex, astrocytic calcium oscillations appear periodic, each cell oscillating at its own particular frequency. (A) Composite image of OGB and SR101 fluorescence on the left; masked regions of interest (ROIs) in black, corresponding to individual astrocytic domains on the right. (B) Calcium fluorescence time-courses extracted from each astrocytic domain, expressed in % change relative to the pre-stimulus baseline. Red = astrocyte, black = neuropil. The stimulus triggers are overlaid as vertical gray bars.

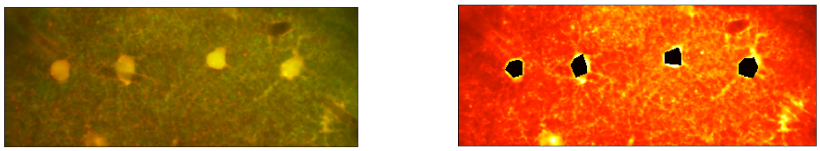

A

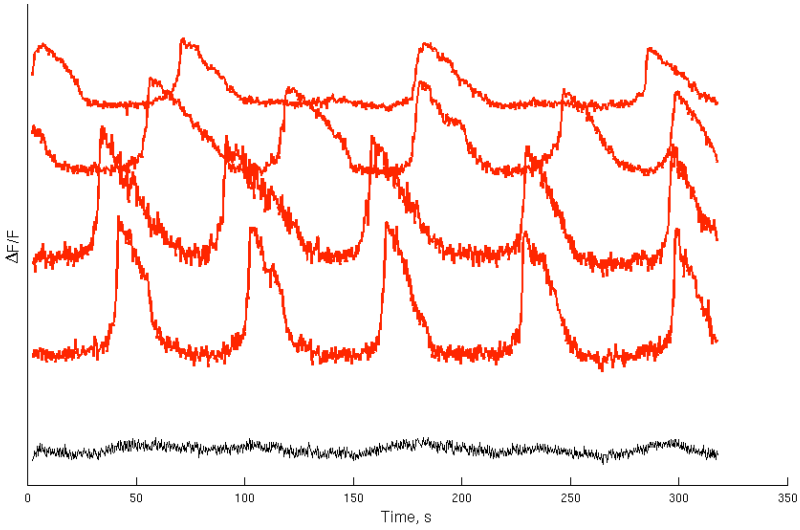

B

Figure 3.5 Astrocytes in the acutely injured mouse cortex oscillate in the absence of physiological stimulation. (A) Composite image of OGB and SR101 fluorescence on the left; masked regions of interest (ROIs) in black, corresponding to individual astrocytic domains on the right. (B) Calcium fluorescence time-courses extracted from each astrocytic domain, expressed in % change relative to the pre-stimulus baseline. Red = astrocyte, black = neuropil.

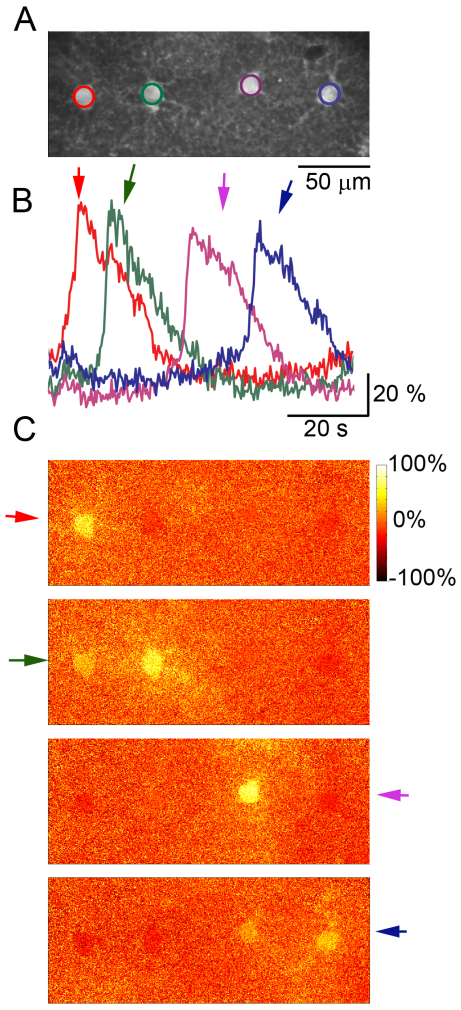

Figure 3.6 Time-series of calcium fluorescence images taken from a field of four astrocytes in which activity appears to propagate as a calcium wave across the field of view. (A) Grayscale image of SR101 fluorescence used to create masks (colored circles) of ROIs. (B) Average calcium time-courses calculated for each ROI in (A), expressed in % change relative to the pre-stimulus baseline. (C) Individual frame-shots from the time-series of images taken at the peak of each time-course.

In fact, what looks like a “wave” may not necessarily be a traveling / diffusive signal being propagated between cells, but rather, could be a momentary alignment of individual patterns of intrinsically oscillatory behavior in neighboring cells, as is seen in the group of cells in (Fig. 3.7).

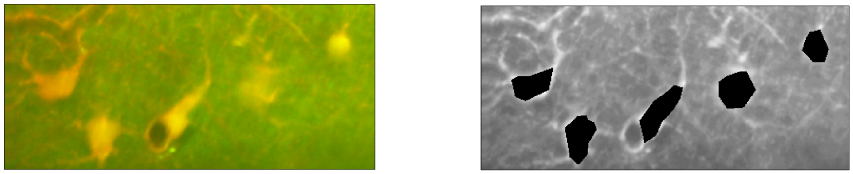

A

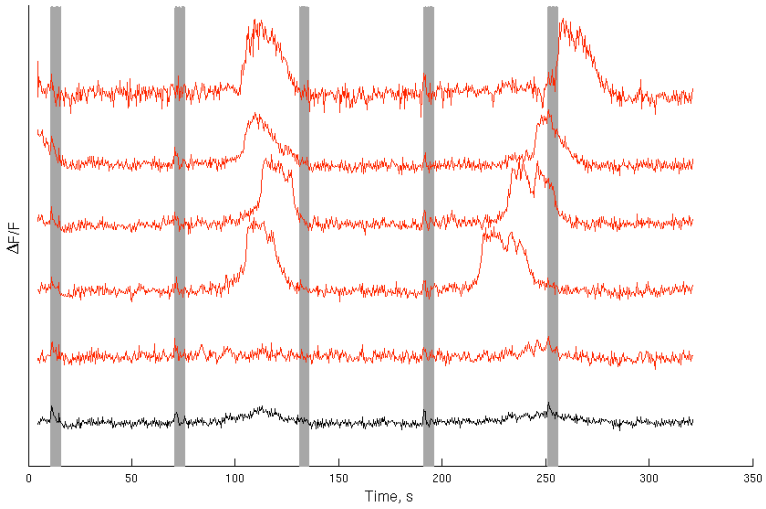

B

Figure 3.7 A “wave-like event” might not really be a wave, but a chance alignment of the activity of individually oscillating cells. (A) Composite image of OGB and SR101 fluorescence on the left; masked regions of interest (ROIs) in black, corresponding to individual astrocytic domains on the right. (B) Calcium fluorescence time-courses extracted from each astrocytic domain, expressed in % change relative to the pre-stimulus baseline. Red = astrocyte, black = neuropil.

DISCUSSION

We further investigated the potential function of astrocyte as sensors of environmental change or pathological insult. First, we demonstrated that the use of the Fluo-4 calcium indicator dye must be regarded with caution, as it may make astrocytes more susceptible to heat/laser induced hyperactivity and intracellular calcium oscillations. Second, we found evidence of intracellular calcium oscillations and wave-like calcium activity *in vivo* in wildtype mouse cortex, calling into question the type of environmental conditions that are necessary to stimulate network level functional activity. Rather than being an AD plaque related phenomenon, our findings suggest that intercellular calcium "waves" can occur in response to cues on multiple time scales -- to acute injury as well as chronic pathology. The act of injection (at multiple sites in the cases illustrated in this chapter) of calcium indicator dyes, capillary bed damage during surgery, and tissue integrity degradation by incubating in soap, may all be forms of acute, localized pathological insult capable of triggering intercellular calcium waves in astrocytes.

The recent observations of spontaneously occurring *in vivo* calcium waves in diseased cortex (Kuchibhotla, 2009), cerebellum (Hoogland, 2009), and retina (Kurth-Nelson, 2009) bring to light the functionality of glial cells at the network level. Rather than being a product of artificial stimulation, or an artifact of *in vitro* conditions, as was once thought, network-level activity in astrocytes can now be considered fully physiologically relevant, and potentially very important to a broader understanding of the normal function of astrocytes in the brain.

This group of three studies, however, were very different in terms of their observations, and bring up several interesting questions regarding the cellular basis

and basic characteristics of “waves.” First, a comparison of size and rate of expansion yields interesting differences between the three types of glial cells: cortical astrocytes, Bergmann glia, and retinal Muller cells. In the retina, they found that spontaneous waves in the isolated retina were more regular in size and rate of expansion than waves *in vivo*. Maximal spread of waves both *in vivo* and in the isolated retina was around 70 μm, at an average speed of 24 μm/s. However, they also claimed that the waves spread concentrically for 4-8 s and contracted for 5-10 s following, indicating that there was significant variability in individual wave spreading speeds, as the maximum distance would be reached within just 3 seconds of spread if it traveled at the average speed that was reported. In the cerebellum, waves spread anisotropically through ellipsoidal domains around 3500 μm^2 in area, which equals in volume a sphere of radius around 29 μm. Speed of spread decreased with distance from the center, dropping to ~60% of originating speed within 40 μm. Velate astrocytes in the cerebellar granular layer also showed transglial waves with expansion time around 2.5 s and radius of around 25 μm. In the AD cortex, maximal spread of waves was around 200 μm, at approximately the same speed that has been reported for *in vitro* calcium waves, around 22 μm/s, with multiple directionality. The “waves” we encounter here appear to occur sporadically in the midst of increased spontaneous calcium oscillations. A combination of these characteristics, they travel slower, at around 5-10 μm/s, but also encompass further distances (> 200 μm), lasting around 25 s.

Only the retinal and cerebellar studies reported on the rate of spontaneous wave generation. In the cerebellum, within the same field of view, they found 0.4 waves per min of observation. In the retina, they stated that 15 spontaneous waves occurred in 60 s, but also report an age-related trend in rate of wave generation,

ranging from 0.27 per min per mm^2 in young rats to 1.0 per min per mm^2 in 120 day old rats. In vivo, the age related trend still held, ranging from 0.6 to 6.5 waves per min per mm^2. Our observations, similarly, in 6-9 month old mice, had oscillations occurring approximately once every minute.

The work in the cerebellum holds significant interest due to the fact that it claims to provide evidence of non-pathological, purinergic release driven, spontaneous calcium wave events. They argued that the introduction of calcium sensor via the viral injection route was a less invasive approach that still yielded repeated ellipsoidal waves similar to their results in the rat, where they engaged in multi-cell bolus loading of microinjected calcium dye. However, simply because viral loading is a means of obtaining measurements without acute introduction of a dye-containing electrode does not mean that the tissue does not get damaged by the viral injection, or respond to the pathology of being infected with virus. The argument that calcium waves could represent a general response to pathological insult still holds.

Chapter IV : Mapping the spatiotemporal dynamics of calcium signaling in cellular neural networks using optical flow

ABSTRACT

An optical flow gradient algorithm was applied to spontaneously forming networks of neurons and glia in culture imaged by fluorescence optical microscopy in order to map functional calcium signaling with single pixel resolution. Optical flow estimates the direction and speed of motion of objects in an image between subsequent frames in a recorded digital sequence of images (i.e. a movie). Computed vector field outputs by the algorithm were able to track the spatiotemporal dynamics of calcium signaling patterns. We begin by briefly reviewing the mathematics of the optical flow algorithm, describe how to solve for the displacement vectors, and how to measure their reliability. We then compare computed flow vectors with manually estimated vectors for the progression of a calcium signal recorded from representative astrocyte cultures. Finally, we applied the algorithm to preparations of primary astrocytes and hippocampal neurons and to the rMC-1 Muller glial cell line in order to illustrate the capability of the algorithm for capturing different types of spatiotemporal calcium activity. We discuss the imaging requirements, parameter selection and threshold selection for reliable measurements, and other perspectives on uses of the vector data

Beginning with an analysis of the expression patterns of astrocyte-specific genes in retinal Muller cells as well as astrocytes of the inner plexiform layer, the molecular underpinnings of generalized “reactive” processes involved in the pathogenesis of common neurological disorders are explored. Until recently, it was believed that the roles of glia in the brain included merely providing structural and

chemical support for neurons, as well as general housekeeping functions such as uptake of potassium after neuronal action potentials. In fact, it has been found that astrocytes can respond to neuronal action potentials by binding glutamate to mGluRs. The overexpression of glutamate receptors in astrocytes has been observed specifically in epileptic tissue. Modeling has consistently indicated that a condition of persistent spiking, similar to that observed in epilepsy, can be elicited in systems where the glutamate receptors on astrocytes are over-expressed. A potential role for neuro-glial signaling in modulating neuronal dynamics at local and distant synapses has been suggested in numerous modeling studies. Experimentally observed as well as mathematically modeled network dynamics in astrocytes and Muller cells of the retina from animal models of neurological disease may be used to delineate between specific cellular and molecular aspects of glial change which are causative versus reactionary to disease.

INTRODUCTION

Calcium signaling is an intermediate step in many of the signaling pathways in neurons and glial cells and is informative of functional neural activity. In neurons calcium signaling precedes subthreshold and threshold (i.e. action potential) changes in membrane voltage, and can be used to infer electrophysiology from optical imaging (Tian, 2006; Canepari, 2008; Yaksi, 2006; Vogelstein, 2009). In astrocyte glial cells it underlies the mechanisms by which these cells communicate in astrocyte networks and in bi-directional communication with neurons (Agulhon, 2007; Bennett, 2005; Scemes 2008). Relative changes in cytosolic calcium concentration can be measured using different fluorescence indicator dyes that can be imaged by optical microscopy in the visual light range, such as bulk loaded AM esters and genetically encoded calcium indicators (Paredes, 2006; Smetters, 1999). The emitted fluorescence of indicator dyes change as a function of the relative amount of free calcium ions individual indicator molecules are able to interact with. Although the relationship between measured fluorescence signals and the calcium levels that produce them is complex and non-linear, it is assumed that there exists a correlation between measured changes in emitted fluorescence by indicator molecules and differing cytosolic calcium concentrations. In this context, the measured fluorescence signal provides a valuable qualitative metric of changing calcium levels that allow inferences of cell signaling and function. Throughout the rest of this chapter, we will use the terms “calcium signal" or “calcium fluorescence" to mean a measured calcium indicator fluorescence signal that reflects a relative cytosolic calcium concentration, as is routinely implied in the literature, even though in practicality we never know the real, i.e. absolute, free ion concentration that gives rise to the measured fluorescence signal.

The data collected by a typical experiment records qualitative movies of imaged changes in calcium fluorescence intensity. One can visualize calcium transients and their relative positions and durations, but there is no inherent quantitative analysis of the data by the experiment itself that allows one to derive the dynamics that characterize such signaling events. Things such as propagation speeds and directions (i.e. velocity), the kinetics of measured waveforms, or analysis that depend on such properties, such as identifying and mapping the signaling geometry of intercellular calcium waves in networks of neurons or astrocytes. Measuring and tracing calcium (or other second messenger) fluorescence signals quantitatively from recorded movies manually is a tedious and labor intensive process for even small data sets, and involves comparing intensities at different frames and locations in order to calculate speeds and directions. It is generally not possible to do so for large data sets that encompass high spatial and temporal resolution detail or large numbers of cells interacting in a circuit or network. This can be addressed by analyzing experimental data with a filter algorithm called optical flow, which can be used to derive quantitative measurements of observed spatiotemporal calcium signals imaged from fluorescence movies. The resultant vector data has a variety of uses, ranging from deriving basic measurements of signal velocity and direction, to characterizing and classifying spatiotemporal calcium dynamics between different experimental conditions. Optical flow is an imaging technique (i.e. a filter) that calculates a two-dimensional displacement field between two subsequent frames in a movie, based on the local spatial and temporal gradients of the two images.

The optical flow filter originated in the computer vision field, where it was designed to approximate object motion in time-ordered image sequences for

applications like stereo disparity measurements, motion estimation, movie encoding and compression, and object segmentation (Horn, 1981). The algorithm uses a computed local spatial and temporal gradient to approximate a displacement or flow vector at each pixel in the image. In both neurons and glial cells cytosolic calcium concentration changes manifest themselves as transient responses with a rapid increase, i.e. rising phase, followed by a kinetically slower decaying phase. This is because free calcium is cytotoxic and therefore kept at nanomolar concentrations in the cytoplasm under normal conditions. It is only transiently elevated followed quickly by its re-uptake or extrusion. Temporal changes are typically coupled to spatial changes as a signal propagates through a cell. Measured fluorescence changes then trace specific paths during periods of observation (c.f. Fig. 4.1). Calcium transients start at a particular location, travel in some direction at a specific speed and terminate at a different location. The typical kinetics of calcium transients in neural cells are particularly well suited to the computational requirements of the optical flow algorithm. We have successfully applied optical flow to calcium fluorescence movies and obtained displacement vectors that track the spatiotemporal progression of calcium signals. The filter works for calcium fluorescence data because calcium signals exhibit both spatial and temporal gradients. The computed vectors provide point estimates of the speed and direction of signals. Optical flow is ultimately an imaging filter that works on whole movies, much like edge filters and image segmentation filters are used in static microscopy (Guo, 2004; Mukamel, 2009; Hashemi, 2008), and provides a novel and automated way of analyzing the spatiotemporal dynamics of calcium intracellular signaling in neurons and astrocytes. We begin by briefly reviewing the mathematics of the optical flow algorithm, describe

how to solve for the displacement vectors, and how to measure their reliability. We then compare computed flow vectors with manually estimated vectors for the progression of a calcium signal recorded from representative astrocyte cultures. Finally, we applied the algorithm to preparations of primary astrocytes and hippocampal neurons and to the rMC-1 Muller glial cell line in order to illustrate the capability of the algorithm for capturing different types of spatiotemporal calcium activity. We discuss the imaging requirements, parameter selection and threshold selection for reliable measurements, and offer perspectives on uses of the vector data.

IV-1 Optical Flow Algorithm and Computation

In this section we briefly introduce the concepts and mathematics of optical flow, focusing in particular on our own implementation of the algorithm to the experimental data that follows in the Results section. The theory behind the algorithm is well established and the interested reader is referred to a number of excellent texts on the subject (see for example (Horn, 1981; Jahne, 2005)). Optical flow is an algorithm that operates at the pixel level and calculates local displacement or velocity between time ordered image pairs. Optical flow (or equivalently image flow) is the perceived motion of an object in a field of view (e.g. by the human eye or a camera), defined as the flow or change in space and time of gray values at the image plane. It is an estimation of the motion field, which is the actual motion of the object in three dimensional space projected onto the image plane (i.e. what we would like to know). As long as the frequency of successive frames in an image sequence is shorter than the motion or displacement of the object of interest (in order to avoid confounding ambiguities in detecting the components of the motion caused by aperture and correspondence problems- see (Horn, 1981; Jahne, 2005)), the optical

flow algorithm is able to track the motion of objects in the field of view as a function of changing gray scale levels, subject to appropriate constraints and minimizations. In other words, the algorithm assumes that any changes in gray values are due to the object moving, and that the irradiance of the object is constant from frame to frame. (This is actually a weak assumption that is difficult to satisfy since motion usually causes changes in irradiance, which is why the algorithm is an estimation of the motion field. In cases where irradiance does not change, the optical flow exactly equals the motion field.) The algorithm assumes the conservation of gray levels in the field of view and assumes that any changes in the distribution of gray levels are due to motion. In fact, the optical flow constraint equation (introduced below) can be derived by analogy from the continuity equation in fluid dynamics that conserves mass (Jahne, 2005). By computing the optical flow for all pixels in a field of view, displacement vectors can be calculated for each pixel that map where an object moved to from the pixel in the first frame to that in the second. Intuitively, one can see why the algorithm performs best with objects that have strong contrasts at boundaries or large signal to background noise ratios. The kinetics of calcium transient signals display clearly distinguishable rising and decaying phases that trace specific paths during periods of observation in the form of intracellular calcium waves (Fig. 4.1) that are readily detectable by the algorithm.

The underlying assumption for computation is to constrain local temporal gradients to the product of spatial gradients and displacement vectors. The basic principle of the algorithm takes as inputs two images and computes a vector for each corresponding pixel in the images which approximates the displacement of a small window surrounding that pixel between the two images (Fig. 4.2). Only intensity values inside the window are used for computing the pixel displacement value, so

the measurement is localized. Adjacent pixels will have overlapping windows, so their computed vectors will be similar, much like pixels in a blurred image are similar.

Following a mathematical description of the algorithm we describe the method for its solution and implementation that we used to derive the optical flow for calcium signals. We also discuss parameters and constraints of relevance to calcium fluorescence movies.

Consider an arbitrary pixel with gray level intensity I(x, y, t), displaced in the xy plane by ∂x and ∂y at time t in an n x n window Ω (Fig. 4.2b). This implies that

$$I(x, y, t) = I(x + \delta x, y + \delta y, +t + \delta t) \tag{1}$$

A first order Taylor series approximation of I(x, y, t) by expansion of the right side of (1) results in

$$I(x + \delta x, y + \delta y, +t + \delta t) = I(x, y, t) + \frac{\partial I}{\partial x}\delta x + \frac{\partial I}{\partial y}\delta y + \frac{\partial I}{\partial y}\delta y + \text{higher order terms} \tag{2}$$

Ignoring higher order terms, which provide negligible contributions, and taking into consideration equation (1)

$$\frac{\partial I}{\partial x}\delta x + \frac{\partial I}{\partial y}\delta y + \frac{\partial I}{\partial t}\delta t = 0 \tag{3}$$

Dividing by ∂t

$$\frac{\partial I}{\partial x}\frac{\delta x}{\delta t} + \frac{\partial I}{\partial y}\frac{\delta y}{\delta t} + \frac{\partial I}{\partial y} = 0 \tag{4a}$$

$$\frac{\partial I}{\partial x}u_x + \frac{\partial I}{\partial y}u_x + \frac{\partial I}{\partial y} = 0 \tag{4b}$$

The two spatial and one temporal gradients are defined by $\frac{\partial I}{\partial x}$, $\frac{\partial I}{\partial y}$, and $\frac{\partial I}{\partial t}$, respectively. $u_x = \frac{\delta x}{\delta t}$ and $v_y = \frac{\delta y}{\delta t}$ represent the x and y spatial components of the optical flow displacement vector $\mathbf{u}(x, y) = (u_x, v_y)$. The basic optical flow formulation is to constrain temporal intensity changes (gradients) to the product of spatial gradients and $\mathbf{u}(x, y)$ to give equation 4. In more compact notation this can be written as

$$\nabla I(x,y,t) \cdot \mathbf{u}(x,y) + \frac{\partial I(x,y,t)}{\partial t} = 0 \quad (5)$$

Computing optical flow means finding the values of **u**(x, y) at each location for every time point that satisfy the above constraint, given the known local image intensity spatial and temporal gradients.

Two factors establish computability of meaningful non-zero flow vector values. First, local spatial gradients must be non-zero at the point of interest (x, y, t). There has to be some image information around the pixel of interest, meaning that neighboring points have to have different values so that gradients are non-zero. If all pixels in a window around (x, y, t) have the same intensity values, then spatial gradients are zero and motion is undetectable by any means. Second, for displacement between subsequent frames to be computed, there has to be a temporal gradient at (x, y, t), or some change in intensity between time points. If there is no temporal change in intensity between subsequent time points, then a value of **u**(x, y) = 0 satisfies the constraint equation in (5). Both of these requirements are limitations on the original application of the optical flow when estimating displacement in natural scenes: objects may have constant intensity in a small window and still be moving, meaning that motion may occur and the recorded intensity spatial and temporal gradients equal zero. These limitations are less important when optical flow is applied to calcium fluorescence movies.

There are many methods for calculating optical flow for recorded movies (see (Barron, 1994) for a review), and all of them work on digitized movies with discrete pixel values of position and time, i.e. (x, y, t) (*columns, rows, frames*). We chose the Lucas and Kanade method because it is conceptually simple and efficient, and flexible in terms of the image processing steps required for computation (Baker,

2004; Baraldi, 1996; Lim, 2005). First, computation of the flow vector **u**(x, y) is performed on a window or spatial neighborhood Ω of arbitrary size, centered around (x, y), which is more reliable than a single point estimate at (x, y). Second, a window function *W*(x, y) is defined to favor values in the center over those near the edges. The constraint equation is redefined as a weighted least-squares t of local first-order constraints to a constant model of a local **u**(x, y) in each small spatial neighborhood around the pixel of interest. The goal is to find the value of **u**(x, y) that minimizes

$$\sum_{(x,y)\in\Omega} W^2(x,y)\Big(\nabla I(x,y,t)\cdot\mathbf{u}(x,y)+\frac{\partial I(x,y,t)}{\partial t}\Big)^2 \tag{6}$$

The above equation can be rewritten and solved as the linear system:

$$A^T W^2 A\cdot\mathbf{u}(x,y,t)=A^T W^2\mathbf{b} \tag{7}$$

Where, for neighborhood Ω, consisting of n points centered around the pixel and time of interest (x, y, t), Ω = {(x_1, y_1, t), (x_2, y_2, t), . . . , (x_n, y_n, t)}:

$$A=\begin{bmatrix} \frac{\partial I}{\partial x}(x_1,y_1,t) & \frac{\partial I}{\partial x}(x_2,y_2,t) & \dots & \frac{\partial I}{\partial x}(x_n,y_n,t) \\ \frac{\partial I}{\partial y}(x_1,y_1,t) & \frac{\partial I}{\partial y}(x_2,y_2,t) & \dots & \frac{\partial I}{\partial y}(x_n,y_n,t) \end{bmatrix}^T \tag{8}$$

$$W=diag\big[W(x_1,y_1),\dots,W(x_n,y_n)\big] \tag{9}$$

$$\mathbf{b}=-\Big[\frac{\partial I}{\partial t}(x_1,y_1,t),\dots,\frac{\partial I}{\partial t}(x_n,y_n,t)\Big]^T \tag{10}$$

Ω is usually a square window with sizes typically ranging from 3 x 3 to 15 x 15 or n = 9 to n = 225 points. We have set the weight matrix *W* to a two dimensional Gaussian σ^2 equal to 1/6 of the window width. As an example, for a 5 x 5 or n = 25 point window:

$$W=\frac{1}{1000}\begin{bmatrix} 1 & 6 & 13 & 6 & 1 \\ 6 & 54 & 112 & 54 & 6 \\ 13 & 112 & 230 & 112 & 13 \\ 6 & 54 & 112 & 54 & 6 \\ 1 & 6 & 13 & 6 & 1 \end{bmatrix}$$

Here, the center values in W have a greater contribution to the calculation than the edge values, favoring gradient values at the pixel of interest. Solving for the flow vector **u**(x, y) in equation (7), yields:

$$\mathbf{u}(x,y) = \left[A^T W^2 A\right]^{-1} A^T W^2 \mathbf{b} \tag{11}$$

Equation (11) describes a linear system in matrix form, where the flow vector u at spatial and time location (x, y, t) is solved from the quantities of A, W, and **b**, defined from the spatial and temporal derivates of n points around (x, y, t). The 2 x 2 matrix $[A^TW^2A]$ matrix contains all the image spatial derivatives, and if those values are close to zero, the matrix is poorly conditioned, and flow estimates become unreliable. Ensuring that both eigenvalues of the $[A^TW^2A]$ matrix are sufficiently large is a good way to ensure that the matrix is well conditioned, since a measure of the conditioning number is the ratio of the largest to the smallest eigenvalue (Barron, 1994). While this is not the only way to compute conditioning, this is the test we used for visualization and measurement reliability of computed vectors for calcium fluorescence data.

Spatial and temporal derivates were computed using 2 x 2 convolution kernel filters, where the ** operator denotes 2-dimensional discrete convolution:

$$\frac{\partial I(x,y,t)}{\partial x} = I(x,y,t) ** \frac{1}{4}\begin{bmatrix} -1 & 1 \\ -1 & 1 \end{bmatrix} \tag{12}$$

$$\frac{\partial I(x,y,t)}{\partial y} = I(x,y,t) ** \frac{1}{4}\begin{bmatrix} -1 & -1 \\ 1 & 1 \end{bmatrix} \tag{13}$$

$$\frac{\partial I(x,y,t)}{\partial y} = \frac{1}{\Delta t}\big(I(x,y,t+\Delta t) - I(x,y,t)\big) ** \frac{1}{4}\begin{bmatrix} 1 & 1 \\ 1 & 1 \end{bmatrix} \tag{14}$$

Here Δt represents the time between frames or the frame rate 1/Δt. Since the temporal derivative calculated in (14) forms the basis for the **b** vector in (11), the frame rate has a linear effect on the magnitude of the flow vector **u**.

Optical flow outputs a displacement vector in units of pixels, normalized to the time difference between the two frames used for computation. When normalized, the vector takes on velocity units of pixels per frame (for this reason it is called a flow vector). The conversion to physical units will depend on the spatial resolution of the camera and microscope, typically expressed in microns per pixel, and the sampling rate for the movie capture, expressed in frames per second. Spatial resolution is a function of the objectives used as well as the resolution of the imager and any pixel binning used. The frame rate is limited at the high end by the camera sampling rate, and at the low end by the minimum exposure time required to capture a detectable intensity signal. The exposure time may be reduced by increased gain or pixel binning, but those come at a cost of reduced resolution or increased noise. The conversion between units of pixels/frame and units of microns/second is straightforward:

$$\frac{microns}{second} = \frac{pixels}{frame} \cdot \frac{frames}{second} \cdot \frac{microns}{pixel} \tag{15}$$

While the optical flow algorithm produces vectors in units of pixels/frame, the analysis of the data in the Results section below have been converted into physical units of microns/second, using the resolution and capture rate of the recordings given the specifics of our imaging system. The Lucas-Kanade method was chosen because it is a relatively simple way to calculate flow vectors, allowing a variable window size, a weighing function that can be designed to favor gradient values near the center, and a measure of how reliable the flow vectors are by means of the eigenvalue calculation. The choice of window size will depend on a variety of factors. It must be large enough to capture the apparent displacement across frames and small enough to resolve features of interest. The capture frame rate must be fast

enough for displacements to be observable within the width of the spatial observation window across successive frames. When measuring the spatiotemporal motion of calcium signals the size of the window , the frame rate, and the resolution are all deeply tied to the size of the cells or cellular compartments in which the signal travels. Together, these parameters must be chosen so that the signal is observable and smooth enough to measure reliably as flow vectors across frames. For example, the choice of parameter values used to image calcium signals in part of a dendrite or a fine astrocyte process will necessarily be different than parameter values for broad calcium signals that fill the soma.

MATERIALS AND METHODS

Cell Preparations

rMC-1 glial cells and primary spinal cord astrocyte cultures (the latter dissected and grown similar to previously described (Silva, 1998; MacDonald, 2008) were grown to approximately 80% confluency and washed twice with Kreb-HEPES buffer (KHB) solution (10 mM HEPES, 4.2 mM $NaHCO_3$, 10 mM glucose, 1.18 mM $MgSO_4$, $7H_2O$, 1.18 mM KH_2PO_4, 4.69 mM KCL, 118 mM NaCl, 1.29 mM CaCl2, pH 7.4) and incubated with 5M Fluo-4 AM in KHB for 1 hr at room temperature. Excess dye was removed by washing twice with KHB and an additional incubation of 30 min at room temperature was done to equilibrate intracellular dye concentration and ensure complete intracellular hydrolysis. Synchronized calcium transients were initiated by mechanical stimulation of a single cell using a (0.5m i.d.) micropipette tip (WPI Inc., Sarasota FL) mounted on a M325 Micrometer Slide Micromanipulator (WPI Inc., Sarasota FL). Comparable data were obtained using adenosine triphosphate (ATP) pharmacological stimulation.

For hippocampal cultures, dissociated hippocampal neurons from timed-pregnant embryonic day 18 (E18) Sprague-Dawley rats were cultured on glass bottomed tissue culture dishes coated with poly-D-lysine and laminin (BD Biosciences, San Jose, CA). Cultures were plated at a cell density of 106 cells/ 3.8 cm^2. Cultures were maintained at 37ºC in 5% ambient CO_2. Plating media was composed of basal medial Eagle (Invitrogen, Carlsbad, CA) with 1X Glutamax, 1000 U/mL penicillin and streptomycin sulfate, 5% FBS, and 1X N2 supplement. Culture media consisted of Neurobasal (Invitrogen, Carlsbad, CA) with 1X Glutamax, 1000 U/mL penicillin and streptomycin sulfate, 20mM glucose, and 1X B27 supplement. Culture media was supplemented with 10uM Ara-C for 24 hrs at 1day *in vitro* (DIV) to inhibit overgrowth of glia. All imaging was performed on 3-5 DIV.

Bulk loading of hippocampal cell cultures was accomplished via incubation in the dark, at room temperature, for 30 min in 1M of the fluorescent Calcium indicator Fluo-4-AM in Krebs-HEPES buffer (10 mM HEPES, 4.2 mM $NaHCO_3$, 10 mM glucose, 1.18 mM $MgSO_4$, $7H_2O$, 1.18 mM KH_2PO_4, 4.69 mM KCL, 118 mM NaCl, 1.29 mM $CaCl_2$, pH 7.4), followed by 2 x 5 min washes in Krebs-HEPES with 100 µM sulfinpyrazone. Hydrolysis was allowed to proceed for an additional 30 min. Stimulation of neurons with glucose was performed by microinjection of 100 µL of 10mM glutamate in PBS from a specified-side of the culture dish, well outside of the microscope field of view. The fluorescence signal generated across the monolayer of cells was recorded for 10 sec prior to glutamate injection, and for 120 sec following injection. Cultured neurons were incubated for 30 min prior to imaging in Mg^{2+}-free PBS to induce the synchronization of calcium transients.

Imaging Setup

Visualization of calcium indicator dye fluorescence was achieved using a 488 nm (FITC) filter on an Olympus IX81 inverted fluorescence confocal microscope (Olympus Optical, Tokyo, Japan) that included epifluorescence, confocal, phase, bright field, and Hoffman differential interference contrast (DIC) modalities. Real-time movie recordings of calcium transient propagation were acquired with a Hamamatsu ORCA-ER digital camera (Hamamatsu Photonics K.K., Hamamatsu City, Japan) and Image-Pro Plus data acquisition and morphometric software (version 5.1.0.20, Media Cybernetics, Inc., Silver Spring, MD) or LabView custom written data acquisition software (ScopeController). All images were captured with a 10X objective, using a 2x2 binning on the camera, for a resolution on 1.3m/pixel and a total image size of 612x572 (camera's maximum resolution is 1224x1144). Images were sampled at frequencies ranging from 2 to 16.4Hz, or 0.5sec to 0.06sec exposure time.

RESULTS

IV-2 Comparison between computed and manually estimated flow vectors

We manually estimated flow vectors for 12 images equivalent to 6 seconds of calcium signaling in primary dissociated spinal cord astrocyte cultures (orange arrows in Fig. 4.3), and qualitatively compared them to computed optical flow vectors for the same data (green arrows in Fig. 4.3; note that only reliable vectors are shown as determined by the eigenvalue test- c.f. equation (11), see above). Manual estimation required stepping through frames and approximating roughly how a calcium signal progressed in time, which in this experimental preparation included intercellular calcium waves that propagated through a subset of the cell network. The manually traced signals were not the only ones observable in the small movie

sequence used, but were chosen to illustrate four representative signaling paths. Manual estimation was performed in two second intervals, estimating the incremental spatial progression of a given calcium signal across four frames.

Estimation of the flow or displacement of a cell signal such as calcium between frames manually like we did for the data in Fig. 4.3 is a very tedious and labor intensive process, and can only realistically be done under very sparse conditions where the observer can clearly delineate the flow of the signal visually. It is nearly impossible to do at the pixel or small window level. In contrast, optical flow calculates a displacement vector for every pixel in every frame, operating at a much finer scale and capturing much more detail than is possible with manual estimates.

Nonetheless, in Fig. 4.3 for the purpose of qualitatively validating derived optical flow vectors to manually estimated ones, in both cases there was a clear overlap in vector direction between manual and flow vectors. Vector magnitudes were more different between the two cases, which is consistent with the fact that the manual estimates spanned four frames while optical flow vectors were calculated across adjacent frames. There is also temporal overlap between the two cases, in the sense that similar displacements were estimated for the same frames using both approaches. The eigenvalue threshold masked out unreliable vectors, and this correlated well with calcium activity; only areas of spatial and temporal changes in the movie produced reliable vectors as assessed visually, which is ultimately the most accurate estimator of complex motions, but only if given the right conditions (e.g. conditions that allow the human eye to separate motion). The optical flow algorithm however, is able to provide reliable quantitative measurements of signaling dynamics at spatial and temporal scales simply not measurable by qualitative visual inspection or manual estimations of the data.

IV-3 Optical flow characterization of intercellular signaling

We applied the optical flow algorithm to typical calcium fluorescence movies of spontaneously forming sparse networks of neural glial cells and neurons in culture, and looked at the dynamics of intercellular signaling following pharmacological or mechanical stimulation. We purposely chose sparse networks because it facilitates the visual interpretation of the entire resultant vector field, but the algorithm itself can operate on any data that displays an appropriate signal. We recorded movies from the rMC-1 Muller glial like cell line, which mechanistically displays calcium signaling similar to Muller retinal glial cells *in vivo* (Yu, 2009), primary dissociated spinal cord astrocytes, and primary dissociated hippocampal neurons. Intercellular calcium waves in rMC-1 cells and astrocytes were mechanically induced by gently poking an initial cell without penetrating the cell membrane, while calcium waves in neuronal networks were induced by the localized pharmacological application of glutamate to one or a small group of cells (see the appendix below for details about experimental preparations and imaging parameters). In particular, intercellular calcium waves in astrocytes and related anatomically specialized macroglial cells such as Muller cells in the neural retina or Bergman glia in the cerebellum have been known to occur under experimental conditions for several years now, and have recently been shown *in vivo* under both physiological and pathophysiological conditions in different parts of the brain, mediated by intracellular calcium transients that induce paracrine signaling, primarily through adenosine triphosphate (ATP) [19, 20, 14]. Astrocyte and related macroglial cells engage in bi-directional chemical signaling with neurons and have the ability to modulate and directly participate in information processing in the brain, which necessitates more than just interactions between neurons and almost certainly involves astrocytes somehow. The functional roles of glial intercellular

calcium waves and their contributions to modulating neuronal information are not yet known, and in fact the dynamics of these signaling events and the conditions under which they occur are just beginning to be explored.

The key parameter for computing optical flow using the Lucas-Kanade method is the window size , specified as a square of a given width (see above). It defines the local neighborhood of pixels along a point of interest that is used to compute the spatial and temporal gradients required for the calculation. Though not required for computation, a minimum value for the eigenvalues for the matrix $[A^T W^2 A]$ should be specified to mask out unreliable measurements. This ensures that only reliable displacement vectors are computed. Table 4-1 shows the window sizes, eigenvalue thresholds, and capture frame rates used to calculate the vector fields shown in Fig 4.4. The displacement vectors can be converted into velocity by equation (15).

Table 4-1 Image capture and optical flow parameters for shown figures

Parameter	rMC-1 Cells	Astrocytes	Hippocampal Neurons
Frame Capture Rate (Hz)	16.4	8	4
Window Size (pixels at 1.3μm/pixel)	11	9	11
Minimum Eigenvalue - (λ_1, λ_2) greater than	11	1.4	.3

Neuronal cultures displayed derived optical flow vectors along processes as the calcium signal propagated throughout the network. As expected, computed vectors and the resultant vector field followed the geometry of connected processes (i.e. axons and dendrites) in the sparse network (Fig. 4.4a). The pattern of activation in this example proceeded diagonally from the site of stimulation in the upper left

hand corner of the field of view. Some neurons activated at considerably longer times following the stimulus (i.e. out to 7 or 8 seconds) most likely due to recurrent feedback signaling in the network which can last several seconds. Note how since only reliable vectors are plotted, as determined by the eigenvalue test, there are spatial discontinuities in the temporal progression of mapped signals, which reflect areas where the algorithm could not compute reliable vectors given the measured data. This may be especially true at lower magnifications as in the example shown here for comparatively large fields of view that capture many cells. This represents a challenging task for the algorithm. Nonetheless, both the spatial and temporal progression of calcium signals are easily visible. The computed data, being in vector form, can complement existing methods like cross-correlation that use only cell body data to establish relationships between cells for example.

Signal flow patterns were also computed for astrocyte and rMC-1 glial networks (Fig. 4.4b and c, respectively). Astrocyte signaling showed rapid burst like radial patterns that was mostly complete by 2 seconds, with some smaller regions of cells activating later as far out as 6-7 seconds. This is consistent with descriptions of intercellular calcium waves reported previously (Cornell-Bell, 1990; Newman, 1997; Allen, 2005). rMC-1 cells showed qualitatively similar radial patterns of activation, with signaling occurring within about 3 seconds following stimulation. However, unlike the astrocyte response, where there was uniform signaling across the network near the site of stimulation, rMC-1 cells showed more heterogeneity in spatial activation patterns, with distinct clusters of cells activating and spreading calcium waves. The distances traveled by the waves in the rMC-1 example roughly agree with previous quantitative characterizations of calcium waves in similar preparations, on average displaying wave distances of about 60 μm over the first 2 seconds or so

and distances between 50-100 μm over about 4 seconds (Yu, 2009). It is interesting however that the spatial progression of the calcium signals in this example was not linear as a function of time, in the sense that cells roughly equidistant from the site of stimulation activated at different times, within about 1 second for some versus about 3 seconds for others. The relationship and dynamics between the spatial versus temporal properties of such waves are difficult at best and usually not possible to determine by visual inspection of recorded movies alone, and are not captured by calculations such as the one dimensional signaling speed of a progressing wave front. Furthermore, speed and distance calculations of neuronal and glial signaling across networks of cells are usually corse approximations computed using low magnification movies that provide a sufficiently large field of view. In contrast, optical flow provides reliable single pixel vectors for any sized region of interest that represent very fine grain detailed descriptions of calcium signal propagation difficult to achieve otherwise. For the astrocyte data from Fig. 4.4b, Fig. 4.5 illustrates the distribution of signaling speeds in m/second for 65 optical flow vectors for a small 10 x 10 pixel region equivalent to a 13 x 13 μm region in the field of view (orange box in the figure). Any region size of interest anywhere in the imaged field that might be of functional interest to the investigator can be similarly characterized. By way of rough comparison, optical flow calculated speeds for calcium signals in computed window were distributed from 1-5 μm/sec, and are roughly similar to those reported previously using more approximate and global methods, in the range of 5 to 10 μm/second (Cornell-Bell, 1990; Newman, 1997; Allen, 2005).

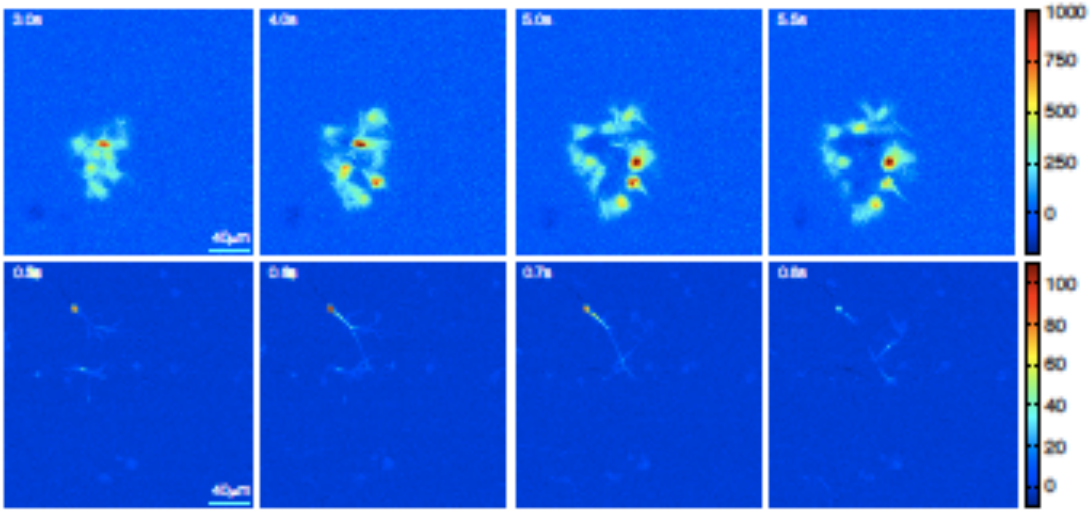

Figure 4.1 Selected frames from recorded movies of imaged calcium fluorescence activity in spontaneously forming sparse networks of primary dissociated hippocampal neurons (top) and cortical astrocytes (bottom). The color coded scale bars on the right represent fluorescence intensity *I* in units of Δ*I*/sec, as a first derivative of the calcium signal. For both cell types, signaling was spontaneous (i.e. inherent to neurons and pharmacologically induced in astrocytes under conditions that mimic the pathophysiology of Alzheimer's disease. Fluorescence increases followed a relatively smooth spatial progression across the frames at the times indicated by the time stamp in the upper left hand corner of each image. Areas of increasing calcium concentration appear as positive Δ*I*/sec values, while areas of decreasing calcium concentration appear as negative values, but at a much smaller magnitudes.

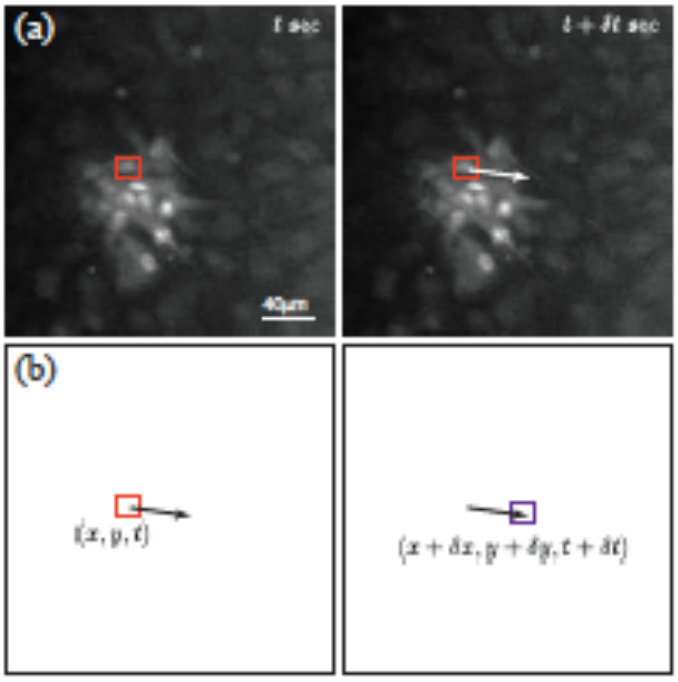

Figure 4.2 The optical flow algorithm. (a) A window in the same location in two subsequent image frames is used to compute a displacement or flow vector (arrow) for the pixel at the center of the window. Only image intensity values in are used for the calculation. Vectors are computed for each pixel in an image frame except in border regions where the vector falls outside of the image. (b) Given the position of the pixel as (x, y) at t seconds, (x, y, t), the displacement vector defines the motion of the pixel at the subsequent frame at ∂t seconds as (x + ∂x, y + ∂y, t +∂t).

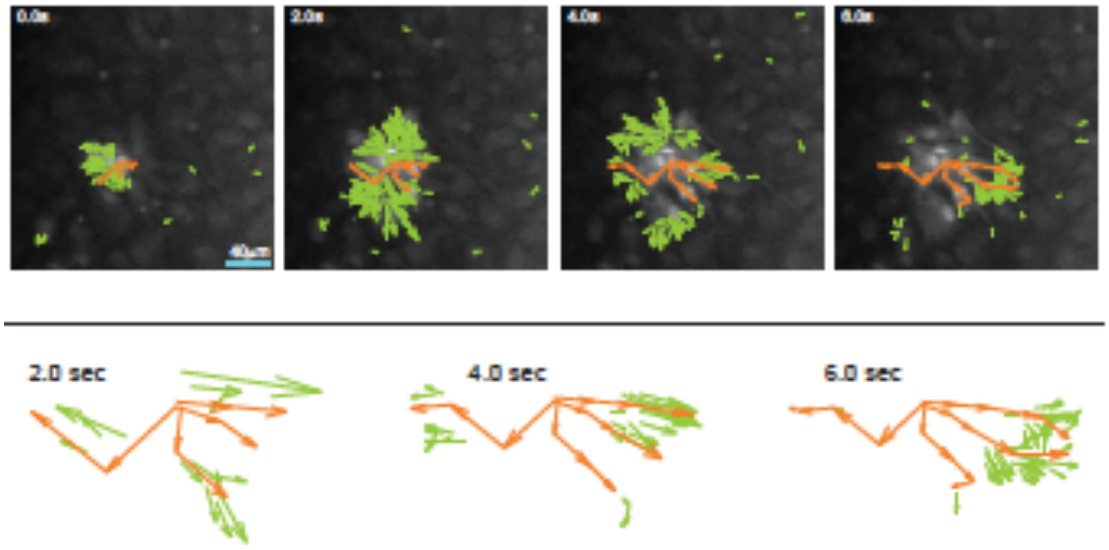

Figure 4.3 Comparison between computed optical flow vectors (green) and manually estimated flow vectors (orange). While computed vectors were calculated for every pixel and every frame, manual vectors were estimated every four frames and only trace a few selected signals. Only reliable optical flow vectors are shown, and only one in four vectors in both horizontal and vertical directions are shown for clarity. Unlike the manual vectors, flow vectors are only shown for the current frame. The top sequence of panels show vectors overlaid on extracted frames from the actual movie at the indicated times for the entire field of view. The bottom panels show the vectors in detail for the 2, 4, and 6 second frames in order to more clearly assess the qualitative overlap between optical flow computed and manually estimated results. For optical flow vectors (in green) only vectors that putatively correspond to manual vectors (in orange) are shown, in contrast to the upper panels which show all computed vectors (see text). See appendix for details regarding experimental preparations, imaging, and parameters for calculation.

Figure 4.4 (facing page) Computed optical flow vectors for induced calcium signals in spontaneously forming in vitro networks of (a) primary hippocampal neurons, (b) primary spinal cord astrocytes, and (c) the rMC-1 Muller glial-like cell line. Six frames from each representative recorded movie are shown with the computed vector field superimposed at times indicated by the time stamps in each frame (left set of six panels). Right panels: Composite temporal projections of the entire movies. The vector fields show the full spatial progression for the evolving calcium signals, with time (i.e. temporal progression) color coded by the color map (in seconds). Plotting the vector fields in this way allows the full spatiotemporal propagation of derived signals from entire movies to be summarized in a single image. This facilitates the qualitative visualization and identification of complex dynamic signaling patterns that would be difficult to detect otherwise, such as for example by simply "playing back" the movie.

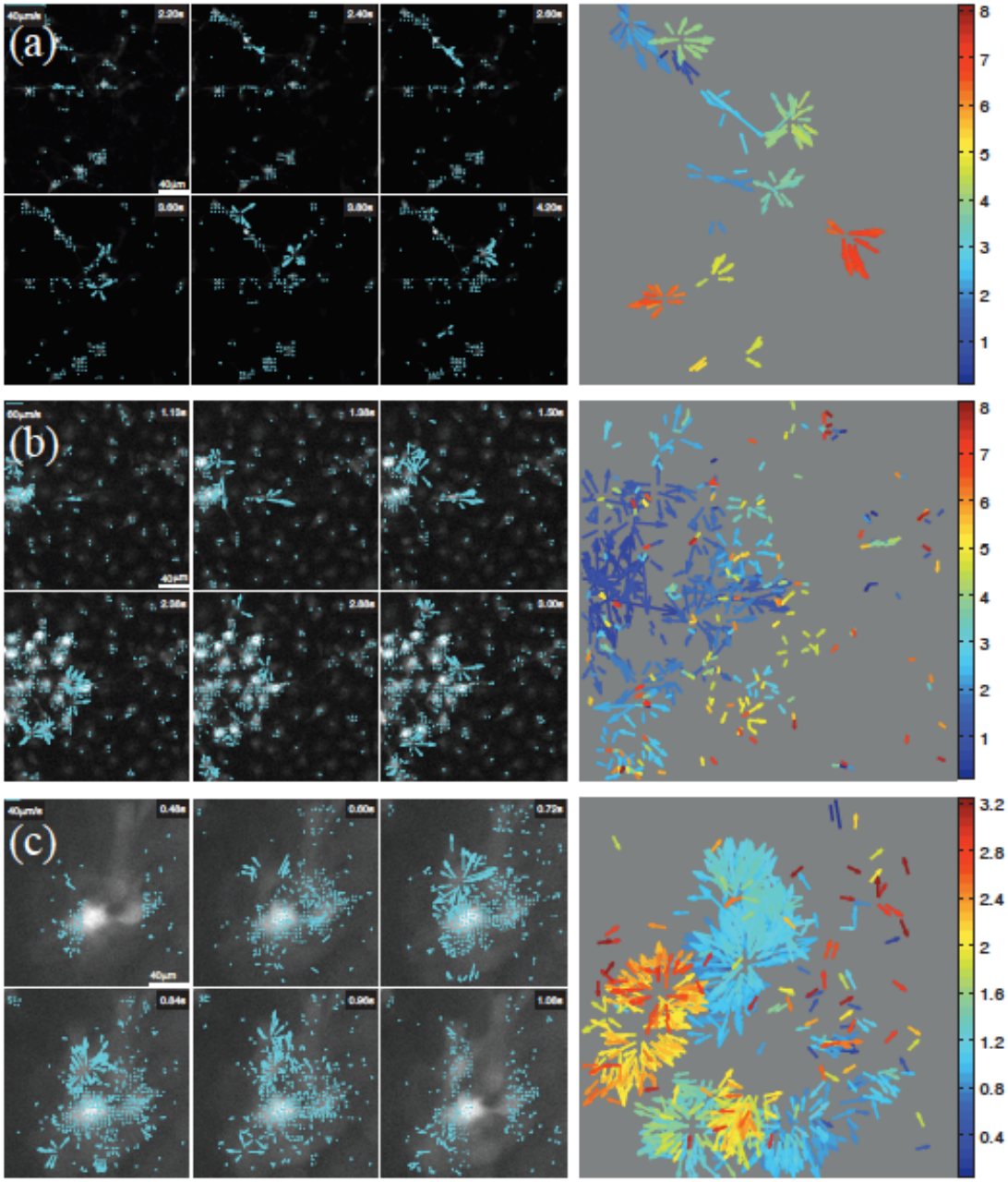
(a)
(b)
(c)
8
7
6
5
4
3
2
1
3.2
2.8
2.4
2
1.6
1.2
0.8
0.4

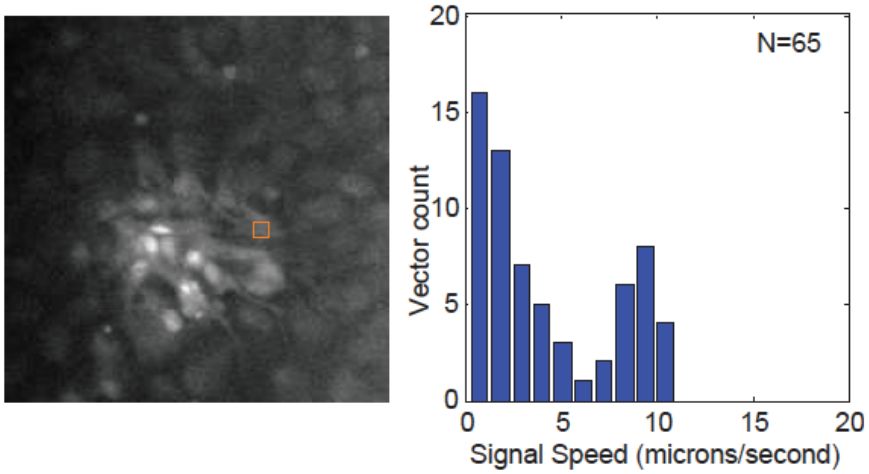

Figure 4.5 Optical flow velocity magnitude distributions for the astrocyte data from Fig. 4.4b. The flow vector magnitudes for reliable measurements in a 10 x 10 pixels (13 x 13 μm) region (orange square) shown as histograms.

DISCUSSION

We describe and show the application of optical flow gradient methods for identifying and spatiotemporally mapping functional calcium signaling in networks of neurons and glia. Although we focused on networks of cells here, the method can be equally applied to the analysis of spatially detailed sub-cellular compartmentalized regions of interest, such as dendrites or astrocyte processes. The method makes use of the spatial first derivative of moving objects in a field of view, in this case changes in fluorescence levels of calcium indicator dyes associated with the free concentration of intracellular calcium, to track their motion between subsequent frames in an image sequence (i.e. a recorded movie). The mathematical foundations of optical flow are well established and optical flow algorithms have been used in a wide variety of fields including applications to cell and molecular biology to track the movement of proteins, vesicles, and even whole cells (Miura, 2005). In neuroscience and neural engineering it has been used in electromyography (Knuttinen, 2002;

Ostlund, 2007) and sensory perception (Langley, 2007; Pagano, 1998), while clinically, it has been used to detect seizures in neonatal infants (Karayiannais, 2006) among other applications. However, the method has not been previously applied to tracking and visualizing calcium signaling and deriving quantitative measurements of calcium spatiotemporal changes that underlie intracellular and intercellular functional signaling in neural cells.

Although in this paper we applied the optical flow algorithm to two dimensional fluorescence movies, the algorithm itself can be readily applied to a recorded movie made up of three dimensional stacks acquired using two-photon microscopy. Work by others is pushing two-photon imaging towards recording real time functional signaling from three dimensional volumes of active cellular neural networks(Gobel, 2007). If the sampling rate is sufficiently high, optical flow can be computed in three dimensions using a volume instead of a square window around a pixel to generate a three dimensional displacement vector. The same constraints on volume size, sampling, and vector reliability metrics in two dimensions apply to the three dimensional case.

Optical flow methods produce a lot of data, generating a vector for every pixel in every image pair computed, so further processing, rendering and visualization methods are key to making quantitative comparisons between experimental setups. Statistical comparisons can be made from vector values by comparing differences between selected regions in different preparations; velocity averages for each region can be compared using statistical methods such as means, standard deviations, and p-values. While vector values from adjacent pixels are not statistically independent, averaged vector values for a given region of interest may be used for statistical comparison with another, non-overlapping region.

Another potential use of the vectors is to classify spatiotemporal patterns. Similar to using a scalar kernel filter to match an image pattern such as an edge or corner, vector fields themselves can be filtered with a known vector kernel to match a pattern of interest. This method is called Clifford convolution (Ebling, 2003), and has been used to label physical flow regimes in fluid dynamics applications. By designing a vector field filter and convolving it with computed optical flow vectors, a scalar map identifying specific patterns of flow associated with the spatiotemporal dynamics of the measured signal can be constructed in order to classify regions exhibiting such patterns. One of the most exciting potential uses of computed flow vectors is in functional network reconstruction. Borrowing again from the field of fluid mechanics, a dynamic vector field can be used to reconstruct the path of a hypothetical particle from a given starting point, tracing out the path that a signal might take between cells, much like a particle in a dynamic flow field (Weiskopf, 2005a, 2005b). Geometrically mapped paths of measured signals that originate in an activating cell and propagate through a network may be very useful for reconstructing the dynamics of the network. This would complement existing network reconstruction algorithms which typically rely on temporal data around fixed regions of interest.

Acknowledgments

Chapter 4 is a reprint of the material as it appears in Mapping the Spatiotemporal Dynamics of Calcium Signaling in Cellular Neural Networks Using Optical Flow, Buibas, Marius; Yu, Diana; Nizar, Krystal; Silva, Gabriel, Annals of Biomedical Engineering, 2010.

GENERAL DISCUSSION

While *in vitro* and *in situ* studies have contributed much to our understanding of astrocytes, only a small group of recent studies have looked at the function of astrocytes *in vivo*. Imaging in the intact brain is hugely important if we are to begin to understand mechanisms of bi-directional communication between astrocytes and their surround. Multi-cell bolus loading of fluorescent calcium indicators, combined with the astrocytic marker SR101, has allowed imaging of up to hundreds of astrocytes at once in the intact cortex (Gobel, 2007), cerebellum (Hoogland, 2009), and olfactory bulb (Petzold, 2008). *In vivo* studies have shown that astrocytes respond with calcium increases to whisker deflection in the barrel cortex (Wang, 2006), have orientation selectivity in the visual cortex (Schummers, 2008), and could potentially serve as long-range, network level signalers of pathological insult (Kuchibhotla, 2009; Ding, 2007). In our studies, a reliable astrocytic calcium response was not observed despite very robust neuronal and vessel dilation responses to forepaw or whisker stimulus. This calls into question the causal relationship between neuronal glutamate release and astrocytic calcium response. Importantly, we did observe astrocytic responsiveness to neuronal activity with NADH imaging, representative of a rapid oxidative metabolism response within individual astrocytes.

The slow temporal characteristics of the astrocytic calcium responses reported here are consistent with previously published studies from Nedregaard's group (Wang, 2006) and others (Gobel, 2007; Schummers, 2008). However, vasodilation was not measured simultaneously in those studies. Our results provide direct, simultaneous assessment of multiple aspects of the NVU, and fail to support a rapid role of astrocytic calcium in coupling neuronal activity to changes in the vasculature.

It remains possible that neurovascular coupling occurs through a suppression of arteriolar calcium oscillations, possibly through smooth muscle hyperpolarization. There may be a non-calcium dependent, complex, bidirectional communication between astrocytes and vascular reactivity.

There is a definite need to investigate further if astrocytes are, in fact, a much more heterogeneous population than we currently believe. To do so, experiments and findings must be evaluated based on some basic requirements: intact flow, functional NVU, and standardization of anesthesia methods. Within the *in vivo* mouse model, which most readily meets all of these requirements, astrocytes must be looked at with respect to potential heterogeneity in their response kinetics, laminar distribution, and metabolic efficiency. Understanding the normal physiological mechanisms underlying the bidirectional communication between elements of the NVU will serve as a foundation for understanding pathological disorders associated with brain microcirculation, such as stroke, Alzheimer's disease, and migraine (Iadecola, 2004), and aid in the advancement of fMRI as a diagnostic tool.

Future perspectives

In the future, it will be important to combine TPLSM imaging of NADH with simultaneous TPLSM imaging of calcium and hemodynamic activity. This tripartite imaging approach would open unprecedented opportunities to study the functional interactions within the NVU from both metabolic and vascular-centric points of view. Taking on the challenge of tripartite imaging has the potential to transform the investigation of rodent models of human brain disease, providing the opportunity to study homeostasis and functional interactions among the neurons, glia, and capillaries of the living brain. Moreover, repeated imaging at different stages of

disease could help to define a set of in vivo imaging biomarkers characterizing the progression of NVU pathology that could then be used for objective screening of potential therapies.

In terms of the question of the existence of intercellular calcium waves in astrocytes *in vivo,* the discrepancy between *in vivo* and *in vitro* results provides our first clue as to the complexity of this phenomenon. It will be important to more clearly define whether this is a physiological or a pathological phenomenon in order to determine what aspects of the NVU environment the astrocytes may be responding to. The complexity of the phenomenon makes it easy to miss important details in describing waves, as well as easy to misinterpret events as propagating signals that may not actually be as well correlated in time as they appear within our highly limited window of observation. We point out here that the repertoire of calcium events present in individual astrocytes may be elicited by acute as well as chronic causes of damage, and thus, has the potential to function as a biomarker of acute distress or chronic disease in the neuroglial environment.

Caveats and potential limitations

Although more in vivo work is certainly necessary, physiological stimulation paradigms must also be regarded with caution as different anesthetics affect blood flow and neural activity/sensitivity in different ways. Anesthesia is known to affect the magnitude of the CBF response, and slight increases in isoflurane have been reported to suppress the astrocytic calcium response markedly more than the neighboring neuronal calcium responses (Schummers, 2008). Likewise, Hoogland et al. (2009) found that spontaneous calcium waves in Bergman glia of the cerebellum occurred with a frequency that was inversely correlated with the depth of anesthesia,

as revealed by comparison of imaging in awake animals versus animals anesthetized with isoflurane. Although we utilized a variety of different anesthetics in our experiments here and found no observable effect on the responsiveness of astrocytes, it is an important criteria to keep in mind when comparing results from different studies, and studies of NVU physiology in the awake animal will be important in the future.

It has been commonly assumed that a change in astrocyte calcium measured globally reflects similar changes near the plasma membrane. However, the application of total internal reflection fluorescence (TIRF) microscopy (Jaiswal, 2007) to measure near-membrane calcium signals, revealed that half of spontaneous calcium transients measured globally fail to elevate calcium near the plasma membrane (Shigetomi, 2010). However, they do note that those that failed to elevate calcium near the plasma membrane were significantly smaller in amplitude and shorter in duration than globally spreading transients. The calcium events we measure here using bulk loaded OGB, show ΔF/F ranges in the regime of large amplitude transients that tend to spread globally to include the area near the plasma membrane.

Recent advances in calcium imaging

Recently, the development of ways to selectively target astrocytes with fluorescent calcium indicator proteins (FCIPs) has enabled investigators to achieve greater resolution and study astrocyte function *in vivo* without the confounding effects of other neuropil signals. There are four methods of getting FCIP DNA into neurons and astrocytes *in vivo*. Generation of transgenic animals, *in utero* electroporation, single-cell electroporation, and recombinant viruses. Only the viral

approach has been used successfully for imaging functional glial signals *in vivo* (Hoogland, 2009). The mosaic expression of FCIPs by astrocytes after viral gene transfer has enabled the *in vivo* study of calcium signals localized to sub-cellular compartments of Bergmann glia in the cerebellum (Hoogland, 2009). However, current FCIPs exhibit slow on and off calcium-binding rates and significantly smaller fluorescence changes relative to synthetic dyes. This limits them to the detection of slow (seconds), large amplitude (μM), calcium signals. Furthermore, the use of a fusion protein containing the calcium indicator as well as a nonfunctional fluorescent marker such as DsRed is often required to enhance the detectability of infected astrocytes. This is because of the low resting fluorescence *in vivo* of calcium sensor proteins such as G-CaMP2. Despite these limitations, the control over the sparseness (varied by the injection rate/volume) as well as type of cells infected (varied by selection of viral serotype and promoter) enables a level of spatial resolution (not limited by optical resolution) which is impressive and needs to be explored in future studies of cortical astrocytes as better FCIPs are designed.

One of the additional advantages of viral vector loading is the possibility of repeated imaging of calcium signals from 1 to 25 days after virus injection (Hoogland, 2009). The development of transgenic mice expressing FCIP in astrocytes would allow noninvasive and long-term imaging beyond what is currently feasible using virus-based approaches. However, beyond the fact that functional FCIP expression has yet to be achieved using transgenic approaches, there are many limitations, including an inability to modulate the number and range of FCIP-expressing cells, and low expression levels due to gene silencing, interaction with endogenous calmodulin, and proteolysis. Novel FCIPs are being designed to

address these issues (Palmer, 2006), and their successful application to *in vivo* imaging is eagerly anticipated.

Advances still needed in subcellular calcium imaging

Intracellular calcium concentration increases are studied as a potential form of astrocyte excitability that may control astrocyte involvement in both synaptic and cerebrovascular regulation. Given the unique cellular architecture of astrocytes, and the timescale necessary to participate in synaptic function and regulate blood flow, an involvement of rapid signaling events within the distal processes that contact synapses or blood vessels appears necessary. However, current methods cannot resolve calcium in such small volume compartments. It has been shown that somatic calcium signals may be an unreliable measure of astrocyte excitability and downstream signaling (Shigetomi, 2008). It even appears that pharmacologically evoked astrocyte calcium transients that, at the somatic level, appear similar in terms of temporal and spatial dynamics, do not represent a binary signal for interactions with neurons. Rather, astrocytes must be appropriately excited, via particular receptor pathways, to elicit neuronal response (Shigetomi, 2008). Thus, astrocytes are theorized to signal at a local level via their distal processes, but most experimental evidence feeding the controversies over astrocyte-to-neuron and astrocyte-to-blood vessel signaling involves calcium measurements in somatic compartments.

Application of a genetically targeted membrane-tethered calcium sensor (Lck-GCaMP2) to astrocyte-neuron co-cultures have resulted in the identification of highly localized and frequent spontaneous calcium signals in astrocyte somata and processes that conventional genetically encoded calcium sensors (GCaMP2) fail to detect (Shigetomi, 2010). The application of such technology to future *in vivo*

imaging work will help to resolve the issue of monitoring calcium signals in astrocytic fine processes. Given the significance of monitoring localized calcium signals in distal processes that contact synapses as well as in endfeet contacting blood vessels, it will be important to generate transgenic mice that express a spatially and temporally high resolution calcium sensor, such as Lck-GCaMP2, selectively in astrocytes. This would will help to determine whether distal astrocyte processes have similar transients to those measured from somatic regions, and whether calcium transients are compartmentalized in astrocyte branches.

One further consideration must be that a full-fledged calcium response in astrocytes may not be required for the initial signaling to vascular smooth muscle. VIP increases calcium in astrocyte endfeet (Straub, 2006) so interneuron release of VIP could bypass somatic calcium response and act directly on endfeet. Alternatively, calcium sensitive potassium channels in endfeet may need only calcium sparks from locally released endoplasmic reticulum calcium to be activated and release potassium to act on inwardly rectifying potassium channels of the smooth muscle. The existence of these possibilities points to a need for fast time resolution and an appropriate calcium dye to detect calcium sparks in endfeet. Finally, an important consideration is that the calcium indicator that is developed to fit these criteria must not affect the calcium dynamics via a strong calcium buffering effect.

Potential for calcium functions on a slower time scale

An increase in the intracellular calcium ion concentration controls a diverse range of cell functions. These include adhesion, motility, gene expression, and proliferation. Calcium signaling patterns are diverse in form as well, occurring as single transients, repetitive oscillations, or sustained plateaus. However, it is not

known whether and which of these pattern characteristics are responsible for encoding the specificity of cellular responses. It has been observed in B lymphocytes that amplitude and duration of the calcium signal differentially encode the activation of the pro-inflammatory transcription factors. Large transient rises in intracellular calcium selectively activate NF-kB and JNK, whereas low, sustained calcium plateaus activated NFAT (Dolmetsch, 1997). It is conceivable that such calcium transient characteristics could also distinguish between various astrocyte signaling effects. Therefore, in order to tease apart the functional role(s) of astrocytes within the NVU, it may be necessary to even further distinguish “types” of calcium signaling events. This is why the development and integration of more detailed image processing techniques such as optical flow is necessary if we are to accurately and adequately describe the huge variability present in the spontaneous and evoked calcium signaling events of astrocytes. The highly variable calcium oscillations which are lumped together as “spontaneous” astrocytic calcium events by the dogma of astrocyte literature may have very specific downstream consequences that simply act on a time scale much longer than we are currently given to assess.

REFERENCES

Agulhon C, Petravicz J, McMullen AB, Sweger EJ, Minton SK, Taves SR, Casper KB, Fiacco TA, McCarthy KD. (2008) What is the role of astrocyte calcium in neurophysiology? *Neuron*. 59(6):932-46.

Agulhon C, Platel JC, Kolomiets B, Forster V, Picaud S, Brocard J, Faure P, Brulet P. (2007) Bioluminescent imaging of Ca2+ activity reveals spatiotemporal dynamics in glial networks of dark-adapted mouse retina. *J Physiology*. 583(3):945-58.

Allen N and Barres B. (2005) Signaling between glia and neurons: focus on synaptic plasticity. *Curr Opin Neurobiol*. 15(5):542-8.

Anderson CM, Nedergaard M. (2003) Astrocyte-mediated control of cerebral microcirculation. *Trends Neurosci*. 26(7):340-4.

Baker S and Matthews I. (2004) Lucas-Kanade 20 years on: A unifying framework. *Int J Computer Vision*. 56(3):221-55.

Baraldi P, Sarti A, Lamberti C, Prandini A, Sgallari F. (1996) Evaluation of differential optical flow techniques on synthesized echo images. *IEEE T Bio-Med Eng*. 43(3): 259-72.

Barron JL, Fleet DJ, Beauchemin SS. (1994) Performance of optical flow techniques. *Int J Computer Vision*. 12(1):43-77.

Bennett M. (2005) A quantitative model of purinergic junctional transmission of calcium waves in astrocyte networks. *Biophys Journal*. 89(4):2235-50.

Blanco VM, Stern JE, Filosa JA. (2008) Tone-dependent vascular responses to astrocyte-derived signals. *Am J Physiol Heart Circ Physiol*. 294(6):H2855-63.

Bushong EA, Martone ME, Jones YZ, Ellisman MH. (2002) Protoplasmic astrocytes in CA1 stratum radiatum occupy separate anatomical domains. *J Neurosci.* 22(1): 183-92.

Canepari M, Djurisic M, Zecevic D. (2008) Dendritic signals from rat hippocampal CA1 pyramidal neurons during coincident pre- and post-synaptic activity: a combined voltage- and calcium imaging study. *J Physiology*. 580(2):463-84.

Cauli B, Hamel E. (2010) Revisiting the role of neurons in neurovascular coupling. *Front Neuroenergetics*. 2:1-8.

Cauli B, Tong XK, Rancillac A, Serluca N, Lambolez B, Rossier J, Hamel E. (2004) Cortical GABA interneurons in neurovascular coupling: relays for subcortical vasoactive pathways. *J Neurosci*. 24(41):8940-9.

Cornell-Bell A, Finkbeiner S, Cooper M. (1990) Glutamate induces calcium waves in cultured astrocytes: long-range glial signaling. *Science*..

Denk W, Strickler JH, Webb WW. (1990) Two-photon laser scanning fluorescence microscopy. *Science*. 248, 73-6.

Denk W, Delaney KR, Kleinfeld D, Strowbridge B, Tank DW, Yuste R. (1994) Anatomical and functional imaging of neurons and circuits using two photon laser scanning microscopy. *J Neurosci Methods*. 54:151-62.

Ding S, Fellin T, Zhu Y, Lee SY, Auberson YP, Meaney DF et al (2007) Enhanced astrocytic Ca2+ signals contribute to neuronal excitotoxicity after status epilepticus. *J Neurosci*. 27(40):10674-84.

Dolmetsch RE, Xu K, Lewis RS. (1998) Calcium oscillations increase the efficiency and specificity of gene expression. *Nature*. 392:933-6.

Ebling J and Scheuermann G. (2003) Clifford convolution and pattern matching on vector fields. *Visualization 2003 IEEE*, 193-200.

Fiacco TA, McCarthy KD. (2006) Astrocyte calcium elevations: properties, propagation, and effects on brain signaling. *Glia*. 54(7):676-90.

Filosa JA, Bonev AD, Nelson MT. (2004) Calcium dynamics in cortical astrocytes and arterioles during neurovascular coupling. *Circ Res*. 95(10):e73-81.

Foster KA, Beaver CJ, Durner DA. (2005) Interaction between tissue oxygen tension and NADH imaging during synaptic stimulation and hypoxia in rat hippocampal slices. *Neuroscience.* 132:645-57.

Galeffi F, Foster KA, Sadgrove MP, Beaver CJ, Turner DA. (2007) Lactate uptake contributes to the NAD(P)H biphasic response and tissue oxygen response during synaptic stimulation in area CA1 of rat hippocampal slices. *J Neurochem*. 103(6): 2449-61.

Garaschuk O, Milos RI, Konnerth A. (2006) Targeted bulk-loading of fluorescent indicators for two-photon brain imaging in vivo. *Nat Protoc*. 1(1):380-6.

Gobel W and Helmchen F. (2007) In vivo calcium imaging of neural network function. *Physiology*. 22(6):358-65.

Gordon GR, Choi HB, Rungta RL, Ellis-Davies GC, MacVicar BA. (2008) Brain metabolism dictates the polarity of astrocyte control over arterioles. *Nature*. 456 (7223):745-9.

Gordon GR, Mulligan SJ, MacVicar BA. (2007) Astrocyte control of the cerebrovasculature. *Glia*. 55(12):1214-21.

Guo Y, Gong B, Levesque S, Manfredi T, Sun Y. (2004) Automated detection and delineation of mitochondria in electron micrographs of human skeletal muscles. *Microsc Res Tech*. 63(3):133-9.

Hashemi M, Buibas M, Silva GA. (2008) Automated detection of intercellular signaling in astrocyte networks using the converging squares algorithm. *J Neurosci Meth*. 170(2):294-9.

Helmchen F, Kleinfeld D. (2008) In vivo measurements of blood flow and glial cell function with two-photon laser-scanning microscopy. *Meth Enzymol*. 444:231-54.

Hirase H, Qian L, Bartho P, Buzsaki G. (2004) Calcium dynamics of cortical astrocytic networks in vivo. *PLoS Biol*. 2(4):E96.

Hoogland TM, Kuhn B, Gobel W, Huang W, Nakai J, Helmchen F, Flint J, Wang SS. (2009) Radially expanding transglial calcium waves in the intact cerebellum. *PNAS.* 106(9):3496-501.

Horn B and Schunck B. (1981) Determining optical flow (distribution of apparent movement velocities of image brightness . . . . Techniques and applications of image understanding, 21-23:319-31.

Iadecola C. (2004) Neurovascular regulation in the normal brain and in Alzheimer's disease. *Nat Rev Neurosci*. 5(5):347-60.

Iadecola C, Nedergaard M. (2007) Glial regulation of the cerebral microvasculature. *Nat Neurosci*. 10(11):1369-76.

Jahne B. (2005) Digital Image Processing. Springer, 6th ed., 2005.

Kang M and Othmer HG. (2009) Spatiotemporal characteristics of calcium dynamics in astrocytes. *Chaos*. 19(3):037116.

Kann O, Schuchmann S, Buchheim K, Heinemann U. (2003) Coupling of neuronal activity and mitochondrial metabolism as revealed by NAD(P)H fluorescence signals in organotypic hippocampal slice cultures of the rat. *Neuroscience*. 119:87-100.

Karayiannis NB, Tao G, Frost JD, Wise MS, Hrachovy RA, Mizrahi EM. (2006) Automated detection of videotaped neonatal seizures based on motion segmentation methods. *Clin Neurophysiol*, 117(7):1585-94.

Knuttinen MG, Parrish TB, Weiss C, LaBar KS, Gitelman DR, Power JM, Mesulam MM, Disterhoft JF. (2002) Electromyography as a recording system for eyeblink conditioning with functional magnetic resonance imaging. *Neuroimage*, 17(2):977-87.

Kocharyan A, Fernandes P, Tong X-K, Vaucher E, Hamel E. (2007) Specific subtypes of cortical GABA interneurons contribute to the neurovascular coupling response to basal forebrain stimulation. *J Cereb Blood Flow Metab*. 28:221-31.

Koehler RC, Gebremedhin D, Harder DR. (2006) Role of astrocytes in cerebrovascular regulation. *J Appl Physiol.* 100(1):307-17.

Koehler RC, Roman RJ, Harder DR. (2009) Astrocytes and the regulation of cerebral blood flow. *Trends Neurosci*. 32(3):160-9.

Kuchibhotia KV, Lattarulo CR, Hyman BT, Bacskai BJ. (2009) Synchronous hyperactivity and intercellular calcium waves in astrocytes in Alzheimer mice. *Science.* 323(5918):1211-5.

Kurth-Nelson ZL, Mishra A, Newman EA. (2009) Spontaneous glial calcium waves in the retina develop over early adulthood. *J Neurosci*. 29(36):11339-46.

Langley K and Anderson SJ. (2007) Subtractive and divisive adaptation in visual motion computations. *Vision Res*. 47(5):673-86.

Lim S, Apostolopoulos J, Gamal A. (2005) Optical flow estimation using temporally oversampled video. *Image Processing, IEEE Transactions*, 14(8):1074-87.

Lin A, Fox PT, Hardles J, Duong TQ, Gao JH. (2010) Nonlinear coupling between cerebral blood flow, oxygen consumption, and ATP production in human visual cortex. *PNAS*. 107(18): 8446-51.

Lindauer U, Leithner C, Kaasch H, Rohrer B, Foddis M, Fuchtemeier M, Offenhauser N, Steinbrink J, Royl G, Kohl-Bareis M, Dirnagl U. (2010) Neurovascular coupling in rat brain operates independent of hemoglobin deoxygenation. *J Cereb Blood Flow Metab*. 30(4):757-68.

Liu X, Li C, Falck JR, Roman RJ, Harder DR, Koehler RC. (2008) Interaction of nitric oxide, 20-HETE, and EETs during functional hyperemia in whisker barrel cortex. *Am J Physiol Heart Circ Physiol*. 295(2):H619-31.

MacDonald CL, Yu D, Buibas M, Silva GA. (2008) Diffusion modeling of ATP signaling suggests a partially regenerative mechanism underlies astrocyte intercellular calcium waves. *Front Neuroeng*. 1.

Metea MR, Kofuji P, Newman EA. (2007) Neurovascular coupling is not mediated by potassium siphoning from glial cells. *J Neurosci*. 27(10):2468-71.

Metea MR, Newman EA. (2006) Glial cells dilate and constrict blood vessels: a mechanism of neurovascular coupling. *J Neurosci*. 26(11):2862-70.

Mintun MA, Lundstrom BN, Snyder AZ, Vlassenko AG, Shulman GL, Raichle ME. (2001) Blood flow and oxygen delivery to human brain during functional activity: theoretical modeling and experimental data. *PNAS*. 98:6859-64.

Mironov SL, Richter DW. (2001) Oscillations and hypoxic changes of mitochondrial variables in neurons of the brainstem respiratory centre of mice. *J Physiol (Lond)*. 533:227-36.

Miura K. (2005) Tracking movement in cell biology. *Adv Biochem Eng Biotechnol*. 95:267-95.

Mukamel EA, Nimmerjahn A, Schnitzer MJ. (2009) Automated analysis of cellular signals from large-scale calcium imaging data. *Neuron*. 63(6):747-60.

Mulligan SJ, MacVicar BA. (2004) Calcium transients in astrocyte endfeet cause cerebrovascular constrictions. *Nature.* 431(7005):195-9.

Newman EA and Zahs KR. (1997) Calcium waves in retinal glial cells. *Science*. 275 (5301):844-7.

Nimmerjahn A, Kirchhoff F, Kerr JN, Helmchen F. (2004) Sulforhodamine 101 as a specific marker of astroglia in the neocortex *in vivo*. *Nat Methods*. 29, 31-7.

Ostlund N, Gerdle B, Karlsson JS. (2007) Location of innervation zone determined with multichannel surface electromyography using an optical ow technique. *J Electromyography Kinesiology*. 17(5):549-55.

Pagano C and Bingham G. (1998) Comparing measures of monocular distance perception: Verbal and reaching errors are not correlated. *J Exp Psych-Human Perception*, Jan 1998.

Palmer AE, Giacomello M, Kortemme T, Hires SA, Lev-Ram V, Baker D, Tsien RY. (2006) Ca2+ indicators based on computationally redesigned calmodulin-peptide pairs. *Chem Biol* 13(5):521-30.

Paredes RM, Etzler JC, Watts LT, Zheng W, Lechleiter JD. (2008) Chemical calcium indicators. *Methods*, 46(3):143-51.

Paspalas CD, Papadopoulos GC. (1998) Ultrastructural evidence for combined action of noradrenaline and vasoactive intestinal polypeptide upon neurons, astrocyte, and blood vessels of the rat cerebral cortex. *Brain Res Bull*. 45:247-59.

Petzold GC, Albeanu DF, Sato TF, Murthy VN. (2008) Coupling of neural activity to blood flow in olfactory glomeruli is mediated by astrocytic pathways. *Neuron*. 58(6): 897-910.

Powers WJ, Hirsch IB, Cryer PE. (1996) Effect of stepped hypoglycemia on the regional cerebral blood flow response to physiologic brain activation. *Am J Physiol Heart Circ Physiol*. 270:H554-9.

Rancillac A, Rossier J, Guille M, Tong X-K, Geoffroy H, Amatore C, Arbault S, Hamel E, Cauli B. (2006) Glutamatergic control of microvascular tone by distinct GABA neurons in the cerebellum. *J Neurosci*. 26(26):6997-7006.

Rouach N, Koulakoff A, Abudara V, Willecke K, Giaume C. (2008) Astroglial metabolic networks sustain hippocampal synaptic transmission. Science. 322:1551-5.

Roy CS, Sherrington CS. (1890) On the regulation of the blood supply of the brain. *J Physiol (Lond)*. 11(1-2):85-158.17.

Scemes E and Giaume C. (2006) Astrocyte calcium waves: what they are and what they do. *Glia*. 54(7):716-25.

Schipke CG, Haas B, Kettenmann H. (2008) Astrocytes discriminate and selectively respond to the activity of a subpopulation of neurons within the barrel cortex. *Cereb Cortex*. 18(10):2450-9.

Schummers J, Yu H, Sur M. (2008) Tuned responses of astrocytes and their influence on hemodynamic signals in the visual cortex. *Science*. 320(5883):1638-43.

Shigetomi E, Kracun S, Sofroniew MV, Khakh BS. (2010) A genetically targeted optical sensor to monitor calcium signals in astrocyte processes. *Nat Neurosci*. 13 (6): 759-66.

Silva GA, Feeney C, Mills LR, Theriault E. (1998) A novel and rapid method for culturing pure rat spinal cord astrocytes on untreated glass. *J Neurosci Methods*. 80 (1):75-9.

Simard M, Arcuino G, Takano T, Liu QS, Nedergaard M. (2003) Signaling at the gliovascular interface. *J Neurosci*. 23(27):9254-62.

Smetters D, Majewska A, Yuste R. (1999) Detecting action potentials in neuronal populations with calcium imaging. *Methods*, Jan 1999.

Straub SV, Bonev AD, Wilkerson MK, Nelson MT. (2006) Dynamic inositol triphosphate-mediated Calcium signals within astrocytic endfeet underlie vasodilation of cerebral arterioles. *J Gen Physiol*. 128(6):659-69.

Takano T, Han X, Deane R, Zlokovic B, Nedergaard M. (2007) Two-photon imaging of astrocytic Ca2+ signaling and the microvasculature in experimental mice models of Alzheimer's disease. *Ann N Y Acad Sci*. 1097:40-50.

Takano T, Tian GF, Peng W, Lou N, Libionka W, Han X, Nedergaard M. (2006) Astrocyte-mediated control of cerebral blood flow. *Nat Neurosci.* 9(2):260-7.

Tian GF, Takano T, Lin JH, Wang X, Bekar L, Nedergaard M. (2006) Imaging of cortical astrocytes using 2-photon laser scanning microscopy in the intact mouse brain. *Adv Drug Deliv Rev*. 58(7):773-87.

Tian L and Looger L. (2008) Genetically encoded fluorescent sensors for studying healthy and diseased nervous systems. *Drug discovery today: Disease models*. 5(1): 27-35.

Tian P, Teng IC, May LD, Kurz R, Lu K, Scadeng M, Hillman EMC, De Crespigny AJ, D'Arceuil HE, Mandeville JB, Marota JJA, Rosen BR, Liu TT, Boas DA, Buxton RB, Dale AM, Devor A. (2010) Cortical depth-specific microvascular dilation underlies laminar differences in blood oxygenation level-dependent functional MRI signal. *PNAS*. Early Edition

Ventura R, Harris KM. (1999) Three-dimensional relationship between hippocampal synapses and astrocytes. *J Neurosci*. 19:6897-906.

Vogelstein J, Watson B, Packer A. (2009) Spike inference from calcium imaging using sequential Monte Carlo methods. *Biophys J*, Jan 2009.

Wang X, Lou N, Xu Q, Tian GF, Peng WG, Han X, Kang J, Takano T, Nedergaard M. (2006) Astrocytic Ca2+ signaling evoked by sensory stimulation in vivo. *Nat Neurosci*. 9(6):816-23.

Wang X, Takano T, Nedergaard M. (2009) Astrocytic calcium signaling: mechanism and implications for functional brain imaging. *Methods Mol Biol.* 489:93-109.

Weiskopf D and Erlebacher G. (2005) 12: Overview of flow visualization. The visualization handbook, Jan 2005.

Weiskopf D, Schramm F, Erlebacher G, Ertl T. (2005) Particle and texture based spatiotemporal visualization of time-dependent vector fields. *Vis 05 IEEE*, 639-46.

Winship IR, Plaa N, Murphy TH. (2007) Rapid astrocyte calcium signals correlate with neuronal activity and onset of the hemodynamic response in vivo. *J Neurosci*. 27(23):6268-72.

Wolf T, Lindauer U, Villringer A, Dirnagl U. (1997) Excessive oxygen or glucose supply does not alter the blood flow response to somatosensory stimulation or spreading depression in rats. *Brain Res*. 761:290-9.

Xu HL, Mao L, Ye S, Palsansathan C, Vetri F, Pelligrino DA. (2008) Astrocytes are a key conduit for upstream signaling of vasodilation during cerebral cortical neuronal activation in vivo. *Am J Physiol Heart Circ Physiol*. 294(2):H622-32.

Yaksi E and Friedrich RW. (2006) Reconstruction of firing rate changes across neuronal populations by temporally deconvolved Ca2+ imaging. *Nat Meth*. 3(5): 377-83.

Yu D, Buibas M, Chow SK, Lee IY, Singer Z, Silva GA. (2009) Characterization of calcium mediated intracellular and intercellular signaling in the rMC-1 glial cell line. *Cell Mol Bioeng*. 2(1):144-55.

Zhang S, Murphy TH. (2007) Imaging the impact of cortical microcirculation on synaptic structure and sensory-evoked hemodynamic responses in vivo. *PLoS Biol*. 5(5):e119.

Zonta M, Angulo MC, Gobbo S, Rosengarten B, Hossmann KA, Pozzan T, Carmignoto G. (2003) Neuron-to-astrocyte signaling is central to the dynamic control of brain microcirculation. *Nat Neurosci*. 6(1):43-50.